# Research and Development of Particle Detectors for Muon Tomography and the CERN ALICE Experiment

Ph.D. Thesis

**LÁSZLÓ OLÁH**

Eötvös Loránd University
Doctorate School of Physics
Head: Dr. Tamás Tél
Particle Physics and Astronomy Program
Head: Dr. László Palla

Supervisors:
Dr. Dezső Varga
Dr. Gergely Gábor Barnaföldi

MTA Wigner Research Centre for Physics,
Research Institute for Particle and Nuclear Physics

Budapest, 2016

# Contents

# 1 Introduction

## 1.1 Particle physics: the fundamental laws of Nature

The motivation of particle physics is to describe the material world with the elementary building blocks and the interactions between them. The Standard Model (SM) provides a consistent picture about our present knowledge of the particles, summarised in Fig. 1 [1, 2]. The material world is built up of fermions. There are two kinds of fermions: leptons and quarks, each type has three families. Leptons have zero or $\pm$ 1 charge and quarks have fractional charge with the values of +2/3 or -1/3. Each fermion has antiparticle with the same physical properties, except that the charge is opposite. The SM includes the electromagnetic, the strong, and the weak interactions. While quarks participate in both the electroweak and the strong interactions, leptons participate only in the electroweak one. These interactions are mediated by spin-1 gauge bosons: the photon for the electromagnetic, eight gluons for the strong, and $Z^0$ and $W^{\pm}$ bosons for the weak interaction. The SM is a gauge theory with the SU(3) $\times$ SU(2) $\times$ U(1) gauge group. Furthermore, the SM includes the newly discovered Higgs boson. This discovery verifies the Higgs theory, which describes the mass generation for the fermions via spontaneous symmetry breaking of the Higgs field. The SM is a successful model, because it could predict the existence and physical parameters of the Higgs boson, the $Z^0$ and $W^{\pm}$ bosons, gluons, and the top and bottom quarks. Furthermore, the SM describes most of the physical processes, such as decays or scatterings, and the predictions are in good agreement with experimental data.

Despite the encouraging results, the SM is not the "Theory of Everything". There are 19 parameters (masses, coupling constants, mixing angles and a CP-violation phase), which do not provide a simple description, as we expect from a "standard" model. The SM does not include the gravitation interaction, and does not describe massive neutrinos. However, the neutrino oscillation experiments, such as Super-Kamiokande demonstrated that electron neutrinos transform to muon neutrinos, therefore the neutrinos have mass [3]. Moreover, the SM does not explain the quantised electromagnetic charges, the number of families, and the many orders of magnitude differences between the masses of leptons. The

unification of the SM with the theory of gravity is difficult due to the so-called hierarchy problem, which is the large energy gap between electroweak ($\sim$ 100 GeV) and Planck ($\sim 10^{19}$ GeV) energy scales. To find the way out, the SM was extended to larger gauge groups, e. g. to SU(5), or alternative models, such as the Supersymmetry (SUSY) or the String Theory were developed. Particle physics still has several open questions at present days. Some of the most intensively investigated questions are as follows.

- How was the Universe created? What happened at the first seconds of the Universe?
- Antimatter galaxies have not yet been observed. Where is the missing antimatter?
- What are the sources of cosmic rays? What is the origin of their energies?
- What is the origin and the nature of the invisible dark matter, dark energy?
- What are the limits in the parameter space of competitive theories, such as Supersymmetry or String Theory?

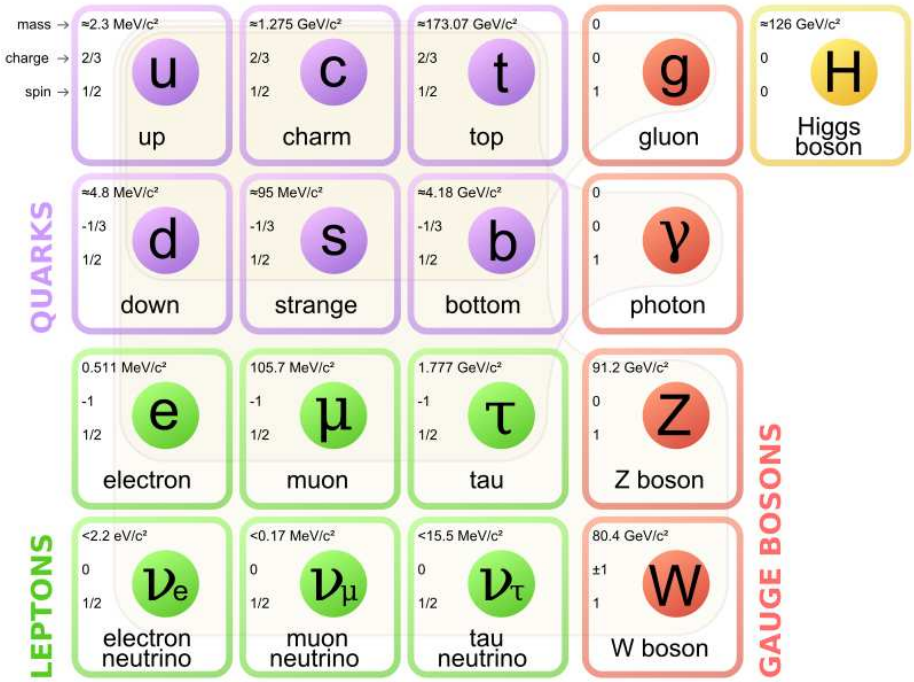


Figure 1: The particles of the Standard Model. The three families of fermions build up the material world. The gauge bosons mediate the interactions between the fermions. The existence of the Higgs boson verifies that the mass generation of fermions occurs via the spontaneous symmetry breaking of the Higgs field [1, 2].

There are several ongoing high-energy physics experiments, located underground or underwater, on the surface, and in the atmosphere of the Earth, as well as in the space, that strive to answer the above mentioned questions. The "input" of these particle physics experiments are provided by particle colliders, and historically by cosmic rays. High accuracy detectors are the key elements of these experiments. These are responsible for the identification, and the measurement of the physical properties of the sources or the secondary particles created in the investigated physical processes.

This thesis focuses on the research and development (R&D) of particle detectors for collider experiments, as well as for cosmic muon tracking and its application for imaging. The following sections introduce the various types of experiments, particle detector systems, and their applications in high-energy physics.

## 1.2 Complex detector systems in particle collision experiments

Particle colliders provide a collimated beam of initial particles with fixed energy in controlled conditions. There are two main types of particle collision experiments: the fixed-target and the beam-beam collider experiments. In the former case, the beam is accelerated and bombs the fix target material. In the latter case, two accelerators, mostly synchrotrons are placed in the same ring. These accelerate the bunches of the particles and/or the nuclei in the opposite directions, and the bunches cross each other at the interaction points.

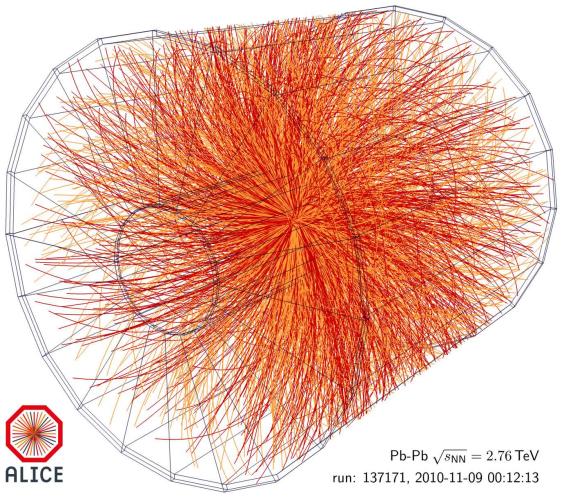


Figure 2: A Pb-Pb collision with the energy of $\sqrt{s_{NN}}$ of 2.76 TeV was produced by the Large Hadron Collider (LHC) and measured by A Large Ion Collider Experiment (ALICE) [4].

As an example, Fig. 2 shows a Pb-Pb collision event at $\sqrt{s_{NN}} = 2.76$ TeV centre-of-mass energy per nucleon pair, produced by the Large Hadron Collider (LHC) in the European Laboratory for Particle Physics (European Council for Nuclear Research, CERN), and measured by **A Large Ion Collider Experiment (ALICE)** [4, 5]. The *orange* and the *red lines* show the trajectories of the tens of thousands of secondary particles.

In both types of particle collision experiments, complex detector systems cover the interaction points (vertices), where the secondary particles are formed, and carry information about the physical processes that play a role in the collisions. A complex detector system measures the basic kinematical properties of the secondary particles, such as mass, energy, momentum, charge, as well as the global properties of the collisions, such as missing energy, vertex position, etc. These detector systems are designed and optimised specifically for the investigated physical processes. In the following, the ALICE detector system is presented as an example for a complex detector system in a beam-beam collider experiment.

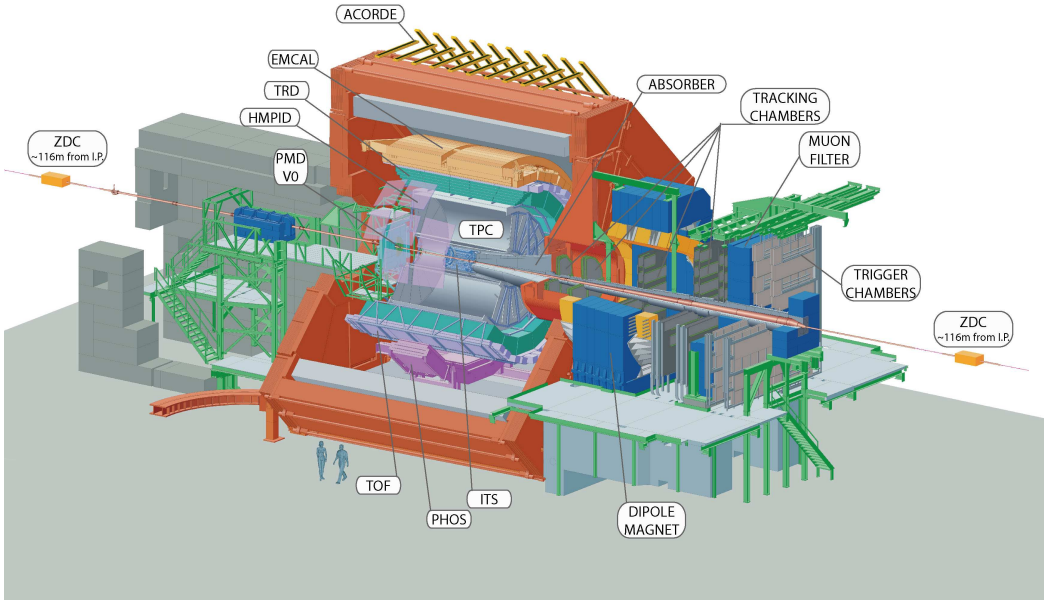


Figure 3: The structure of A Large Ion Collider Experiment (ALICE) [5].

Figure 3 shows the structure of the ALICE detector [5]. It is a huge detector system weighing 10,000 tons, and occupying $26 \times 16 \times 16$ m$^3$, placed underground at the depth of 56 m. The ALICE Collaboration aims to investigate the physics of the primordial matter of the early Universe, and its physical processes, such as the hadronisation, or the showers

of hadrons (jets) and their interaction with the hot quark-gluon plasma (QGP) created in heavy-ion collisions. If one assumes that the state variables (temperature, pressure, chemical potential, etc) of the QGP have similar values as those in the early Universe, one can study the first microseconds after the Big Bang via the measurement of heavy-ion collisions. The ALICE measures p-p, p-Pb, and Pb-Pb collisions produced by the LHC, to investigate the quark-gluon plasma.

The high-energy collisions are happening around the centre of the detectors. A group of subdetectors are placed along the beam line and determine the collision parameters. The Zero Degree Calorimeter (ZDC) measures the energy of neutrons of the colliding nuclei that did not participate in the heavy ion reaction, and detach from the colliding nuclei: this quantity is in an indirect connection with the impact parameter of the heavy-ion collision. The scintillator-based V0 detector measures the number and the spatial distribution of the secondary particles produced in the collision.

The second group of subdetectors reconstructs the vertex (collision point), and measures precisely the trajectories of particles. The Inner Tracking System (ITS) is based on semiconductor detectors. It reconstructs the position of the vertex, and the decay points of the fast-decaying particles. The Time Projection Chamber (TPC) is based on Multi-Wire Proportional Chambers (MWPC). It measures charged particle trajectories in 3D, as well as the sign of their charge, and their momentum by curvature in the magnetic field of 0.5 T. Furthermore, the TPC allows particle identification (PID) on a statistical basis by the measurement of the ionisation energy loss and momentum of the particles.

Track-by-track PID is provided by the measurement of Time-Of-Flight (TOF), and also by the detection of Cherenkov radiation with the High Momentum Particle Identification Detector (HMPID). Electron identification is performed by the measurement of transition radiation with the Transition Radiation Detector (TRD). The PHOton Spectrometer (PHOS) is applied for the discrimination of photons and other neutral decay products. The Pre-Shower Multiplicity Detector (PMD) measures the multiplicity and the spatial distribution of photons in the forward region.

For jet analysis and electron/photon identification, the ElectroMagnetic CALorimeter (EMCAL) is applied. The Muon Spectrometer measures and investigates the heavy quark decays, such as the $J/\Psi$ decay in the $\mu^+\mu^-$ channel. The ALICE COsmic Ray DEtector (ACORDE) is placed above the magnet. It measures cosmic rays up to the energy of $10^{17}$ eV with plastic scintillators, and acts as a cosmic ray trigger detector.

The Data AcQuisition system (DAQ) is optimised for two types of events: the very frequent but small multiplicity p-p events, and the relatively rare but large multiplicity Pb-Pb events. The trigger system is organised to different levels to optimise the timing, and the data sorting.

We have thus seen that detector systems at collider experiments are relatively complex instruments. These combine the different state-of-art particle detectors to select the interesting events, and reconstruct the thousands of particle trajectories with high accuracy. The arrangement of these detector systems depends on the physical motivation of the proposed measurements.

## 1.3 Cosmic ray detectors

The primary cosmic rays mostly consist of protons and lighter nuclei (He, ..., Fe) originating from astrophysical sources, as well as from the interaction of these particles and nuclei with the interstellar matter. As presented in Fig. 4, the energy range of the cosmic rays can reach $10^{21}$ eV, which is eight orders of magnitude higher than the beam energy of the LHC [6]. We can explore the Cosmos by both satellite and ground-based experiments within this extreme energy range.

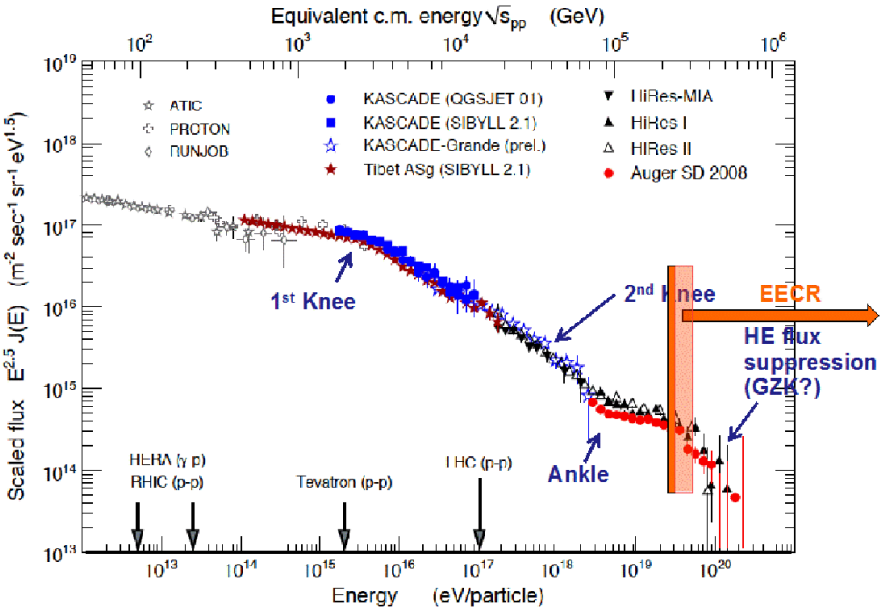


Figure 4: The energy spectrum of primary cosmic rays on the surface of the Earth [6].

The most advanced satellite-based cosmic ray detector system is the **Alpha Magnetic Spectrometer (AMS-02)**. Since 2011, it operates as an external module of the International Space Station (ISS) which orbits around the Earth at the altitude of 300 km [7]. The AMS-02 searches for baryonic antimatter by the measurement of anti-helium per helium ratio with the precision of $10^{-9}$. It is also designed to search for dark matter candidates, such as neutralino by the measurement of the energy spectra of positrons, anti-protons, and gamma rays. It also searches for a special form of matter, the so-called strangelets, which consist of a number of up, down and strange quarks, and expected to arrive with extremely high energies. Furthermore, the large amount of data helps to measure the flux and composition of cosmic rays, as well as their time variation more precisely.

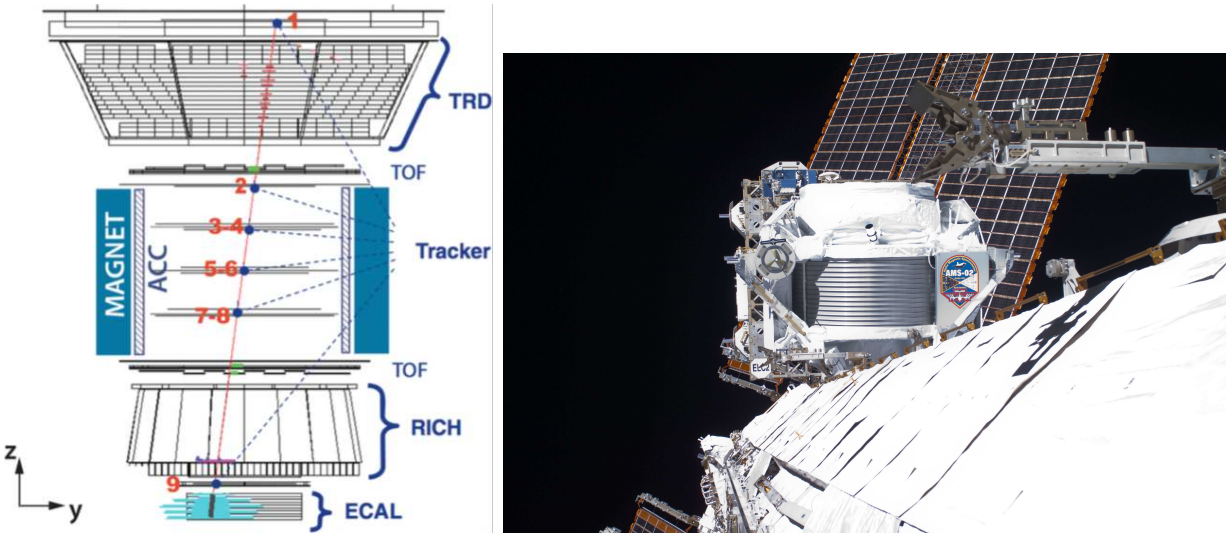


Figure 5: *Left:* The structure of the Alpha Magnetic Spectrometer (AMS-02) with a 1.03 TeV electron [7]. *Right:* A photo of AMS-02 on the International Space Station [8].

Figure 5 shows the structure (*left*) and a photo (*right*) of the AMS-02 on the ISS. It combines the state-of-art particle physics detectors. Nine silicon tracker planes with the sensitive area of 6.2 $m^2$, position resolution of 10 $\mu$m measure particle trajectories, and reconstruct their charge and momentum in the magnetic field of 0.15 T. For electron identification, the Transition Radiation Detector (TRD) is placed in vacuum above the magnet. The TOF detector discriminates upward-going and downward-going particles. A Ring Imaging CHerenkov (RICH) detector measures the charge and velocity of the particles. The Electromagnetic Calorimeter measures the 3-dimensional profile of the electromagnetic showers, identifies electrons, and measures their energy. Besides particle

detectors, the Anti-Coincidence Counter measures the event topology, reduces the background events, and keeps only those ones which take place in the detector system from top to bottom. The tracking alignment system corrects the position of tracking detectors using laser beams. Furthermore, the Star Tracker measures the orientation relatively to fixed stars.

The primary cosmic rays enter the Earth's atmosphere isotropically, collide with the atmospheric nuclei ($N_2$, $O_2$, Ar) and generate secondary particles, mostly pions ($\pi^{0,\pm}$) and kaons ($K^0$, $\overline{K}^0$, $K^\pm$). The competition of the energy dependent processes, the decays and the interactions produces three different components in the atmosphere, as shown in *panel A* of Fig. 6 [9]:

(i) The **hadronic component** consists mostly of neutrons, protons, pions and kaons. It forms the core of the particle showers.

(ii) The **soft (electromagnetic) component** is initiated by the decay of neutral pions into photons, $\pi^0 \to \gamma + \gamma$, and consists of electrons, positrons that are generated via pair production. The electrons create further photons via bremsstrahlung. Furthermore, the decays of muons, $\mu^+ \to e^+ + \nu_e + \bar{\nu}_\mu$ and $\mu^- \to e^- + \bar{\nu}_e + \nu_\mu$ produce electrons as well as the knock-on electrons, which have non-negligible contribution at small energies.

(iii) The **muonic component** is produced by weak interaction: the charged mesons decay into charged muons and neutrinos via the following channels: $\pi^+ \to \mu^+ + \nu_\mu$, $\pi^- \to \mu^- + \bar{\nu}_\mu$ and $K^+ \to \mu^+ + \nu_\mu$, $K^- \to \mu^- + \bar{\nu}_\mu$.

The highest energy primary cosmic rays create extensive air showers in the atmosphere that consist of the mentioned components. Ultra-high-energy cosmic rays (UHECR, $E > 10^{18}$ eV) generate billions of particles in the three components, which spread over a few tens of square kilometers. The primary cosmic rays are also detected on the surface of the Earth via the showers. The flux of primary cosmic rays is rapidly decreasing with increasing energy down to about few particles per km$^2$ per century at the highest energies. The detection of the extensive air showers on the surface of the Earth provides more information about the properties of the primary cosmic rays than balloon or satellite experiments. The motivation for the investigation of extensive air showers is to find the source of high energy cosmic rays, and to understand the acceleration mechanism which created them.

Extreme-energy cosmic rays (EECR, $E > 5 \times 10^{19}$ eV) were detected with the energy greater than the theoretically predicted end of the energy spectrum, the so-called Greisen – Zatsepin – Kuzmin (GZK) limit [10, 11]. The GZK cutoff suppresses the particles by interaction with the 2.7 K cosmic background radiation. The particle showers produced by EECR are also investigated.

*Panel B* of Fig. 6 shows the scheme of the **Pierre Auger Observatory**, built for the measurement of UHECRs [12]. It tracks the development and measures the energy of the air showers caused by the primary cosmic rays in the $10^{17}$-$10^{21}$ eV energy range.

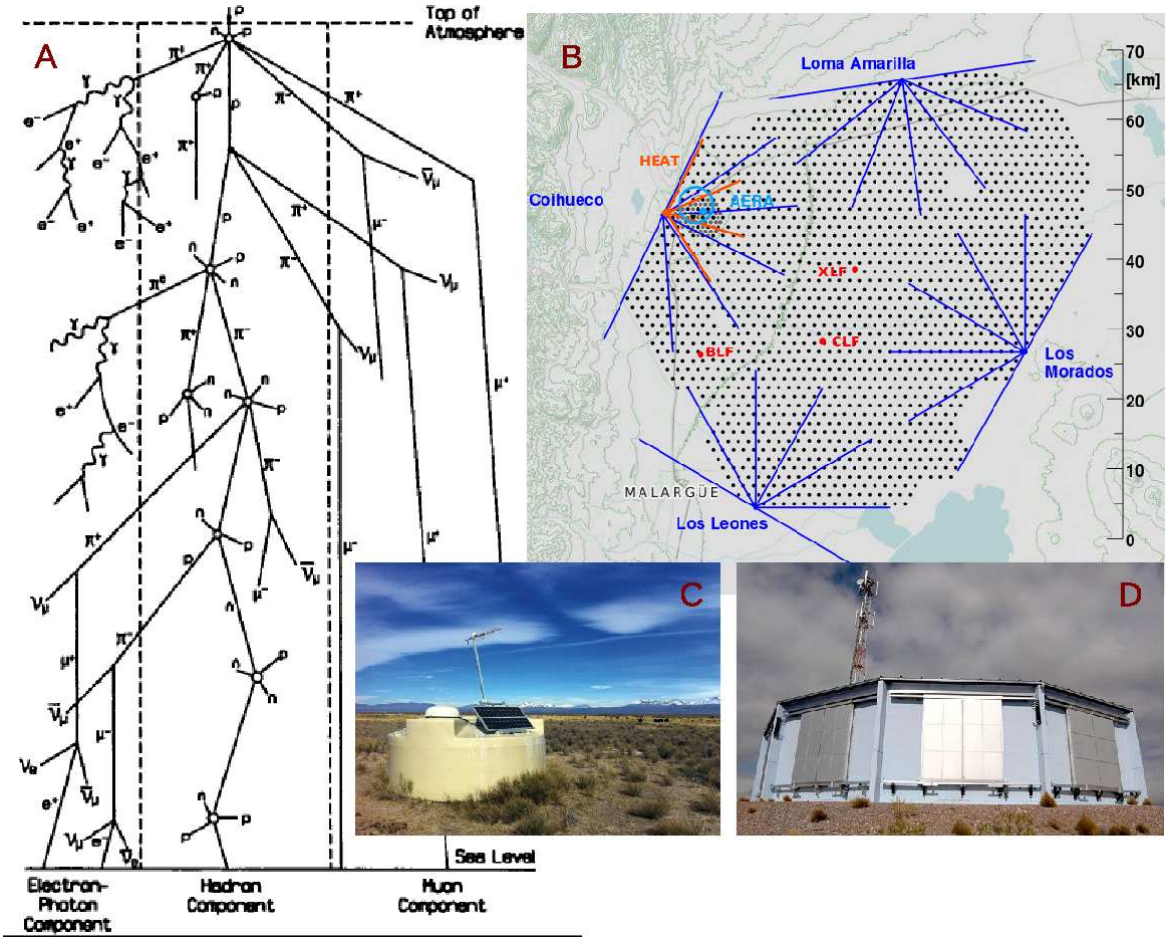


Figure 6: **A:** The scheme of the air shower development in the atmosphere with the soft (electrons and photons), the hadronic (neutrons, protons, pions and kaons), as well as the muonic components [9]. **B:** The schematic view of the Pierre Auger Observatory. *Black dots* represent the places of the water tanks with Cherenkov detectors, and *blue lines* show the covered area by fluorescence detectors. **C:** A photo about a water-filled Cherenkov detector. **D:** A photo of an ultraviolet photon detector.

The UHECRs produce ultraviolet (UV) photons in the wavelength range of 330 nm - 380 nm via the fluorescence of excited nitrogen molecules in the atmosphere. These interact with the incoming particles of the extensive air shower. The *blue lines* in the *panel B* and the *panel D* of Fig. 6 show the optical detectors, which track the longitudinal development of the air showers through the atmosphere by the detection of the generated UV photons at four measurement sites. A pair of fluorescence detectors measure the direction of the air showers within the angle of view of $30^\circ \times 30^\circ$ and up to the altitude of 15 km with high accuracy. Each of the optical detectors consist of a grid of focusing mirrors with the surface of $3.6 \times 3.6$ m$^2$, and the photon detectors consist of 440 photomultiplier tubes with the surface of $0.8 \times 0.8$ m$^2$.

The Pierre Auger Observatory covers the area of 3,000 km$^2$ on the Pampas of Argentina by the 1,660 water tanks as shown by the *black dots* in *panel B* of Fig. 6. The *panel C* of Fig. 6 shows a photo of a water tank. These tanks are placed 1,500 m far from each other. The energies of the particles are determined from photon signal amplitudes of the Cherenkov light in the water thank. The trajectories of the particles in the incoming air shower are reconstructed using the relative positions of different tanks, and the differences between the timing of the photon signals.

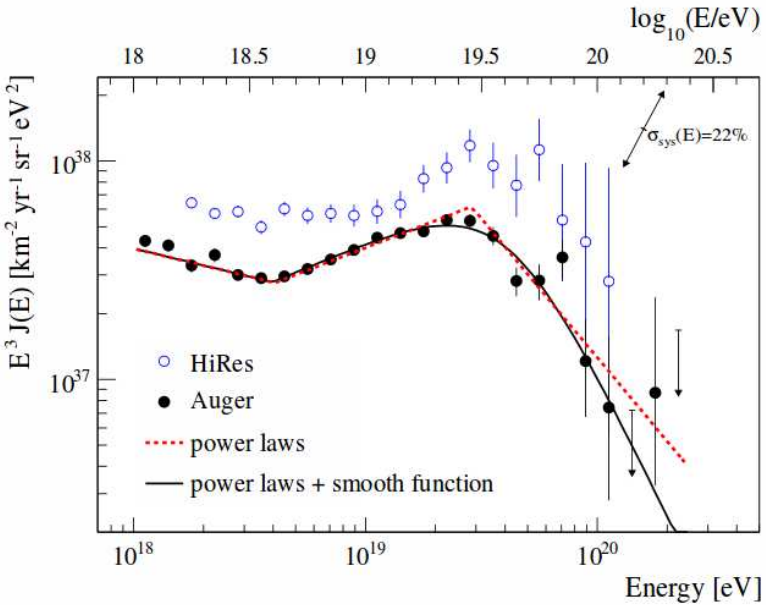


Figure 7: The energy spectrum of ultra-high-energy cosmic rays demonstrating the onset of the GZK cutoff [13].

One of the most important results of the Pierre Auger Observatory was the experimental confirmation of the existence of the GZK limit. Figure 7 shows the energy spectrum around the GZK limit [13]. This spectrum is suppressed by a factor of two around the value of $\log_{10}(E/eV) = 19.61 \pm 0.03$, that was expected from the GZK prediction.

## 1.4 Particle detectors for imaging

One can consider particle detectors as digital cameras, which take images about the investigated physical processes. Throughout the twentieth century, the discovery of new particles, and the evolution of detector technologies were accompanied with the appearance of new imaging techniques.

The first particle imaging technique was made possible by the discovery of X-rays. W. C. Röntgen imaged the hand of his wife to a photographic plate using X-rays in 1895. The application of the recent developments of particle physics, such as the well collimated and monoenergetic X-ray sources, the detector technologies and the software entered new feasibilities in medical, industrial, and homeland security applications by X-ray imaging. Figure 8 shows the wavelength and the energy spectrum of Röntgen photons, and the possible applications of hard X-rays (5 keV - 200 keV) [14].

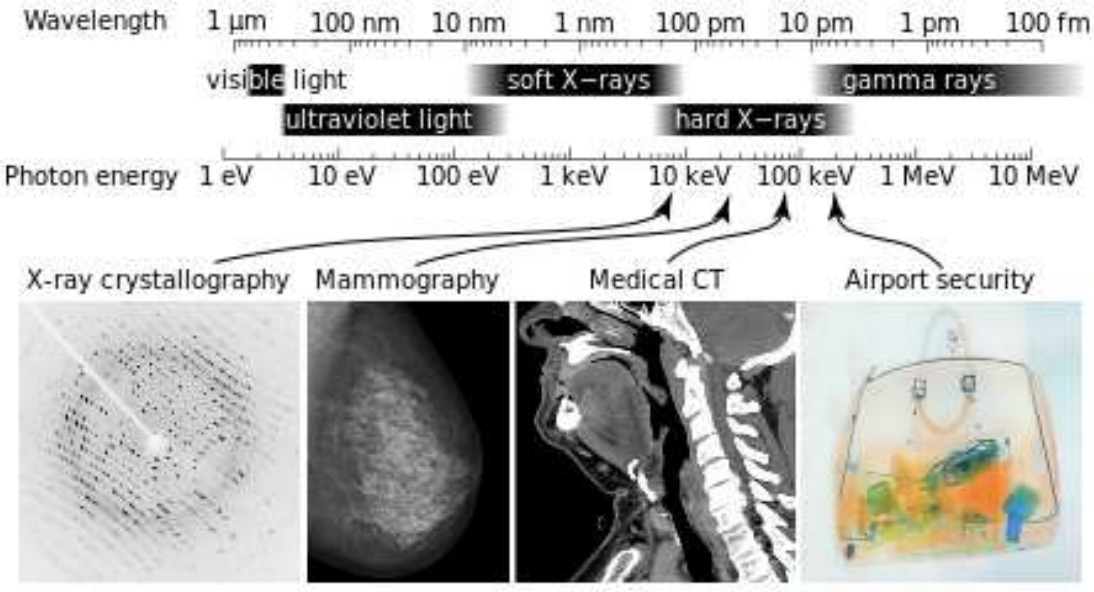


Figure 8: The energy spectrum of X-rays and the target of interests for hard X-rays (5 keV - 200 keV) [14].

In modern X-ray imaging systems, the "Röntgen photons" are generated by a vacuum tube: electrons are accelerated by high voltage (20-150 kV), and collide to the anode, such as tungsten or copper, which converts the electrons to Röntgen photons. The X-rays penetrate through the investigated object, and interact with it via photoabsorption, Compton scattering, or Rayleigh scattering. Thereafter, the X-rays are detected by photographic plates, scintillators, or ionisation chambers.

Different techniques are applied to extract the images about the investigated object. Computed Tomography (CT) takes 2-dimensional X-ray images of the investigated objects from different directions, and combines them into a 3-dimensional tomographic image.

The main disadvantage of X-ray imaging is the radiation dose, which limits the number inspections and their time. Moreover, the small penetration length ($< 0.5$ m), due to the relatively small energy of X-rays, is also a limiting factor to these measurements.

The positron emission tomography (PET) is applied for medical inspections, e. g. for oncology, neurology or cardiology [15]. PET can identify tumours at early stages. The growth of a tumour requires energy, which is taken from glucose. Therefore, the tracking of the glucose inside the human body provides information about the place of the tumour. At the start of the diagnosis, Fluorodeoxyglucose (FDG) is injected into the investigated body. The FDG molecules accumulate around the tumour, and decay to oxygen, and create positrons: $^{18}F \rightarrow ^{18}O + e^{+} + \nu_e$. The positrons annihilate with the electrons, and generate two 511 keV gamma photons in each annihilation. The gamma photons are emitted to the opposite directions and detected by scintillators or gaseous detectors. The PET image is reconstructed by the image slices taken from the different directions. PET is usually combined with Computer Tomography (CT) or more recently with Magnetic Resonance Imaging (MRI) to provide more reliable diagnosis. The PET/CT inspections have the radiation exposure of about 25 mSv, which dose is the half of the dose limit of a nuclear energy worker.

Cosmic rays are also applicable for imaging purposes, especially at large scales. Muon radiography (or shortly muography) deduces the density-length (average density $\times$ thickness) of the investigated object by the measurement of the cosmic ray muon flux along different paths through the object. Thereafter, the average density of the object is determined with the knowledge of thickness from geodetic measurements. The tomographic image of the investigated object is generated by the measurement of muon flux in different directions through it, similarly to the PET/CT imaging technique. This technique is called

muon tomography. The advantage of the application of the highly penetrating natural radiation for imaging purposes is twofold: the size of the investigated objects can reach up to kilometer scales and the objects are not damaged during measurements. Various types of tracking detectors are applied for muon radiography, e. g. scintillators, nuclear emulsions, or gaseous detectors.

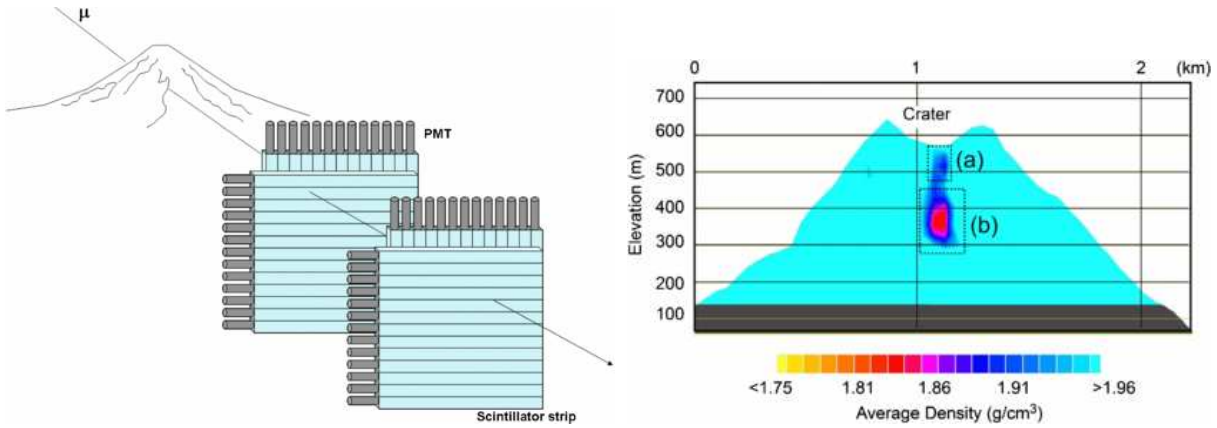


Figure 9: *Left:* The schematic view of the radiographic imaging of a volcano by scintillator detectors [19, 20]. *Right:* The density map of Mt. Iwodake was reconstructed from the measured muon flux. The low-density anomalies, ($a$) and ($b$) originate from volcanic gases and lava [19].

The applicability of muon radiography was demonstrated for various purposes: archaeological researches were performed inside pyramids [16], the presence of hidden caves were investigated above natural caverns [17], the density of a lava dome inside an active volcano was determined [18]. Figure 9 shows an example of the imaging of a volcano by a scintillator-based muon detector (*left*), and the density map reconstructed from the muon flux measured across the volcano (*right*) [19, 20].

To exploit the potential of cosmic ray muon radiography, the application oriented R&D of particle detectors, good understanding, and suppression of background particles (soft component, low energy muons and hadrons) are necessary.

The above presented imaging techniques demonstrated that particle detectors are applicable for the inspection of objects of very different sizes, from the human body up to the kilometer-size volcanoes. This thesis and my Ph.D. work were related to these research directions.

## 1.5 Thesis objectives

I joined the REGARD group (presently MTA "Lendület" Innovative Detector Development Group) in the Wigner Research Centre for Physics of the Hungarian Academy of Sciences in 2010, and the Budapest group of the ALICE Collaboration in 2012. My thesis work had two aims. One of them was to develop gaseous detectors for the ALICE experiment for the high-luminosity periods of the Large Hadron Collider. The another aim was the application oriented development of gaseous tracking systems for cosmic muon imaging. The thesis objectives are summarised in the following points.

- Investigating the performance and the ageing of ALICE High Momentum Particle Identification Detector during the first LHC period (2010-2013), and development of gaseous detectors for ALICE.
- Development and building of reliable, low-power, and portable tracking systems with optimised spatial and angular resolution for cosmic muon tracking and radiographic imaging.
- Cosmic muon imaging with gaseous detectors.

The thesis is organised as follows. Chapter 2 focuses on the review of gaseous detectors. In Chapter 3, my contributions to the ALICE experiment are summarised, and the ageing study of the High Momentum Particle identification Detector is presented. Chapter 4 reviews cosmic ray muon imaging. Chapter 5 focuses on the development of portable gaseous tracking systems for muon radiography. Chapter 6 presents the application of the developed portable muon telescope for underground measurements. In Chapter 7, a novel method is introduced to image low-$Z$, and small-size objects by cosmic muon tracking. Chapter 8 summarises the main thesis results.

# 2 Review of gaseous detectors

The present chapter focuses on gaseous detectors. These are applied specifically to measure the trajectory of charged particles. Owing to their low material budget and cost efficiency, gaseous detectors are widely used in particle physics as well as other applications. Here I provide information about the operation of gaseous detectors, highlight some important concepts, and as examples, I present two applications of the Multi-Wire Proportional Chambers in high-energy physics experiments.

## 2.1 The interaction of charged particles with gases

The detection of charged particles is based on their interaction with the gaseous medium. The electric field of the charged particle interacts with the gas atoms/molecules, and results both in atomic ionisation and excitation. The energy loss of charged particles via ionisation as a function of density-length, $L$ is described by the Bethe – Bloch formula [21, 22]:

$$-\Big(\frac{\mathrm{d}E}{\mathrm{d}L}\Big)_{ion} = 0.3071\frac{Z}{A}\frac{q_e^2}{\beta^2}\left[\ln\frac{2m_e c^2\beta^2\gamma^2 E_{max}}{I^2} - \beta^2 - \delta(\beta\gamma)\right] , \tag{1}$$

where $E$ is the kinetic energy of the incident charged particle, $q_e$ is the elementary charge, $\beta = v/c$ is the velocity of the particle in the units of speed of light, $v$ is the velocity of the particle in m/s units, $c = 3{\times}10^8$ m/s is the speed of light, $\gamma = 1/\sqrt{1-v^2/c^2}$ is the Lorentz factor of the particle, $E_{max} = 2mc^2\beta^2\gamma^2/(1 + 2\gamma(m_e/M) + (m_e/M)^2)$ is the maximal transferable kinetic energy for charged particle with $M$ mass, and $m_e$ is the electron mass. $Z$ is the atomic number, and $A$ is the mass number of the medium, while $I \approx Z \times I_0$ denotes the effective ionisation potential of the medium. The value of $I_0$ depends on the choice of the gas, and varies within the energy range of 10 eV - 25 eV. The $\delta$ is the correction factor of density effect caused by the polarisation of the medium [22]. Note that the Bethe – Bloch formula is valid for either solid or liquid media.

The energy loss per unit density-length depends on the velocity $\beta$ of the charged particle. Figure 10 shows the ionisation energy loss of different particles as a function of their momenta in solid, gaseous, and liquid media [22]. The $1/\beta^2$ term dominates the fast

decreasing part, the energy loss reaches a constant value around $\beta\gamma = 2$, and after that, it slowly increases above $\beta\gamma = 4$ (relativistic rise). The region with the constant energy loss is the so-called minimum ionising region, and the charged particles within this $\beta\gamma$ region are called Minimum Ionising Particles (MIPs). The average energy loss per unit density-length for MIPs is about 1-2 MeVg$^{-1}$cm$^2$.

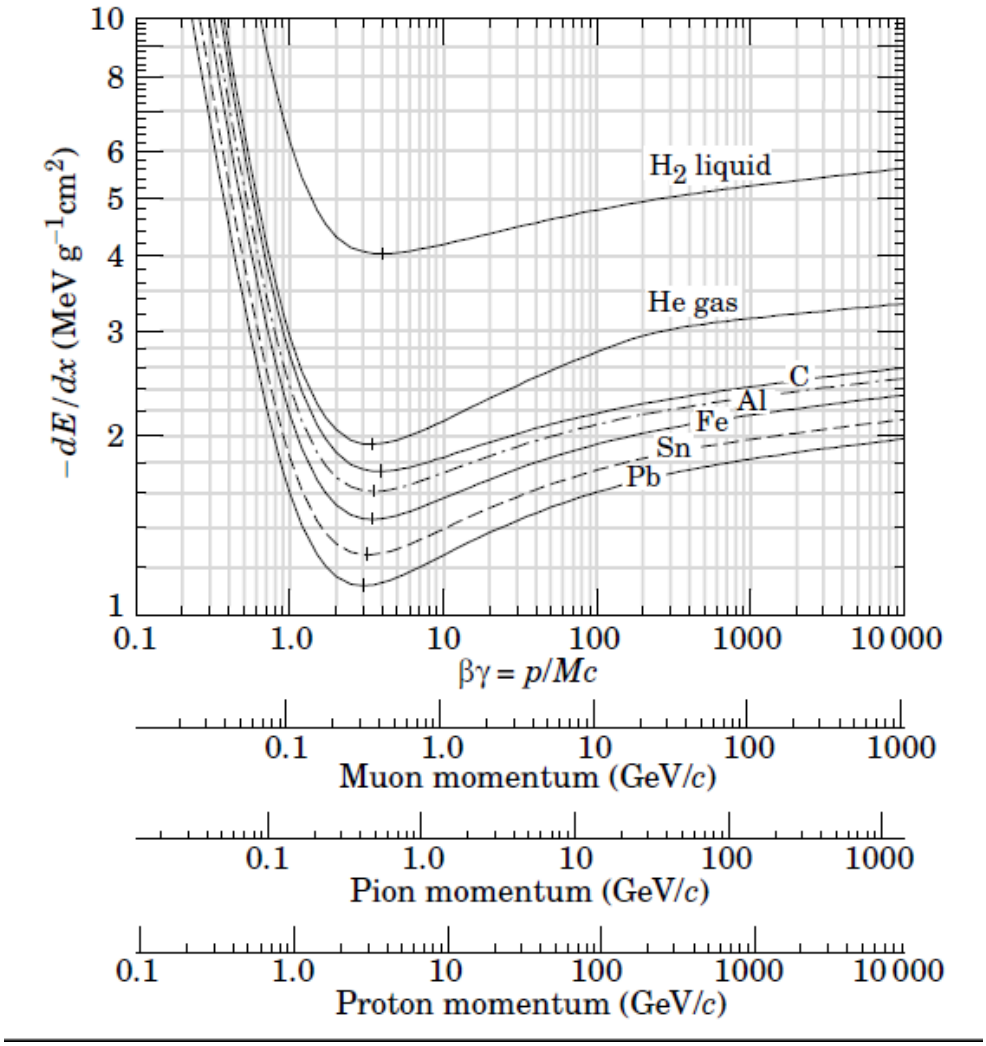


Figure 10: The ionisation energy loss ($-\mathrm{d}E/\mathrm{d}x$) of different charged particles across different media [22]. Note that the $x$ denotes the density-length in the figure.

The total ionisation energy loss is the result of discrete interactions between the charged particle and the atom. There are two kinds of the atomic collisions: the "close" collisions liberate the electric charges via ionisation due to the large energy transfer ($> 100$ eV),

and the "distant" collisions with small energy transfer induce both the ionisation (10eV - 100 eV) and the excitation ($< 10$ eV) of the gas atoms [23]. The electrons liberated by ionisation are called $\delta$-electrons. Due to the randomising effect of multiple collisions, the total range of electrons $R$ is approximated up to 1 MeV by the following formula [23]:

$$R[\mathrm{g/cm^2}] = 0.71(E[\mathrm{MeV}])^{1.72} \ , \tag{2}$$

where $R$ is given in g/cm$^2$ units, $E$ is the energy of the electron given in MeV units. For example, secondary electrons with an energy of 3 keV have 100 $\mu$m range in argon gas. The average energy loss is 2.5 keV/cm in argon in normal conditions. These electrons produce relatively large signals and the centre of gravity of the detected charge is systematically displaced. This effect limits the position resolution of the gaseous detectors to 20-30 $\mu$m at atmospheric pressure.

The energy loss as given by the Bethe – Bloch formula is usually small compared to the total energy of the charged particle, and it builds up from a relatively small number of interactions with a wide range of possible energy transfers. The distribution of the $\Delta E$ energy loss in thin media is approximately given by the Landau distribution [23]:

$$f(\lambda) = \frac{1}{\sqrt{2\pi}} \mathrm{e}^{-\frac{1}{2}(\lambda + e^{-\lambda})} \ , \tag{3}$$

where $\lambda$ denotes the normalised deviation from the most probable energy loss, called most probable value (MPV):

$$\lambda = \frac{\Delta E - \mathrm{MPV}}{\xi} \ , \tag{4}$$

where $\xi$ is the average energy loss given by the first term of Eq. (1). The Landau distribution starts similarly as a Gaussian function, but it has a long tail. The energy resolution of the gaseous detectors for the energy loss of fast particles is thus compromised because of the domination of the non-Gaussian statistics [23].

The total ionisation is produced by both of the charged particles and the secondary electrons. The total number of electron-ion pairs, $n_T$ created via ionisation is expressed by the following equation [23]:

$$n_T = \frac{\Delta E}{W_i} \ , \tag{5}$$

where $W_i$ is the effective average energy to produce an electron-ion pair. In case of gas mixtures, this can be calculated by a composition law [23].

## 2.2 Avalanche process in gaseous detectors

In high enough electric field, the secondary electrons accelerate and create further electron-ion pairs. The number of electrons increases exponentially along the path of the electrons. This leads to an electron avalanche, the so-called Townsend avalanche. In the electric field the created free electrons and the ions drift to the opposite directions to the proper electrodes. The electron avalanche generates a negative signal and the ions generate a positive signal. The *gas gain* is the ratio of the number of detected electrons on the positive electrode to the number of electrons produced in the ionisation process by the charged particle. In most types of gaseous detectors, electron avalanches are created. Different concepts of gaseous detectors apply various electrode configurations, resulting different gas gains, discussed below in Sec. 2.3.

The gaseous detectors are typically operated with continuous gas flow. This minimises the amount of incoming $O_2$ molecules and other electronegative contaminents which capture the secondary electrons, and thus reduce the gas gain and detection efficiency of charged particles.

The choice of the applied gas depends on the experimental requirements. These are sometimes conflicting operational parameters, such as high gain operation, low working voltage, fast signal production, high rate capability, or long lifetime [23].

The main component of the applied gas/gasmixture is usually a noble gas due to that electron multiplication in such gases is achieved with much lower electric fields than in polyatomic gases. The latter ones have many energy dissipation modes [23, 22]. The cost of xenon (Xe) and krypton (Kr) gases is relatively high, thus argon (Ar) is applied widely in gaseous detectors. However, argon has a low gas gain, and thus usually does not produce high enough signals for the readout electronics. The reason is as follows: the excited gas atoms return to the ground state, and emit photons with the energy of 11.6 eV. The energy of these photons is higher than the ionisation potential of any metal (e.g. 7.7 eV for copper). Consequently, photoelectrons (PEs) are emitted from the cathode, and a new avalanche is initiated.

Polyatomic molecules, mostly organic compounds like hydrocarbons or alcohols and inorganic compounds like carbon-dioxide ($CO_2$) or freon are applied as "quenching gases" to absorb the photons and the electrons emitted from the cathode. The efficiency of quenching increases with the number of molecules, thus very high gas gains are achieved. The dis-

advantage of the hydrocarbon gases shows up in high radiation environments, where they dissociate and interact with the detector material in an unfavorable way, thus contribute to the ageing of the detector. Practically, the mixture of three or four gases are applied to minimise these problems and to reach a high gas gain and stable operation of large detectors. The physical properties of the most commonly used gases in particle detectors at normal temperature and pressure are summarised in Refs. [22] and [23]. The secondary electrons lose their kinetic energy in multiple collisions with the gas atoms or molecules. Their diffusion is expressed by the following equation:

$$\frac{\mathrm{d}N}{N} = \frac{1}{\sqrt{4\pi Dt}}\,\mathrm{e}^{-x^2/(4Dt))}\mathrm{d}x \ , \tag{6}$$

where $\mathrm{d}N/N$ is the fraction of electrons found in the $\mathrm{d}x$ element at the distance $x$ from the origin after $t$ time, and $D$ is the diffusion coefficient. The standard deviation (RMS) of the distribution is $\sigma = \sqrt{2Dt}$. The diffusion coefficient depends on the choice of the gas, the temperature, density, etc. the velocities are measured to few $\mathrm{m}/\mu\mathrm{s}$. The ions move much slower than the electrons due to their much larger mass. When $\vec{E}$ electric field is applied in the gaseous detector, the electrons increase their energy between collisions. The drift velocity of electrons in gases can be approximated by Townsend's expression for low fields [22]:

$$\vec{v} = \frac{e\vec{E}\tau}{m_e} \ , \tag{7}$$

where $\vec{v}$ is the drift velocity, $e$ is the elementary charge, $\tau$ is the average time between the collisions, and $m_e$ is the mass of the electron, respectively. The ions move slowly along the direction of the electric field. The drift velocity is linearly proportional to the electric field over all the practical range. The drift velocity and the diffusion of electrons and of ions depend on the inelastic cross-section of the applied gas, which is determined by the rotational and vibration levels of the gas molecules [22]. In noble gases, such as in Ar or in Xe, the inelastic cross-section is zero at low energies due to their ionisation and excitation thresholds. Large drift velocities can be achieved by the application of polyatomic gases, such as $CO_2$ or $CH_4$. When a magnetic field is applied, the transverse component of the drift velocity is decreased by the Lorentz force.

## 2.3 Basic concepts of gaseous detectors

Several detector concepts were developed to measure the trajectories of charged particles. The present section focuses on three widely used concepts which are related to this thesis.

### 2.3.1 Multi-Wire Proportional Chambers

The first classical Multi-Wire Proportional Chamber was developed and built by G. Charpak at the end of 1960s [24]. This innovation revolutionised the electronic detectors in high energy physics, and G. Charpak received the Nobel Prize in 1992 for this pioneering development.

The MWPC consists of an anode wire-plane between two parallel cathode plates. The typical wire spacing is a few millimetres and the distance between the cathode plates is a few cm. Positive potential of a few kVs is applied on the anode wires to create a positive electric field inside the MWPC. The magnitude of the electric field in the drift region, $E_{drift}$ and at $R$ distance from the anode wires, $E(R)$ are given by

$$E_{drift} = \frac{CU}{2\epsilon_0 s} \ , \ E(R) = \frac{CU}{2\pi\epsilon_0}\frac{1}{R} \ , \ C = \frac{2\pi\epsilon_0}{\pi(d/s) - \ln(2\pi r/s)} \ , \tag{8}$$

where $U$ is the potential difference between the anode wires and the cathode, $s$ is the wire spacing, $\epsilon_0$ is the vacuum permittivity with the value of 8.854 $\times 10^{-12}$ F/m, $C$ is the capacitance per unit length of an anode wire, $d$ is the distance between the cathode and the anode wires, and $r$ denotes the radius of the anode wires [22].

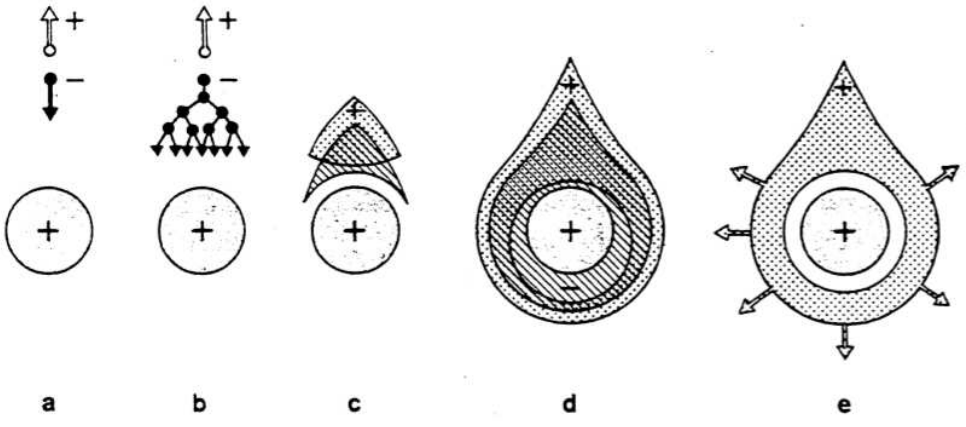


Figure 11: The schematic view of the signal generation on an anode wire of a MWPC [23].

Figure 11 shows a 2D view of the time development of an avalanche around an anode wire [23]. The electron produced by the ionisation of the charged MIP is accelerated in the electric field to the direction of the anode wire (*a*). When the electron approaches the anode wire to about the distance of few times of the radius of the wire, the electron avalanche starts to form (*b*). A drop-like avalanche is created and surrounds the anode wire (*c*-*d*). The electrons are collected on the wire within the time of about a few nanoseconds, and the ion cloud migrates to the direction of the cathode (*e*).

After charge collection, the signals are amplified and digitised by dedicated Front-End Electronics (FEEs). The digitised signals are transmitted to the data acquisition (DAQ) system, which is responsible for measurement control, data storage, and data analysis.

The low material budget, the high efficiency, the reasonable position resolution, and the relatively low price allowed that large size MWPCs are widely applied in various experiments, few of them is presented in Sec 2.4.

The disadvantages of the classical MWPC concept are the following. The wires are fixed by heavy support frames, which limit the portability and applicability. This arrangement is very sensitive for any distortion in detector geometry, both for distortions of the cathode planes and for inaccuracy in the wire distances. Figure 12 shows the equipotential surfaces of the electric field and the field lines inside a MWPC with a displaced wire. A geometrical inaccuracy leads to a change in the gas gain near the wire and deteriorates the uniformity of the MWPC.

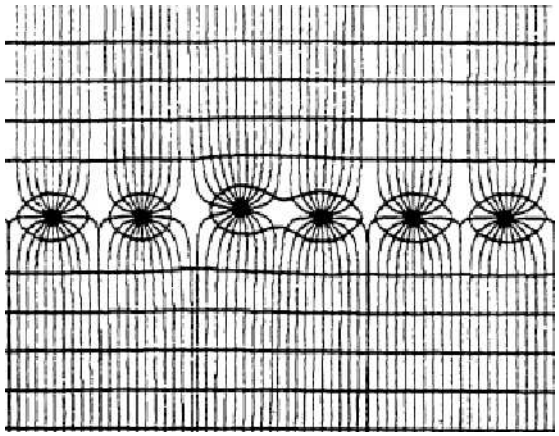

Figure 12: The equipotentials of the electric field and the field lines inside an MWPC with the wire thickness of 20 $\mu$m, the spacing of 2 mm, and the cathode distance of 2 cm. A small displacement of anode wires can cause the distortion of the electric field [23].

New variants of MWPCs can eliminate the problem caused by the mechanical inaccuracies. These were developed by the REGARD group. As the member of the research group, I participated in the development and construction of these novel chambers.

An asymmetric MWPC, called Close Cathode Chamber (CCC) was developed by D. Varga *et al.* in 2011 [25, 26]. The structure of the CCC is shown in the *left panel* of Fig. 13. The lower cathode is segmented into 4 mm wide pads, and the wire plane is placed at a distance of 1.5-2 mm above the lower cathode, perpendicularly to the pads. The wires are precisely positioned and glued into laser-engraved plastic bars. This arrangement provides insensitivity to mechanical distortions, e. g. to external tension or bulging effect. The CCC does not require the robust support frames of the MWPC detectors. The total weight of a chamber with the size of 0.5 $\times$ 1 m$^2$ is about 2 kg. A commercial, non-flammable and non-toxic mixture of Ar and $CO_2$ gases in portion of 82:18 (called FC18) is applied in CCC chambers. A gas flow of 0.5-1 L/h can keep the $O_2$ level under 1,000 ppm. The CCCs provide a reliable gas gain of about 5 $\times$ 10$^3$.

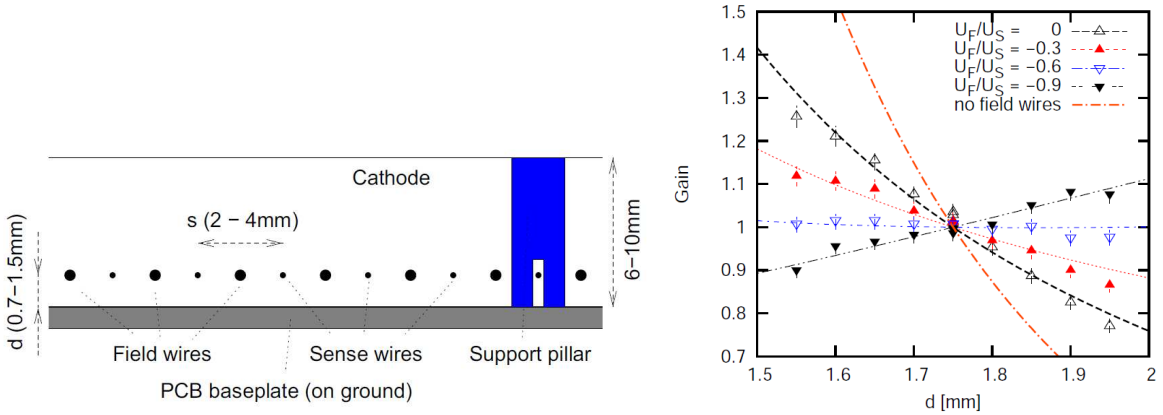


Figure 13: *Left:* Structure of a CCC detector [25, 26]. *Right:* The relative gas gain as a function of the distance ($d$) of the base plate and the wire plane. The independence on $d$ is demonstrated at the distance range 1.5 mm - 2 mm at $U_F/U_S = -0.6$ [25, 26].

There are two kinds of wires inside the CCC chamber. Gold-plated tungsten sense wires are used as anode wires with the diameter of 22-25 $\mu$m to collect the avalanche. Copper field wires with the diameter of 100 $\mu$m form the special electrostatic field in the CCC [25]. Analogue signals from both the field wires and the pads, are amplified and discriminated by FEEs, thus 2-dimensional spatial information is provided. Each sense wire is connected to a conductive line on the PCB, and the resulting signal can be used for triggering or

self-triggering. The typical applied high voltage (HV) is about $U_S$ = 1,050 V on the sense wires, and $U_F$ = -525 V on the field wires and on the cathode. The key advantage of the CCC concept is the gas gain independence on the flatness of the base plate [25]. There is a wide range of the wire-plane – baseplate distance (1.5 - 2 mm), where the gas gain is approximately constant with the appropriate choice of the ratio of the sense wire to the cathode high voltage, $U_F/U_S = -0.6$, as plotted in the *right panel* of Fig. 13 [25, 26].

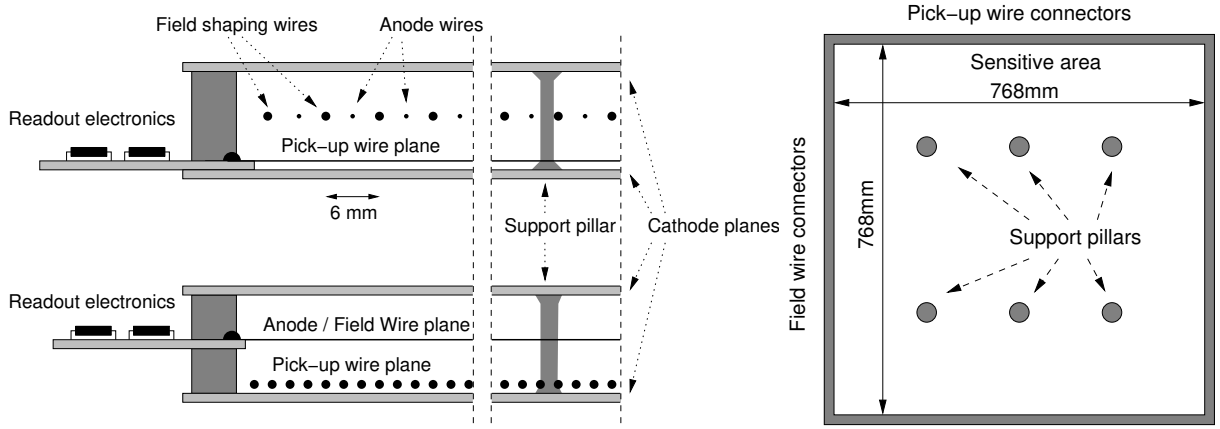


Figure 14: *Left:* Scheme of the presented new MWPC concept with the wire spacing of 12 mm for both anode- and field wires [OL01]. *Right:* The upper view of the new MWPC detector with the support pillars [OL01].

Another new variant of MWPC detector consists of two wire-planes, which are placed perpendicularly above each other to provide 2-dimensional position information [OL01, 27]. Therefore, this concept applies an additional wire-plane instead of the pads etched to the base plate. This solution decreases drastically the cost of the chamber and increases its size, which was limited by the production procedure of PCBs. This MWPC can also be operated with FC18 gas mixture. Figure 14 shows the structure of this new MWPC detector from the side views (*left*) and the upper view (*right*). The upper wire-plane consists of anode and field-shaping wires. This is placed in the middle of the chamber at the distance of 1 cm from the cathodes. Both kinds of wires are positioned with the spacing of 12 mm. The lower wire-plane consists of pick-up wires with the spacing of 4 mm. Every consecutive three pick-up wires are connected together and are read out as pads. The anode wires are similar to those as applied in the CCC. Both the pick-up wires and the field shaping wires are 100 $\mu$m thick copper wires. A high voltage of about 1,700 V is applied on the anode wires, while the field shaping wires and pick-up wires are on ground potential. Six support

pillars between the upper and lower cathodes provide better mechanical stability for the chamber. The weight of such an MWPC with the size of $0.8 \times 0.8$ m$^2$ is 6 kg.

This detector is insensitive for small ($\sim$ mm) inaccuracies in wire positioning. Instead of laser engraved plastic bars, the wires are soldered to PCBs, which simplifies the detector construction, and allows larger ($\sim$ m$^2$) size detectors to be built in a relatively shorter time frame (few days). More information about detector construction is provided in Sec. 5.2. These MWPCs apply the same FEEs and DAQ system as the CCCs. Both of them are presented in Sec. 5.3. Due to the low material budget and high tolerance against the mechanical distortions, both the CCC and the presented new MWPC detectors are very promising concepts for particle tracking and applications.

### 2.3.2 Resistive Plate Chambers

Another gaseous detector concept is the Resistive Plate Chamber (RPC), which is applied widely for charged particle tracking in High Energy Physics (HEP) [28]. Figure 15 shows the structure of a Glass Resistive Plate Chamber (GRPC) [29]. It consists of two parallel electrodes, which are sandwiched by conductive layers, e. g. graphite to provide the anode. One of the plates are made of high volume-resistivity material, e. g. glass with the volume-resistivity of $10^{12}$ $\Omega$ cm. Gas is filled between the two plates. The applied gas can be e. g. the non-flammable mixture of the following gases: Forane is applied for ionisation (93 %), isobutane is used for quenching the ultraviolet photons created via the excitation of Forane (5 %), and sulphur hexafluoride (2%) serves as a high voltage dielectric. Furthermore, an insulator, typically a Mylar foil is applied between the anode and the readout.

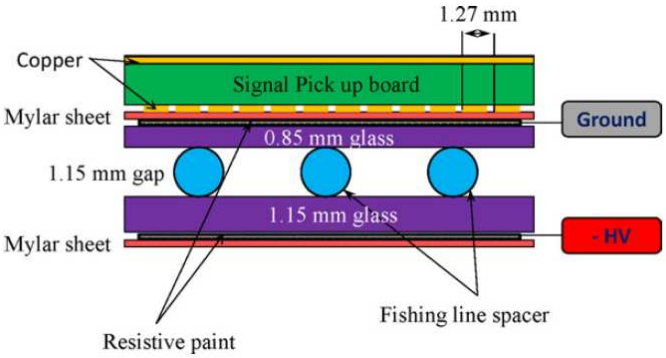


Figure 15: The structure of a Glass Resistive Plate Chamber (GRPC) [29].

The signal readout of RPCs are possible via 2-dimensional pads with the typical size of cm by cm which are assembled on a Printed Circuit Board (PCB). FEEs are attached on pad-by-pad, thus the number of electronic channels and power consumption of RPC increase with the area of the detector. The RPC detectors are widely used in HEP experiments because of the very fast signal production time (100-200 ps). These are applied mostly as trigger detectors or time-of-flight detectors to measure the velocity of particles.

### 2.3.3 Micro-Pattern Gaseous Detectors

The third general concept is the Micro-Pattern Gaseous Detector (MPGD). The first MPGD was a Gas Electron Multiplier (GEM). It was developed by F. Sauli in the middle of 1990s [30, 31]. Figure 16 shows a microscopic image of the structure of a GEM foil (*left*), and the electric field (*right*) created inside and around it. GEMs are made of kapton foil with holes etched into it. The typical diameter of the holes is about 70 $\mu$m and their distance is about 100-200 $\mu$m. Using different high voltages on the upper- and lower sides of GEM, an electric field is created inside the holes, and a gas gain of 10 is provided. To allow reasonable gas gain of $10^3$-$10^4$, three or four GEM foils are placed parallely under each other. The advantage of GEM detectors is high rate capability (up to 50 kHz/cm$^2$), high spatial resolution ($\sim$ 20-50 $\mu$m), low material budget, and flexibility.

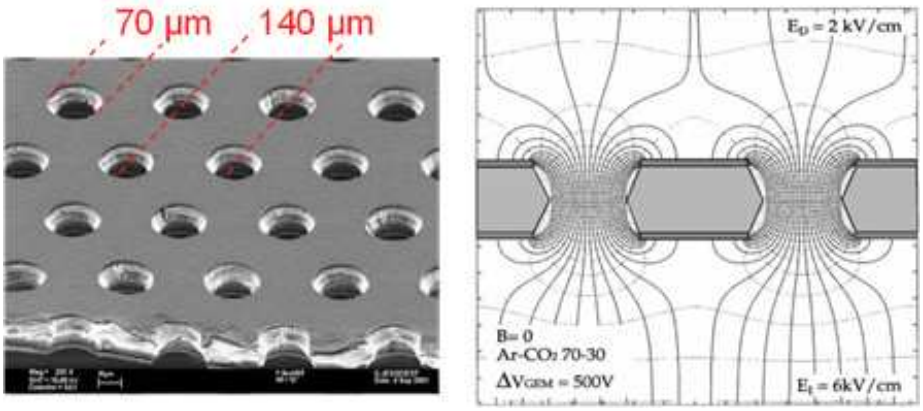


Figure 16: *Left:* A microscopic image of a Gas Electron Multiplier (GEM) with the hole size of 70 $\mu$m and hole distances of 140 $\mu$m [32, 33]. *Right:* Schematic field configuration around a single GEM layer generated by a high voltage difference of 500 V between its upper and lower sides [33].

Besides the GEM, there are further variants of MPGDs, such as Thick-GEM, Micromegas, or Ingrid [31]. The suitable hole size, the distance between the holes, the optimal hole patterns, and the electric field configurations are under investigation and optimisation. To maximise the efficiencies of MPGDs, the RD51 collaboration was established in CERN in 2008 for data exchange, share of the infrastructures, software tools, and the production technologies [32]. All the large LHC experiments will be upgraded before the high-luminosity LHC era using MPGDs. For example, the MWPC-based TPC of the ALICE will be replaced with a continuous-readout GEM-TPC, the forward tracking and the triggering of the Compact Muon Solenoid (CMS) will be performed with GEMs, and Micromegas will be applied in the forward muon tracking system of A Toroidal LHC ApparatuS (ATLAS).

## 2.4 Particle tracking and identification with gaseous detectors

The present section focuses on the applications of MWPCs in complex detector systems. Two particle identification detectors are presented here.

### 2.4.1 Time Projection Chambers

The Time Projection Chamber was developed for 3D particle tracking by D. R. Nygren [34]. The TPC consists of a large gas or liquid detection medium inside of a field cage with cylindrical or square shape. It is closed by the readout chambers, such as MWPCs or GEMS. When the charged particles penetrate through the TPC, they ionise the medium, and produce electrons, which drift towards the readout chambers and provide two-dimensional positional information. The third dimension is obtained by the measurement of the detection time relative to the interaction time set by a separate trigger detector.

The *left panel* of Fig. 17 shows the structure of the cylindrical ALICE TPC detector [35]. It is the largest TPC in the world with the total active volume of about 90 $m^3$ filled with Ne-$CO_2$ gas mixture in a portion of 90:10. The ALICE TPC has 72 MWPC-based readout chambers placed as endplates.

Particle identification can be performed by the TPC with the measurement of momentum of particles and the energy deposit inside the detection medium. The momentum and the charge sign are determined by a helix fit in the presence of the magnetic field. The energy loss is calculated from the measured charge distributions along the track on each

detector segment. The *right panel* of Fig. 17 shows how the ALICE TPC identifies the charged particles produced in p-p collisions the $\sqrt{s_{NN}} = 13$ TeV centre-of-mass energies per nucleon pair [36].

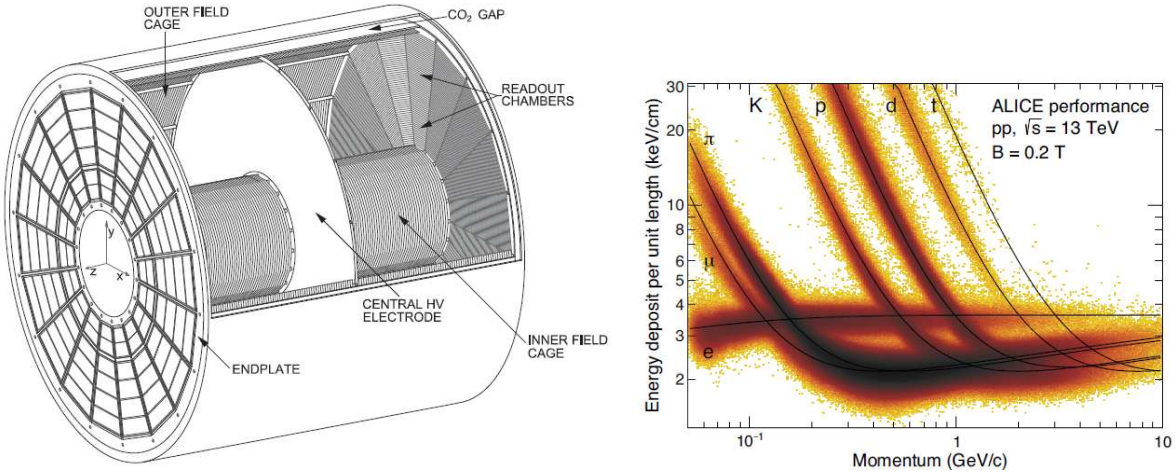


Figure 17: *Left:* The structure of the ALICE TPC with its cylindrical field cage [35]. *Right:* The ALICE TPC identifies charged particles by the measurement of their ionisation energy loss and measures their momentum from the bending in the magnetic field. The energy loss per unit length is plotted as function of momentum for different particles produced in p-p collisions with the $\sqrt{s_{NN}} = 13$ TeV centre-of-mass energies per nucleon pair [36].

The MWPC-based readout chambers of the ALICE TPC are operated with a gating grid [35]. When the TPC receives a trigger signal, the gating grid switches to transparent mode to allow the ionisation of electrons close to the anode wires of the MWPCs. After the time of 100 $\mu$s, an alternating voltage is applied on the gating grid to close it. This prevents the drift of electrons from the drift region to the amplification region, and the backflow of the ions from the amplification region to the drift region, which causes the distortion of the electric field in the TPC. The gating grid limits the measurable event rate of few kHz, which is above the typical Pb-Pb collision rate of about 3.5 kHz measured during the first LHC period (2010-2013). However, from the so-called high-luminosity LHC periods, the event rate will be increased up to about 50 kHz, which results the pileup of the events (tracks from different events measured as one event). This effect would lead to the loss of data. Consequently, the continuous operation of the TPC and the minimisation of the backflow of ions are necessary from the high-luminosity LHC periods. This fact motivates the application of GEM foils instead of MWPCs in the ALICE TPC [35].

### 2.4.2 Ring Imaging Cherenkov detectors

Gaseous detectors are also used in Cherenkov photon detectors for measurement of the velocity of charged particles. When the velocity $v$ of a charged particle is greater than the speed of light in the detector medium, the medium emits a certain type of electromagnetic radiation, called Cherenkov radiation. This radiation appears at a given angle $\theta_C = \arccos(c/(nv))$, where $n$ is the refractive index of the medium. The velocity of the particle can then be determined by the measurement of the Cherenkov angle:

$$v = \frac{c}{n\cos(\theta_C)}. \tag{9}$$

The so-called proximity focusing configuration is a widely used concept in Ring Imaging Cherenkov (RICH) detectors. The Cherenkov effect is obtained in a radiator of a few cm thickness and the photons are emitted along a cone pass through a somewhat thicker proximity gap, which are detected as a ring by a photon detector. The thickness of the ring depends on the thickness of the applied radiator. The radius of the ring depends on thickness of the proximity focusing gap and the emission angle of Cherenkov photons. Therefore, one can measure the velocity of the particles by the reconstruction of Cherenkov ring, the calculation of the Cherenkov angle and the knowledge of the refractive index of the radiator.

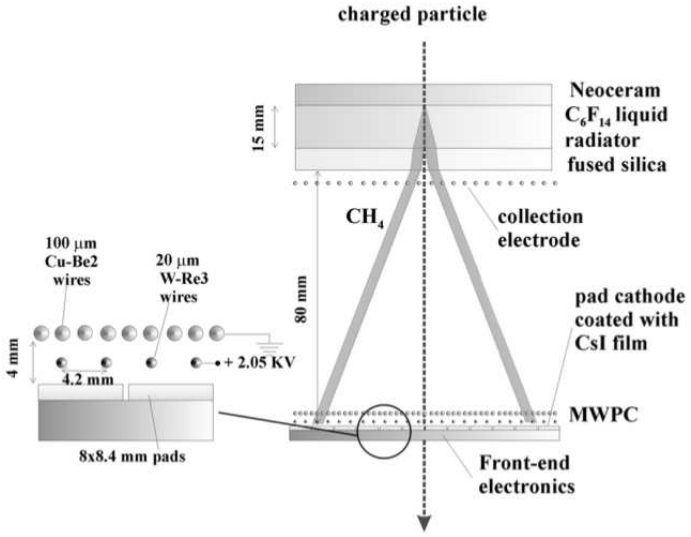


Figure 18: The proximity focusing geometry is applied for Cherenkov light detection in the ALICE HMPID [37].

Figure 18 shows the structure of a RICH detector, which applies proximity focusing configuration. This is the High Momentum Particle Identification Detector (HMPID) in ALICE [37]. Cherenkov photons are created in a liquid radiator. After a 80 mm thick proximity focusing gap, the photons are converted to photoelectrons in pads coated with caesium iodide (CsI) and the single photoelectrons create an electron avalanche inside an MWPC to produce a measurable signal on the pads.

As presented above, the momentum of charged particles are measured by the TPC in the ALICE detector. This allows the HMPID to identify charged hadrons on track-by-track basis. The identification of charged hadrons is obtained by the calculation of their mass, $m$ by the following expression:

$$m = p\sqrt{n^2 \cos^2(\theta_C) - 1}, \tag{10}$$

where $n$ is the refractive index of radiator and $\theta_C$ is the measured Cherenkov angle. Figure 18 presents the hadron identification capability of HMPID in p-Pb collisions at $\sqrt{s_{NN}} = 5.02$ TeV centre-of-mass energies per nucleon pair [38]. More technical details are provided about the HMPID detector in Sec. 3.1.

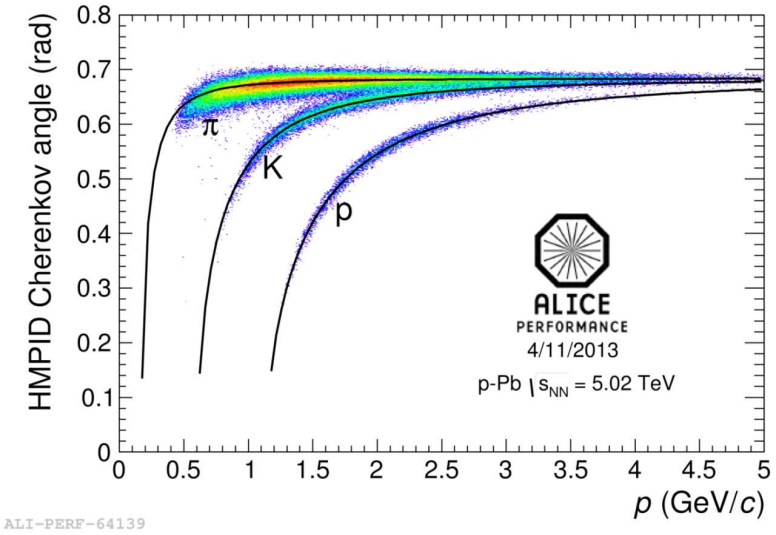


Figure 19: The identification of charged pions, kaons and protons is performed by the ALICE HMPID and TPC detectors in p-Pb collisions at $\sqrt{s_{NN}} = 5.02$ TeV centre-of-mass energies per nucleon pair [38].

# 3 Research and development of gaseous detectors for ALICE

The ALICE experiment at the LHC was designed to study the properties of the quark gluon plasma via the study of heavy-ion collisions [5]. The excellent tracking and particle identification capabilities of ALICE were demonstrated in Pb-Pb collisions. In the LHC Run 1 period (2010-2013) the ALICE experiment recorded Pb-Pb collision data with an integrated luminosity of 0.16 $nb^{-1}$ [39]. After the first long-shutdown (LS1), Run 2 allows to approach the integrated luminosity of 1 $nb^{-1}$. After the second long-shutdown (LS2) this is expected to increase to 10 $nb^{-1}$ with the rate of 50 kHz in Pb-Pb collisions. The upgrade of the present system and the design of new subdetectors are necessary to fully exploit the scientific potential of the LHC during the High Luminosity runs after the LS2.

As a member of the ALICE collaboration, I contributed to the upgrade of the TPC detector [35], where the present Multi-Wire Proportional Chamber readout plane will be replaced with Gas Electron Multipliers, as presented in Sec. 2.4. I contributed to the beam test measurements of the GEM foils at the CERN Proton Synchrotron (PS) and at the CERN Super Proton Synhcrotron (SPS) in 2014 [OL02]. I contributed to the construction of a Close Cathode Chamber based GEM gain scanner. This device was specifically developed for the quality assurance of GEM foils by the measurement of their gas gain map. I contributed to the development of a planned, future subdetector, the so-called Very High Momentum Particle Identification Detector (VHMPID) [OL03, OL04, OL05]. The VHMPID is a Ring Imaging Cherenkov detector, which can extend the track-by-track PID capabilities of ALICE up to the momentum of 25 GeV/c. This detector system allows the determination of hadron specific effects in parton fragmentation, in jet formation, and the improvement of our understanding of the hadronisation process. The VHMPID concept applies Close Cathode Chambers to detect charged particles by their Cherenkov radiation. I contributed to the construction and the test measurements of the CCCs at the CERN PS. The decision about the installation of the VHMPID within ALICE was postponed after the LS2.

There is no possibility to upgrade all subdetectors of ALICE during the LS2 due to the schedule of the upgrade of the experiment. The study of the performance and the ageing of these subdetectors is necessary in order to decide about their operation during the LHC Run3. One example is the High Momentum Particle Identification Detector. The study of the ageing of this detector helps to estimate its future PID capability. The HMPID applies the first large size CsI photon converters, and operates them in the highest energy collisions. The CsI photocathodes (PCs) of HMPID were produced by the RD26 collaboration at the end of 1990s [40]. The ageing study provides useful information to the development of the next generation of RICH detectors.

The present chapter focuses on my contributions to the HMPID detector of the ALICE experiment. I developed an analysis method to measure the performance of the HMPID in p-p, p-Pb and Pb-Pb collisions [OL06]. I estimated the ageing of the HMPID during the LHC Run 1 using Monte Carlo simulations [OL07].

Section 3.1 and Sec. 3.2 describe the structure and the operation of the HMPID detector. The developed analysis and simulation methods are presented in Sec. 3.3, and in Sec. 3.4. The results extracted from the Run 1 data are presented in Sec. 3.5. Section 3.6 summarises the results and the future perspectives.

## 3.1 The High Momentum Particle Identification Detector

The HMPID is the largest Ring Imaging Cherenkov counter existing with its total sensitive area of 11 $m^2$ [37]. The HMPID identifies charged hadrons on a track-by-track basis via the measurement of the emission angle of Cherenkov photons. Charged pions and kaons can be identified with $3\sigma$ separation in the momentum range 1 GeV/c - 3 GeV/c. (Anti)protons can be distinguished from kaons in the 1.5 GeV/c - 5 GeV/c range. Thus the HMPID improves the PID capabilities of the ALICE in the momentum region above 2 GeV/c, where the other PID detectors can not identify charged hadrons precisely. It is combined with the ITS, the TPC, the TOF, and the TRD to identify charged hadrons in the entire momentum range and to determine their spectra and ratios.

The HMPID consists of an array of seven identical RICH modules installed on an independent support frame. It is mounted at the two o'clock position on the ALICE space frame in a cupola-like structure. It is placed at 4.7 m distance from the interaction point. The HMPID acceptance covers the region of $|\eta| < 0.6$ in pseudo-rapidity.

The modules are based on the proximity focusing configuration presented in Sec. 2.4 and shown in Fig. 18. The RICH modules are described briefly in the following points [37].

(i) **Liquid radiator:** The Cherenkov photons in a RICH module originate from a 15 mm thick Neoceram radiator tray capped with 5 mm thick fused silica optical quartz windows. The radiator contains perfluorohexane (tetradecafluorohexane, $C_6F_{14}$) liquid with a refraction index of $n = 1.29$ at $\lambda = 190$ nm. This refraction index corresponds to a maximum velocity value, $v_{threshold} = 0.77$c. The water and oxygen contamination of the radiator are monitored and kept below 10 ppm [41].

(ii) **Photoelectron detector:** After the 80 mm thick proximity focusing gap, a Multi-Wire Proportional Chamber is applied for photoelectron detection. The MWPC is filled with pure methane gas. A high voltage of 2,050 V is applied on the anode wires to provide the designed gas gain of about $4 \times 10^4$, and to achieve an excellent ($> 90$ %) photoelectron detection efficiency. The MWPC is divided to six high voltage sectors, each with an area of $128 \times 20$ cm$^2$. Furthermore, the MWPC has six photocathodes with the sensitive area of $64 \times 40$ cm$^2$. The PCs are coated with 300 nm thick CsI layers to convert the Cherenkov photons to photoelectrons in the UV range (140 nm - 210 nm). Each CsI coated photocathode is segmented into $8.0 \times 8.4$ mm$^2$ pads. Figure 20 shows the schematic of the HMPID detector with the seven RICH modules segmented into PCs and the production date of the PCs.

(iii) **Front-End Electronics:** There are 161,280 Front-End Electronics (FEE) channels in the HMPID altogether. The FEEs are based on two Application-Specific Integrated Circuits (ASICs) [42]. An analog multiplexed low-noise signal processor and a readout processor are applied for the zero suppression of the collected data and for the calibration of charge distributions via subtraction of the pedestal. In the present system, the number of malfunctioning FEE channels is less than 0.2 % of the total number of channels. The average noise was measured on each FEE channel and it was found to be about 1,000 electrons input equivalent per channel. The data is read out with Detector Data Links (DDLs).

(iv) **Detector Control System (DCS):** The RICH modules are controlled and monitored by the DCS [43]. It ensures safe and synchronised operation of low voltage (LV) and high voltage supplies, the liquid circulation system, the gas and cooling systems. Any change in detector operation is archived and stored for offline reconstruction.

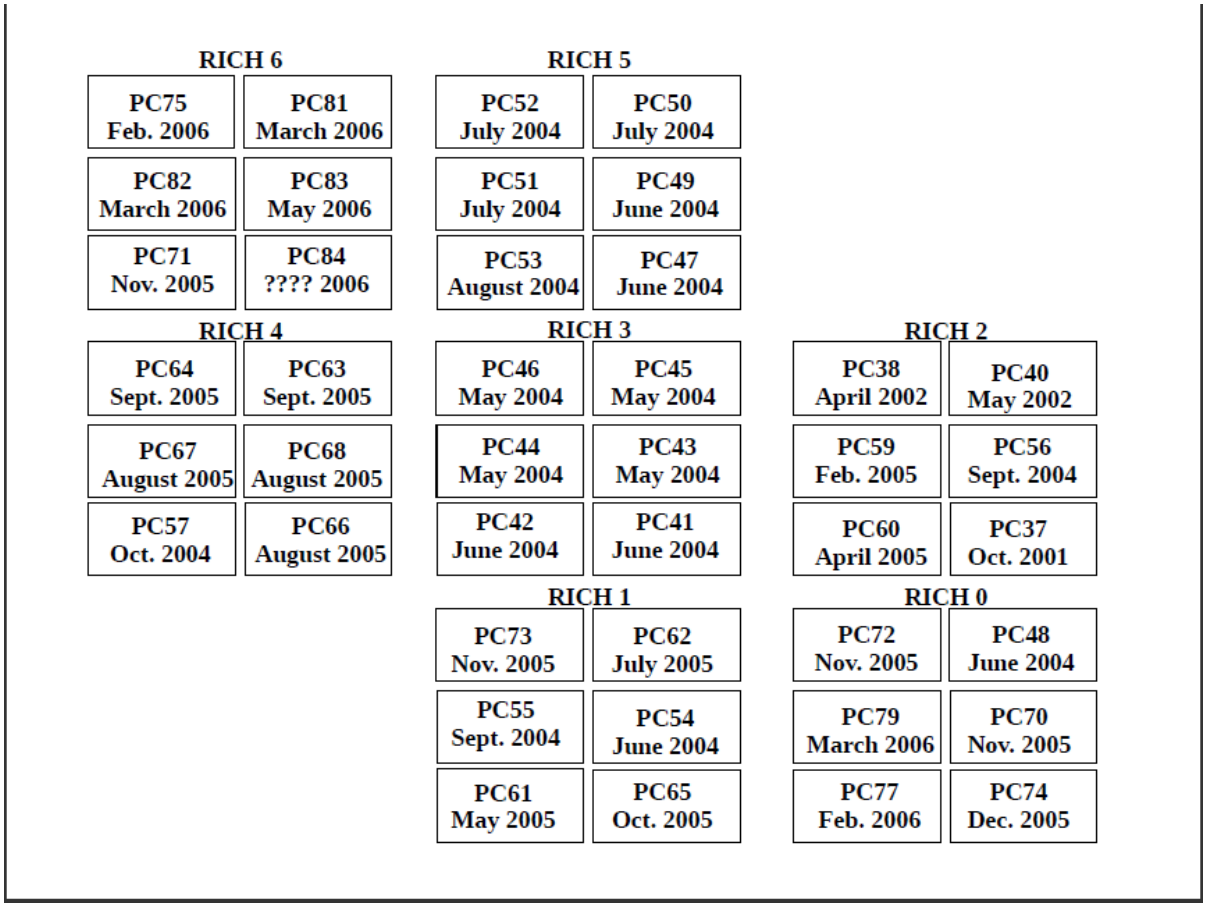


Figure 20: The schematics of the HMPID modules. Each module is segmented into six photocathodes. The PCs were produced between 2001 and 2006 [OL06].

(v) **Liquid circulation system:** Its purpose is to purify the $C_6F_{14}$, fill and drain the radiator vessels remotely, safely at a constant flow of 4 L/h, and empty them independently. In order to minimise the evaporation of $C_6F_{14}$, the liquid system was operated in stagnant mode during the data taking periods and in circulation mode during the LHC technical stops or p-p runs.

(vi) **Gas system:** A RICH module has a total volume of 200 L. It is filled up with $CH_4$ during operation periods and with Ar during technical stops. The gas pressure is kept at 2-3 mbar above atmospheric pressure.

## 3.2 The operation of the HMPID detector

The present section focuses on the operation of the HMPID. Here, the signal generation processes and the extracted signals are presented.

The charged hadrons create the Cherenkov light inside the liquid radiator. These hadrons are closely minimum ionising particles. The MIPs penetrate through the liquid radiator and the proximity focusing gap to the MWPC. The charged hadrons generate about 20 primary electrons inside the 4 mm thick methane gas, thus these result about 20 times higher signals than the single photoelectrons created via photoconversion.

Some of the Cherenkov photons are absorbed in the radiator, reflected at the radiator-quartz window or at the quartz window-gas boundaries. The radiator transparency is the ratio of the number of the emitted photons to the total number of the produced photons. The radiator transparency, $T(E)$ decreases with the energy of the Cherenkov photons, $E$. This is expressed by the following equation:

$$T(E) = E^{-L_{rad}/L_{abs}(E)} \ , \tag{11}$$

where $L_{rad}$ is the thickness the radiator, and $L_{abs}(E)$ is the absorption length of the Cherenkov photons which depends on their energy.

The conversion of the Cherenkov photons occur via the photoelectric effect in the upper 60 nm of the CsI pads. CsI is a relatively efficient photoconverter with the quantum efficiency (QE) of about 0.25 for photons at 175 nm wavelength. (Quantum efficiency measures the ratio of the number of photons that create a photoelectron (PE) to the total number of photons that entered the material.) In addition, CsI has low electron affinity[1], low photoelectron energy ($E_a$ = 0.1-0.2 eV), and large electron escape length (e.g. it is 16 nm for 1 eV electrons). If the energy of the photons are greater than the photoelectric threshold energy of the CsI (the sum of the bandgap energy and the electron affinity energy), the created photoelectrons are emitted from the CsI [44]:

$$\frac{hc}{\lambda} \geq E_g + E_a \ , \tag{12}$$

where $h$ is the Planck constant, $\lambda$ is the wavelength of the photons, $E_g$ is the bandgap energy. The threshold energy is about 6.2 eV, the corresponding threshold wavelength is 210 nm. The QE increases from zero at the threshold wavelength to up to 0.35-0.4

[1]The electron affinity is a chemical process in which an electron and a neutral atom form a negative ion, and produce energy.

measured at the wavelength of 160 nm. This upper wavelength (energy) limit of the HMPID for UV photon detection is set by the collection electrode frame located 4 mm below the quartz window. The ageing of photocathodes of the HMPID can be quantified via the determination of the quantum efficiency of the CsI surface. The following processes cause the ageing of CsI surface [45]:

(i) **Exposure to humidity:** Humidity causes hydrolysis of the CsI surface. The heat enhanced PCs are more stable to air exposure. The $H_2O$ level of the CsI PCs have to be kept below 10 ppm during transportation, storage, and operation.

(ii) **Intensive photon flux:** UV photons cause dissociation of the CsI molecules, and this leads to the so-called enrichment of the CsI surface: $h\nu + CsI \rightarrow Cs^+ + I + e^-$. Therefore the iodine atoms evaporate and the remaining Cs excess increases the electron affinity, which leads to the reduction of the quantum efficiency.

(iii) **Ion bombardment** also contributes to the enrichment of the CsI surface. The main cause of ion bombardment is the avalanches inside the MWPC.

At the place of the photoconversion, a non-negligible loss in the number of photoelectrons is caused by the Fresnel reflection of the Cherenkov photons on the surface of the CsI covered PCs [46]. The probability of the Fresnel reflection can be calculated from the complex refractive index of the CsI. The complex refractive index depends on the roughness of the surface of CsI. The roughness is defined by the following expression [46]:

$$S_r = e^{-4\pi \cos(\theta_0)\sigma_r/\lambda} \quad , \tag{13}$$

where $S_r$ is the correction factor of the surface roughness, $\theta_0$ is the incident angle of photons, $\sigma_r = 20$ nm is the roughness parameter, and $\lambda$ is the photon wavelength.

After the photoconversion, the emitted PE creates an electron avalanche inside the MWPC. The electron avalanche is also detected by the pads. The fired pads form the clusters. The sum of the amplitude of the analog signal read out from the fired pads is called photoelectron cluster charge. The lowest signal amplitudes have the highest probabilities, since the cluster charges follow an exponential distribution [37]. The single photoelectron efficiency is calculated from the gas gain by the following expression:

$$\varepsilon_{det} = e^{-A_{th}/A_0} \quad , \tag{14}$$

where $A_{th} = 3$ or 4 is the common ADC threshold of the Front-End Electronics, and $A_0$ is the gas gain in Analog-to-Digital Converter (ADC) units. 1 ADC count is equal to the

charge of 1060 electrons (0.17 fC). Note that the optimisation of the gas gain of MWPC is crucial because of the photon feedback mechanism: at higher gas gain ($\sim 10^5$), the avalanche emits photons isotropically, these photons produce additional photoelectrons in the CsI, and these created photoelectrons produce noise clusters in the photocathode.

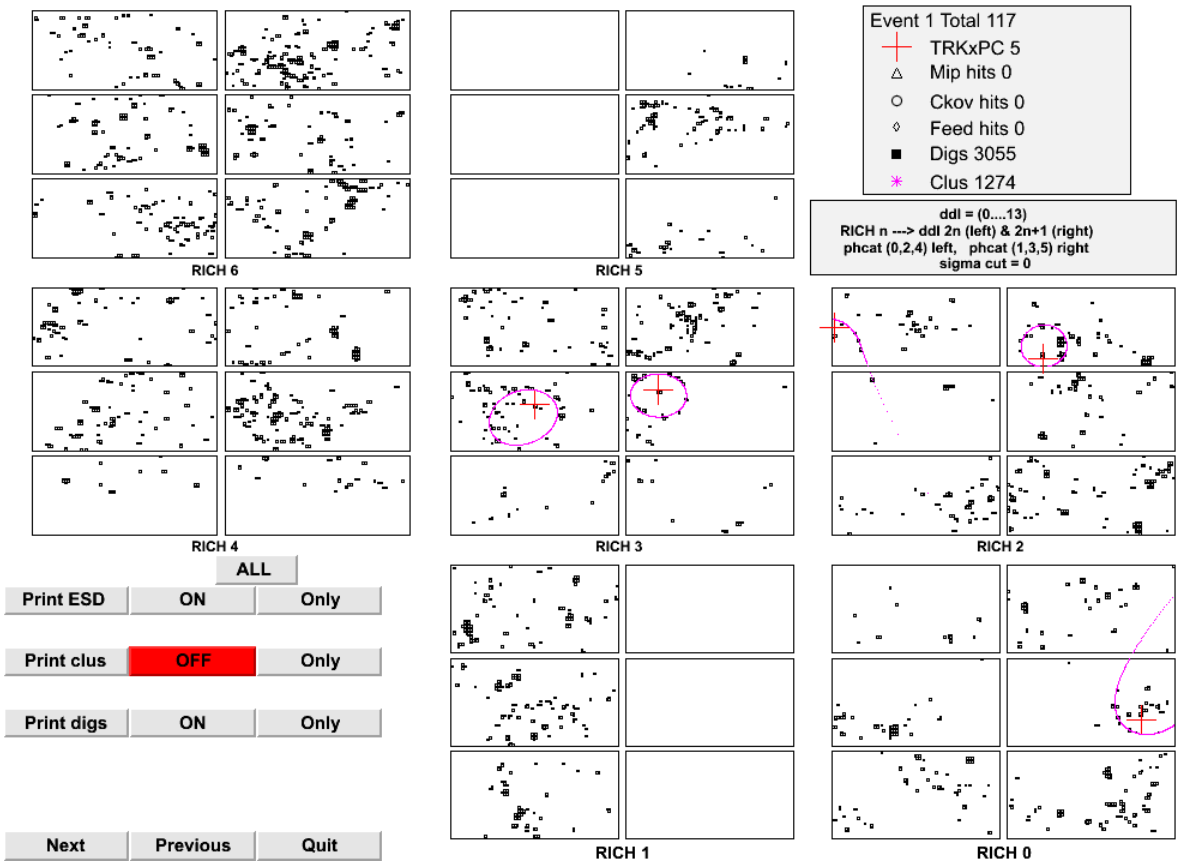


Figure 21: The event display of the RICH modules with an event produced in a Pb-Pb collision at $\sqrt{s_{NN}} = 5.02$ TeV centre-of-mass energies per nucleon pairs.

The photoelectron clusters are detected along the Cherenkov ring. Figure 21 shows the event display with the detected photoelectron clusters along the Cherenkov ring (*purple lines*) and with the detected tracks (*red crosses*) produced by Pb-Pb collisions at $\sqrt{s_{NN}} = 5.02$ TeV centre-of-mass energies per nucleon pairs. The number of PEs per Cherenkov ring, $N_{PE}$ is calculated by the following equations:

$$N_{PE} = L_{rad} N_0 \sin^2(\theta_C) \ , \tag{15}$$

where $L_{rad}$ is the thickness of the liquid radiator and the factor, $N_0$ is the so-called figure

of merit:

$$N_0 = 370\,\varepsilon_{det} \int_{E_{min}}^{E_{max}} QE(E)\,T(E)\,\mathrm{d}E \quad , \tag{16}$$

where $E$ is the energy of Cherenkov photons, $E_{min} = 5.5$ eV is the minimum energy, $E_{max} = 8.5$ eV is the maximum energy, $QE(E)$ is the quantum efficiency of the CsI surface, $T(E)$ is the measured transparency of the liquid radiator, and $\varepsilon_{det}$ is the single PE detection efficiency.

The physical processes presented above were implemented in the Monte Carlo simulation of the HMPID detector, called RICHSIM, which was developed by the HMPID group [46, 47].

## 3.3 Description of the data analysis method

I developed analysis methods to quantify the main performance parameters (gas gain, single photoelectron detection efficiency, and the number of photoelectron clusters) of the HMPID, and to determine the ageing of the CsI coated photocathodes. The data analysis was performed in p-p and p-Pb collision data sets of the different LHC periods of the Run 1. I run Monte Carlo simulation of the HMPID to reproduce the measured number of photoelectron clusters, $N_{PE}$ and to extract the quantum efficiencies of the PCs.

The data analysis was performed at the Event Summary Data (ESD) level in minimum bias triggered events within the ALICE off-line analysis framework, called AliRoot [48]. ESD is the output of the reconstruction, which contains only high level information about the charged particles with their PID information, e. g. the position of the event vertex and the secondary vertex candidates. An analysis task is used to read ESDs, and to fill a Root TTree object with all of the relevant information about the tracks, and the photoelectron clusters [49]. Table 1 lists the analysed periods with their time intervals, the type of collisions with specified centre-of-mass energies per nucleon pairs, as well as the common thresholds of the FEEs in ADC units, and the number of reconstructed tracks. The periods highlighted with bold fonts were used to extract the quantum efficiencies of the photocathodes. The analysed periods were selected after the global Quality Assurance from the Run Condition Table [50].

The event-by-event analysis starts with the track reconstruction, and the calculation of the emission angle of the Cherenkov photons. The cluster charge distributions of the

| Period | Interval day/month/year | Collision | $\sqrt{s_{NN}}$ TeV | $A_{th}$ ADC $\times 10^3$ | Tracks |
|---|---|---|---|---|---|
| 10b | 1/04/2010 - 26/04/2010 | p-p | 7 | 4 | 377 |
| **10c** | **2/05/2010 - 27/05/2010** | **pp** | **7** | **4** | **2,941** |
| **11a** | **25/03/2011 - 28/03/2011** | **pp** | **7** | **3** | **2,150** |
| 11c | 5/06/2011 - 11/06/2011 | p-p | 7 | 3 | 386 |
| 11d | 13/07/2011 - 24/08/2011 | p-p | 7 | 3 | 952 |
| 11e | 23/09/2011 - 4/10/2011 | p-p | 7 | 4 | 186 |
| **12a** | **5/04/2012 - 9/04/2012** | **pp** | **7** | **4** | **177** |
| **12b** | **11/04/2012 - 19/04/2012** | **pp** | **7** | **4** | **222** |
| 12c | 1/05/2012 - 22/05/2012 | p-p | 7 | 4 | 139 |
| 12d | 2/07/2012 - 7/08/2012 | p-p | 7 | 4 | 104 |
| 12f | 15/08/2012 - 10/09/2012 | p-p | 7 | 4 | 102 |
| 12g | 15/09/2012 - 17/09/2012 | p-p | 7 | 4 | 22 |
| **13b** | **20/01/2013 - 22/01/2013** | **p-Pb** | **5.02** | **4** | **3,512** |
| 13c | 22/01/2013 - 25/01/2013 | p-Pb | 5.02 | 4 | 1,051 |
| 13d | 25/01/2013 - 27/01/2013 | p-Pb | 5.02 | 4 | 1,056 |
| 13e | 28/01/2013 - 1/02/2013 | p-Pb | 5.02 | 4 | 1,141 |
| 13f | 2/02/2013 - 10/02/2013 | p-Pb | 5.02 | 4 | 2,337 |

Table 1: The main parameters of the analysed data sets: the name of the LHC period, the time of the data taking period, the type of the collision and its energy, the common threshold of the FEEs, and the number of the reconstructed tracks. The periods highlighted with bold fonts were used for the ageing study as well.

photoelectrons and the MIPs, as well as the $N_{PE}$ vs. Cherenkov angle are filled within the event cycle. Thereafter, the gas gain, and the average number of photoelectrons at the maximum emission angle are calculated.

For the Cherenkov angle reconstruction, a geometrical backtracking algorithm is applied. It was developed by the HMPID Collaboration [38, 51]. This backtracking algorithm is based on the determination of the positions of the MIP and the PE clusters, respectively. In the first step, the so-called global tracks are reconstructed by ITS and TPC, then they are extrapolated to the PCs to determine precisely the position of the MIPs. In the next step, starting from the centroid of each MIP cluster, the emission angle of Cherenkov photons are reconstructed, which belong to the global tracks. The backtracking algorithm applies the following assumptions: PE clusters have the same energy of 6.85 eV and they can be found at the same angle [37]. After the reconstruction of the tracks, the standard track selection cuts were applied to select the global tracks. These cuts are as the follows.

- Track-vertex distance of the closest approach, $DCA_{track-vertex} \leq 2$ cm.
- Track re-fitted in ITS: ITS refit $\neq 0$.
- Track re-fitted in TPC: TPC refit $\neq 0$.
- A reconstructed track has at least 70 clusters in TPC: $N_{TPCraws} \geq 70$ (out of 159).
- To separate the charge contributions originated from MIPs and PE clusters, the selected MIP charge is greater than 120 ADC counts: $Q_{MIP} > 120$ ADC.
- The selected single PE cluster size is less than 4: $PE_{cluster\ size} < 4$.
- The HMPID acceptance ($A$) for Cherenkov photons is $A \geq 0.99$.

After the track selection, the cluster charge distributions originated from PEs and MIPs, as well as the number of PEs per Cherenkov ring were determined.

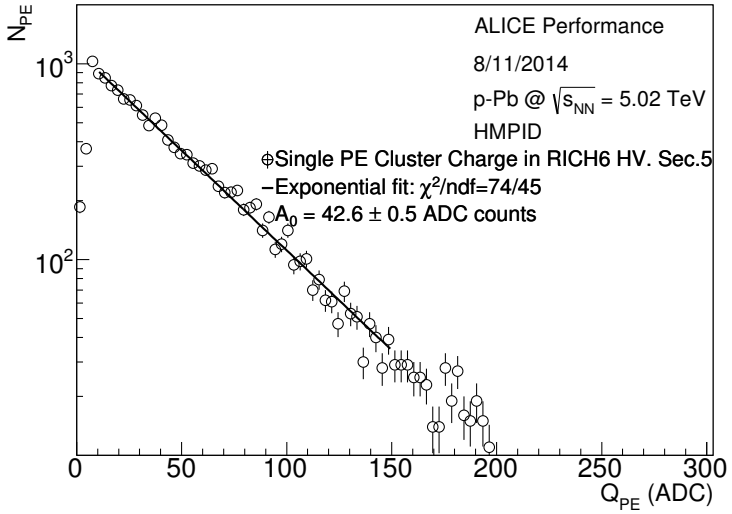


Figure 22: An example of a PE cluster charge distribution extracted from data collected in p-Pb collisions at $\sqrt{s_{NN}} = 5.02$ TeV with a well fitted exponential function [OL06].

The gas gain monitoring is an effective procedure to detect the failed HV sectors and the radiator leaks. The gas gain was extracted from single PE cluster charge distributions in each HV sector. Each single PE cluster charge distribution was fitted with exponential functions in the charge range 10 ADC - 150 ADC counts. The corresponding gas gain, called $A_0$ parameter, was the inverse of the slope of the fitted exponential function. Figure 22 shows the measured PE cluster charge distribution in RICH 6 HV sector 5 with a well fitted exponential function, and with the extracted gas gain of 42.6 $\pm$ 0.5 ADC counts

(45,156±530 electrons) [OL06]. The single PE detection efficiency was calculated from the gas gain by Eq. (14), and it was found to be $\varepsilon_{det}$ = 88.6±1 % for this HV sector. The number of PEs per Cherenkov ring was corrected with the single PE detection efficiencies account for the photon detection stability of the HMPID.

The MIP detection performance was monitored with the most probable value and sigma parameters of the measured MIP cluster charge distributions. The parameters were extracted by a Landau fit in each HV sector. Figure 23 shows an example of a MIP cluster charge distribution fitted with the Landau function in the range 250 ADC - 1,200 ADC counts. The most probable value (MPV) and the sigma parameter were found to be MPV = 401.1±2.1 ADC counts and Sigma = 98.5±1.1 ADC counts, respectively [OL06].

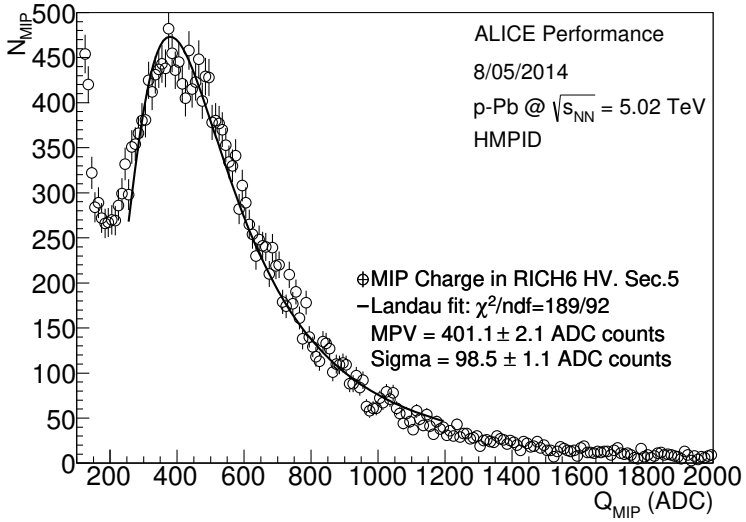


Figure 23: An example of a MIP charge distribution extracted from data collected in p-Pb collisions at $\sqrt{s_{NN}}$ = 5.02 TeV and fitted with a Landau function [OL06].

To determine and monitor the stability of the PE detection performance, the average number of PE clusters per ring as a function of the $\sin^2$ of the Cherenkov angle was calculated in each photocathode. The stability is related to the figure of merit, i. e the QE of the CsI covered PCs. QE was extracted via the comparison of the number of Monte Carlo simulation generated PE clusters to the measured values in each $\sin^2$ bin. Figure 24 shows the average number of the reconstructed PE clusters per ring as the function of the $\sin^2$ of the Cherenkov angle in RICH 2 module. One can expect from Eq. (15) that, the number of PEs is linearly proportional to the $\sin^2$ of the emission angle of Cherenkov

radiation. The detector noise forms small clusters, which contribute to the average number of PEs mostly at small photon emission angles. This fact motivated the extraction of the average number of PE clusters at the maximum emission angle. Note that the average number of PE clusters were corrected with the single photoelectron detection efficiencies in each $\sin^2(\theta_C)$ bin.

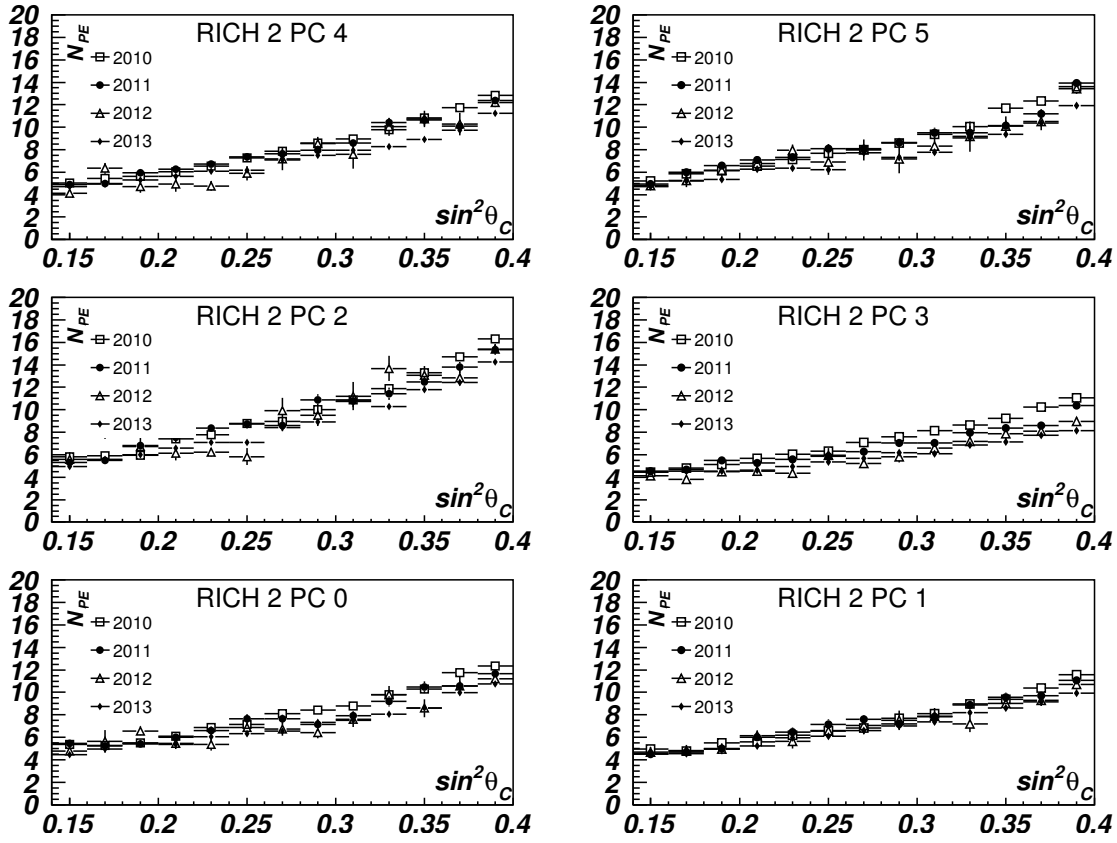


Figure 24: The average number of PE clusters per Cherenkov ring vs. the $\sin^2$ of Cherenkov angle, $\theta_C$ in the RICH 2 module measured during the LHC Run 1 period [OL06].

## 3.4 Description of the simulation method

The present section describes the details of the Monte Carlo simulation applied to extract the quantum efficiencies of the CsI PCs. I used the ALICE Simulation Framework to generate events, and to simulate their passage through the detector system [48]. I generated 40,000 charged hadrons ($\pi^+, \pi^-, K^+, K^-, p$ and $\bar{p}$) with AliGenCoctail setup, which combines the PYTHIA6 [52] and the HIJING [53] generated events.

The ALICE Reconstruction Framework was applied to reconstruct the generated events. First of all, the local cluster reconstruction was performed in each subdetector. Then, the vertices and the tracks were reconstructed in parallel and the particles were identified. Finally, the lists of reconstructed particles and the global event properties were filled into an Event Summary Data. From the ESD outputs, the PE cluster charge distributions, the corresponding gas gain values, and the number of PE clusters per ring vs. $\sin^2(\theta_C)$ were extracted for each PC.

The interactions of the ALICE subdetectors with the generated particles were already implemented in the GEANT3.21 simulation code. The HMPID detector with its geometry, the constituent materials and their optical properties were also included in the ALICE Simulation Framework by the HMPID Collaboration [54, 55]. The loss of Cherenkov photons on the CsI surface by Fresnel-reflection process was also added to this simulation, as a correction.

As presented in Eq. (15) and Eq. (16), the number of PEs per Cherenkov ring depends on the measured radiator transparency, the quantum efficiency, and the photoelectron detection efficiency calculated from the measured gas gain. The measured radiator transparency and the calculated gas gain were implemented in the simulation. The third input of the simulation was the QE vs. energy function. The output of the simulation was the number of PEs. If the simulated number of PEs vs. $\sin^2(\theta_C)$ were in agreement with the measured one, the QE in the simulation was also in agreement on average with the QE of the investigated PC. This procedure was performed for each PC for the 10c, 11a, 12ab and 13b LHC periods. The simulation parameters are described in the following items:

(i) **Absorption of Cherenkov photons in the liquid radiator:** The absorption length, $L_{abs}(E_{Ph})$ of the emitted Cherenkov photons were included in the simulation. These were calculated from the measured transparencies, $T(E_{Ph})$ within the energy range from 5.5 eV to 8.5 eV for both of stagnant and circulation detector operation modes using Eq. (11). Figure 25 shows the measured transparencies as a function of photon wavelength (*upper panels*), and the corresponding absorption lengths as a function of photon energy (*lower panels*) for one period from each year of the Run 1. As expected, the UV transparency threshold of $C_6F_{14}$ was around 165 nm, and the transparency increased with the photon wavelength [37]. The radiator transparency were not measured for each LHC period. In case of 11a and 12ab periods, those transparencies were used ins the simulation, which were measured close to those periods.

In case of 10c and 13b periods, transparency measurements were not performed, thus the average of the five transparencies was used in the simulation.

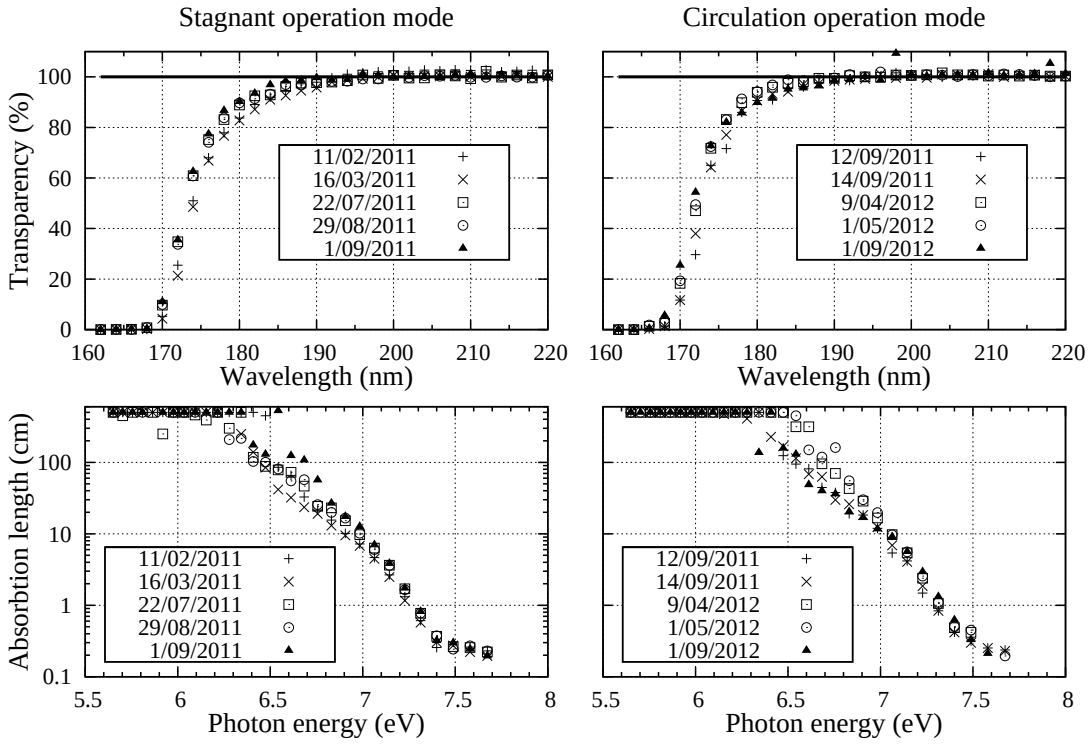


Figure 25: The measured radiator transparencies (*upper*) and the calculated absorption lengths (*lower*) at different photon energies for both of stagnant (*left*) and circulation (*right*) operation modes.

(ii) **Conversion of Cherenkov photons to PEs in the CsI covered PC:** To calculate the quantum efficiency of the CsI surface, I used the following $QE(E_{Ph})$ quantum efficiency function:

$$QE(E_{Ph}) = C \cdot \left[1 - e^{-1.29730 \cdot (E_{Ph} - 6.07267\, eV)}\right] \quad , \tag{17}$$

where $E_{Ph}$ is the photon energy in eV units, $C$ is a constant scale parameter with the typical value in the range 0.2-0.4. This input function was modified to reproduce the number of measured PE clusters. The parametrisation of this input function is based on the earlier measurements published in Ref. [56].

(iii) **Determination of input gas gain parameter:** This is also performed with this simulation before the extraction of $QE(E_{Ph})$. The measured PE cluster charge distribution, and the measured gas gains were reproduced.

The absorption of Cherenkov photons, and the creation of PE clusters were implemented to the simulation from the measured data. Therefore, the quantum efficiency vs. photon energy function remained as an adjustable input parameter. The number of PE clusters were determined by the same analysis method applied in the LHC data, and described in Sec. 3.3. If the number of the generated Cherenkov photons was in agreement with the measured value within statistical errors, than the adjustable input parameter of the simulation was also in agreement with the real average quantum efficiency.

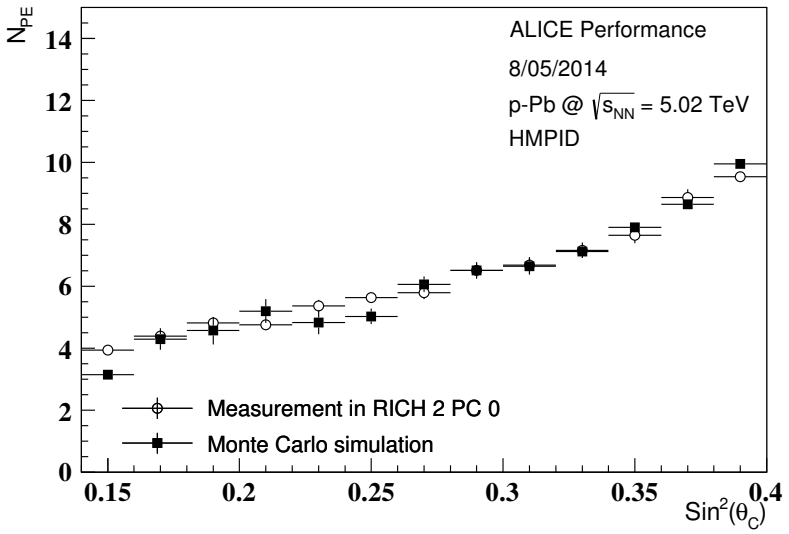


Figure 26: The number of PE clusters, $N_{PE}$ per Cherenkov ring vs. the $\sin^2$ of Cherenkov angle, $\theta_C$ in RICH 2 PC 0 which was extracted from the LHC data (*empty circles*) and the simulation (*filled rectangles*) [OL07].

Figure 26 shows an example of the comparison between the Monte Carlo generated and the measured data. The number of PE clusters extracted from p-Pb data (*empty circles*) in RICH 2 PC 0 and the generated one (*filled rectangles*) are plotted as a function of $\sin^2$ of the $\theta_C$ Cherenkov angle. The simulation and the measurement were in good agreement.

## 3.5 Results on performance and ageing of ALICE HMPID

In this section, I present the results on the performance and the ageing of the HMPID detector extracted from LHC data sets collected during Run 1 period.

Figure 27 shows the period-by-period evolution of the extracted gas gains with the corresponding statistical errors in each HV sector. Note that the horizontal scale is not

linear in time, it shows the LHC periods listed in Tab. 1. The single photoelectron detection efficiencies were calculated by Eq. (14). In each HV sector, these vary in the efficiency range 88 % to 94 %, which corresponds to the design performance of the HMPID detector [OL06].

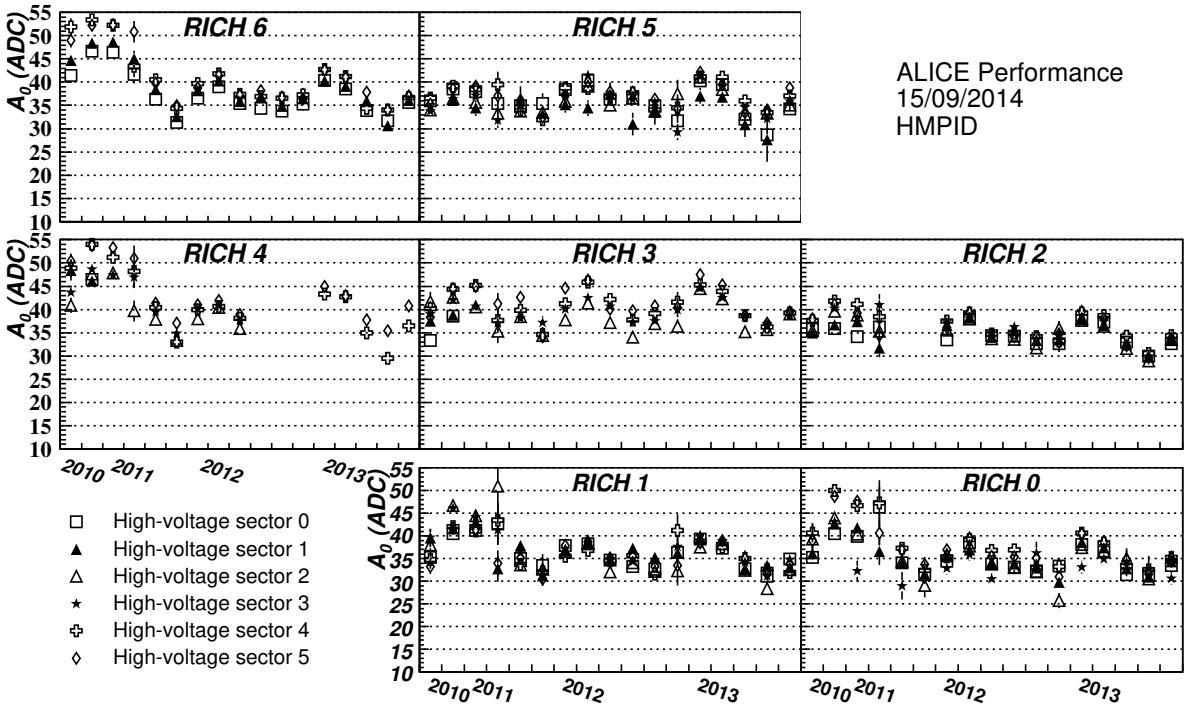


Figure 27: The variation of gas gain ($A_0$) with the corresponding statistical errors for each HV sector during LHC Run 1 period [OL06].

Figure 28 shows the period-by-period evolution of the most probable values and of the sigma parameters of the MIP cluster charge distributions with the corresponding statistical errors in each HV sector [OL06]. The upper points around 400 ADC value correspond to the MPV parameters and the lower points around 100 ADC value correspond to the sigma parameters, respectively. The missing points correspond to those runs in which there were no sufficient statistics after the application of the track selection cuts. It is worth noticing that, the significant decrease in the gas gain after the fourth LHC period is not a detector effect, it is the result of gas gain equalisation performed after the LHC11c period to achieve more homogeneous detector conditions. For this purpose, a high voltage scan was performed from 1,900 V up to 2,050 V. To equalise the gas gains close to $4\times10^4$ in each HV sector, the high voltages were set to different values between 2,025 V and 2,055 V in each sector.

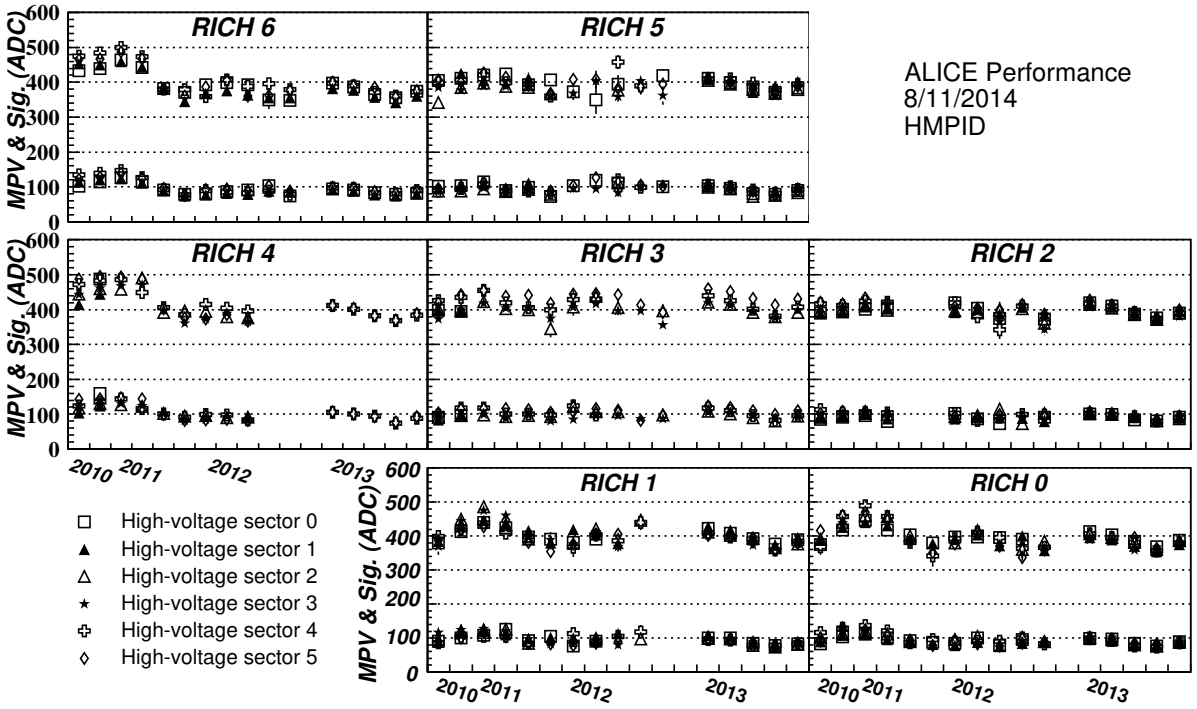


Figure 28: The variation of most probable value (*upper points*) and the sigma (*lower points*) of the MIP charge distribution with the corresponding statistical errors for each HV sector during LHC Run 1 period [OL06].

Figure 29 shows the gas gain values extracted from PE cluster charge distribution with the corresponding statistical errors. The selected LHC runs were performed before (*empty circles*) and after (*filled circles*) the gain equalisation. A better HV sector uniformity was achieved after the gain equalisation [OL06].

Note that fluctuations are larger than their statistical errors in the variation of the single electron mean pulse height, as well as in the most probable value and in the sigma parameter of the MIP cluster charge distributions. This was observed due to the lack of the online correction for the pressure and the temperature, which were measured in the RICH modules. The $A_0$, MPV, and sigma parameters varied within $\pm 15\,\%$. The above presented results show that the MWPC operated reliably the LHC Run 1 period. A significant decrease was not observed in the performance of PE and the MIP detection, those corresponded to the performance measured immediately after the design of the HMPID detector [OL06].

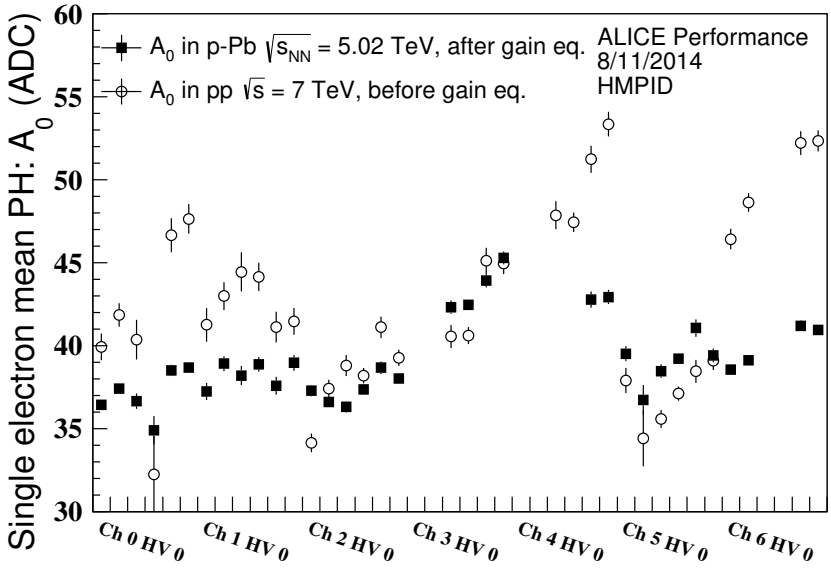


Figure 29: The gas gain is plotted for each HV sector before the gain equalisation (*empty circles*) and after the gain equalisation (*filled rectangles*) [OL06].

To quantify the PE detection stability, the average number of PE clusters per Cherenkov ring was calculated at the maximum emission angle, in the bin $0.38 < \sin^2(\theta_C) < 0.4$. This Cherenkov angle range was chosen, because here the number of PE clusters was less influenced by the larger background measured in p-Pb, in contrast to the bins at smaller angles.

Figure 30 shows the variation of the average number of PE clusters per Cherenkov ring at the maximum emission in each PC during the LHC Run 1 [OL06]. The extracted PE numbers were corrected with single PE detection efficiencies. The values are omitted for PCs with leaked radiator trays. The numbers of PE clusters in different PCs show variation among each other because of the failed HV sectors. The average number of PE clusters per ring at maximum emission angle was stable in all of the individual PCs, except in the PCs of RICH 2 where 15-36 % reduction was observed during the period of 2010-2013. This result is discussed and concluded together with result observed on the quantum efficiency.

To quantify the variation of quantum efficiencies of the CsI PCs, the QE vs. photon energy functions were evaluated at the energy of 7.3 eV (wavelenght of 170 nm). The QE of the PCs were measured and evaluated at this wavelength after their production time.

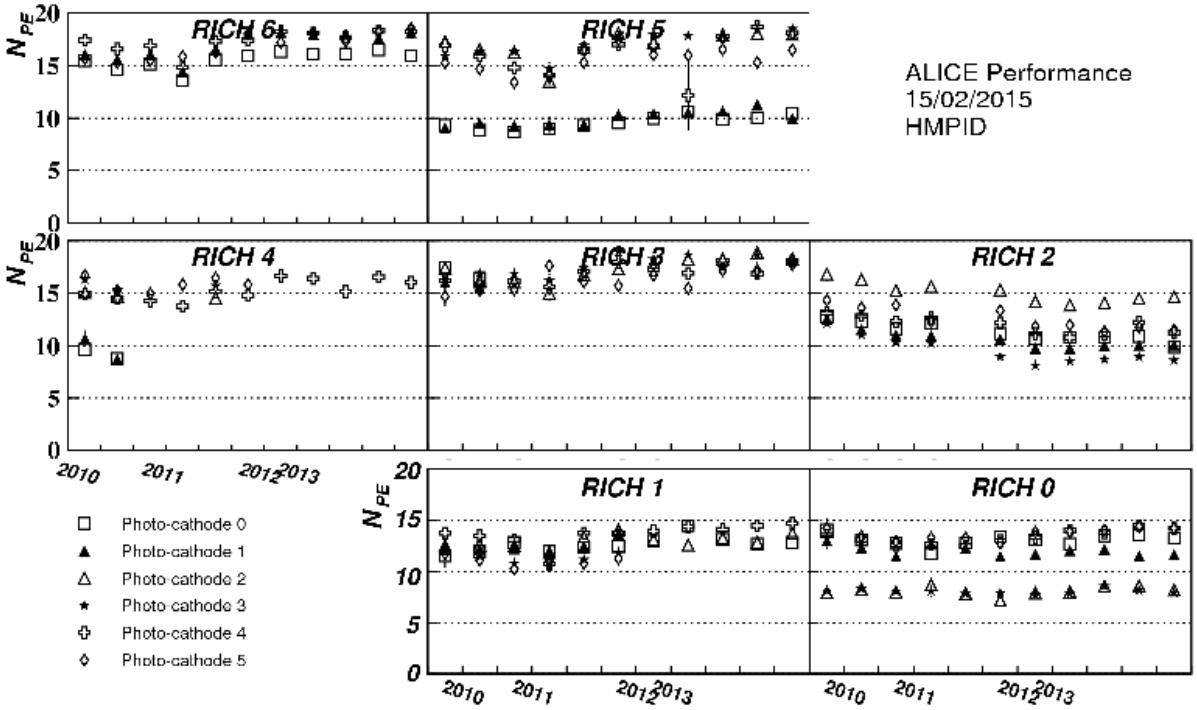


Figure 30: The variation of the average number of the reconstructed PE clusters per Cherenkov ring at the maximum emission angle in p-p and p-Pb collisions during the period of 2010-2013 [OL06]. The PE numbers were corrected with single PE detection efficiencies and the corresponding statistical errors are plotted as well.

In Fig. 31, the quantum efficiencies of the PCs are plotted as a function of the production date of the PCs. The QEs were stable in each photocathode, except in the PCs of RICH 2, where a significant, 30 - 40 % QE loss were observed. The relative systematic errors of the simulated QEs were determined by the comparison the results produced using the extreme data sets. The value of the relative systematic error caused by the measured radiator transparencies was found to be 15 %. The relative systematic error caused by the gas gain was found to be less than 1 %. To conclude, the systematic error caused by the measured radiator transparency is not yet low enough (few percent) to predict reliably the ageing of the CsI PCs using only the Monte Carlo simulations. Further radiator transparency measurements will be performed by the HMPID group to provide more reliable input data for the Monte Carlo simulation.

The possible causes of the observed loss in the number of PEs and quantum efficiency of PCs of RICH 2 are discussed in the following points.

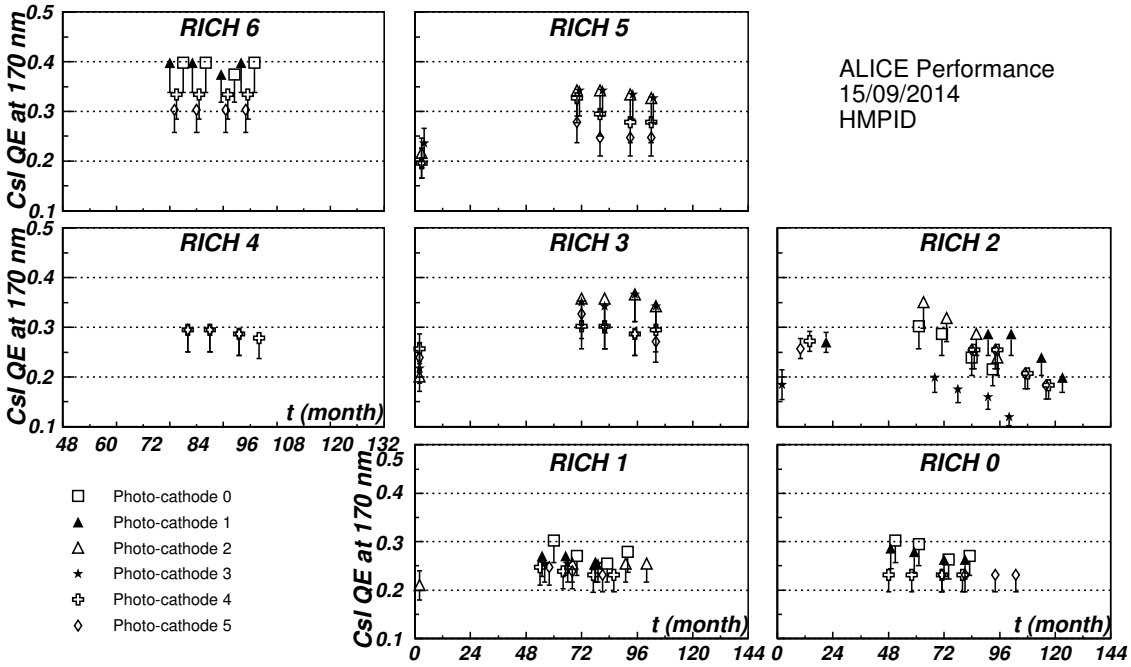


Figure 31: The quantum efficiency at the photon wavelength of 170 nm as a function of production date for the PCs. The relative systematic error of 15 % is also plotted.

(i) **Exposure to humidity:** Figure 32 shows the variation of water and oxygen contamination of RICH modules during the LHC periods which are used for study of QE. The oxygen and water contamination were normal during the Run 1 and there were no difference between RICH 2 and the other modules in this respect. Based on these results, one can conclude that quantum efficiency loss is not caused by the water or oxygen contamination in RICH 2.

(ii) **Age of photocathodes:** In the RICH 2 module, PC 1, PC 4, and PC 5 were produced between 2001 and 2002 [56]. As shown in Fig.31, these PCs are the oldest ones. The extracted quantum efficiencies of this module are in agreement within errors between the measurements, which were performed in 2004 [56] and in the 10c period, at the beginning of the LHC Run 1. PC 0, PC 2, and PC 3 were produced between 2004 and 2005. In case of PC 0, PC 2, and PC 3, one observes a significant, 15-36 % loss of quantum efficiency. From these facts, I concluded that there is no correlation between the date of production and the measured quantum efficiencies in case of RICH 2 module.

(iii) **Ageing due to ion bombardment:** To monitor the accumulated charge dose, integrated currents were measured on the anode wires with the nA-meters of the HV boards by the HMPID group [OL06, 57]. The results of these measurements provide an average value of accumulated charge dose per PC of $0.013\,\mathrm{mC/cm^2}$, well below the threshold of $0.2\,\mathrm{mC/cm^2}$, which is the value to observe any possible ageing effects [58]. This charge threshold will not even be reached before the end of Run 3 period, when the accumulated charge dose is expected to reach $0.16\,\mathrm{mC/cm^2}$.

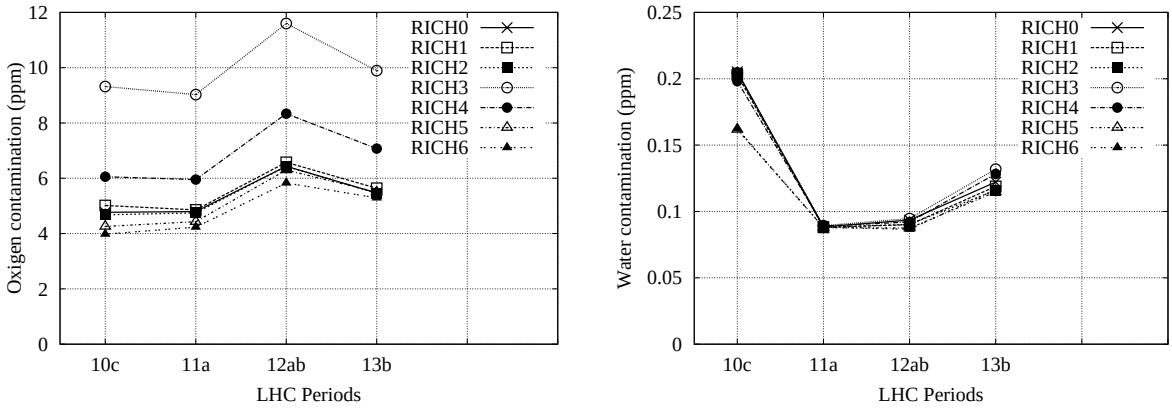


Figure 32: The variation of the average oxygen (*left panel*) and water (*right panel*) contamination in each RICH module for different data taking periods during the LHC Run 1 [OL06].

To conclude, the measured number of PEs and the extracted QEs were stable during LHC Run 1 period (2010-2013), as well as were consistent with the measurements of the humidity and of the accumulated charge dose in each PC, except in the six PCs of the RICH 2 module. Further data collection during LHC Run 2 and new radiator transparency measurements are necessary to fully understand the observed effects in the RICH 2 module.

## 3.6 Summary on the performance and the ageing of the ALICE HMPID

I presented a study focused on the variation of the performance and the ageing of the ALICE HMPID detector. I determined the photoelectron production and detection performances by the analysis of the LHC p-p and p-Pb data sets collected during the LHC Run 1 period (2010-2013).

The single PE detection efficiencies were found to be above 88 %, and were in agreement with the performances measured immediately after the production date of the PCs. The average number of the detected PE clusters per Cherenkov ring at the maximum emission angle was stable in each PC, except in the PCs of RICH 2, where 15-36 % reduction was observed. I quantified the QE of the CsI covered PCs with Monte Carlo simulation. The decrease of quantum efficiencies were not observed in the PCs, except in the PCs of RICH 2, where a significant, 30-40 % decrease were found. However, the observed effects were not concluded as the ageing of the CsI PCs of the RICH 2 module due the their large systematic uncertainties caused by the radiator transparency. The results observed in the other RICH modules were consistent with the results of the humidity and the charge dose measurements in each module; and did not present any ageing effect. These results show that the HMPID detector can operate reliably until the end of the first high-luminosity LHC period (2023).

I published the results in an ALICE Public Note together with the HMPID group [OL06]. I presented my results on behalf of the ALICE Collaboration at Quark Matter 2014 conference [OL07].

# 4 Review of muon radiography

The following chapters focus on the application of gaseous detectors for cosmic muon imaging. This chapter presents the possible applications and the technical details of muon radiography.

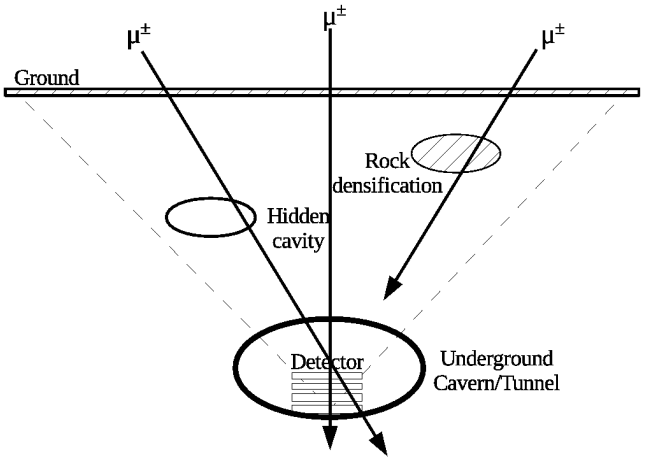


Figure 33: Geometrical arrangement of underground muography: a tracking detector is deployed inside an underground cavern or tunnel and measures the flux of cosmic muons. The presence of an underground cavity (rock densification) above the detector causes an increase (decrease) in the muon flux relatively to the expected value.

The first muon radiographic measurements were proposed by E. P. George at the beginning of the 1950s [59]. The aim of the measurements was to determine the rock density above an Australian mine by the measurement of the cosmic muon flux. Geiger counters were deployed in an underground tunnel inside the mine. The idea was that the rock densifications, e. g. the ores or the minerals cause smaller muon flux than the expected flux calculated from the soil thickness and the estimated average density. In case of cavities, the measured muon flux is larger than the expected flux due to the missing material. Figure 33 shows the scheme of underground muography. E. P. George could determine the significant differences in soil thickness at different directions. However, the applied detector was not reliable and precise enough to find ores above the location of the measurement.

In the following subsection, I review the milestones of cosmic-ray muon imaging, and the progress of recent applications.

## 4.1 Applications of cosmic muon tracking

### 4.1.1 Subsurface density mapping and underground cavity research

In the 1960s, the main properties of cosmic rays were sufficiently known and the particle detection techniques were precise enough to perform reliable measurements. Based on the idea of E. P. George, muography measurements were proposed by L. W. Alvarez *et al.* with the aim to find hidden crypts or chambers inside the Chephren pyramid [16]. A tracking detector was installed into the Belzoni chamber under the Chephren pyramid and the measurements were started in early 1968.

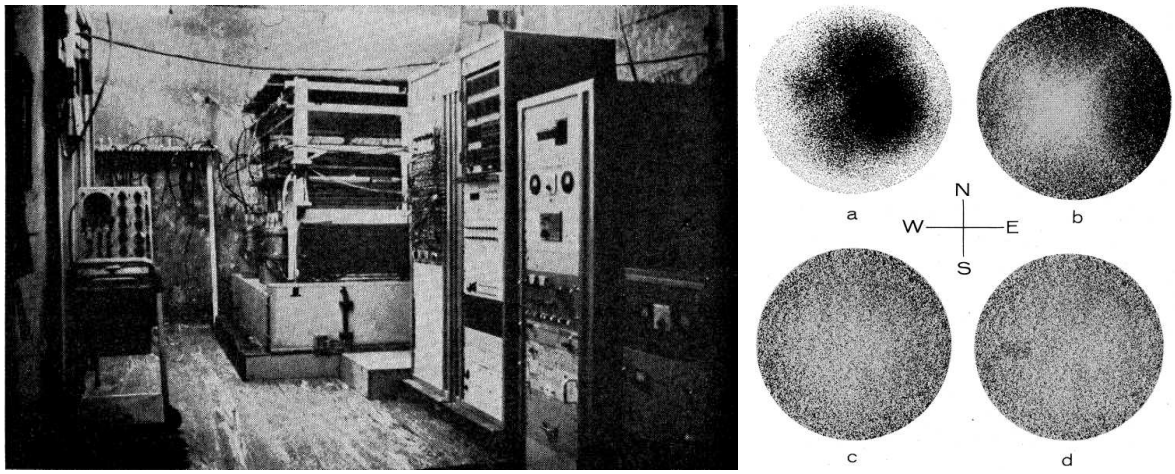


Figure 34: *Left:* A muon detector consisting of spark chambers, scintillators, absorbers and data readout modules was installed inside the Belzoni chamber under the Chepren pyramid [16]. *Right:* The measured scatter plots without any correction ($a$), with correction for detector acceptance ($b$), and with correction on the surface inhomogeneities of the pyramid ($c$), and the result of the Monte Carlo simulation with the Kings' chamber ($d$) [16].

The *left panel* of Fig. 34 shows the cosmic ray detector inside the Belzoni chamber. It was constructed from two spark chambers with the sensitive area of 1.8 m $\times$ 1.8 m, placed parallel under each other with the distance of 0.3 m, and from three scintillators, one above the spark chambers and 2 below them. Furthermore, a 1.2 m thick iron absorber was placed between the lower two scintillators to absorb low energy particles which would obscure the the "image" of the pyramid. Both the spark chambers and the scintillators

were modular because of transportation requirements. The modular design necessitated corrections on detector acceptance. The detector angle of view was a cone with the opening angle of 70° which allows to explore 19% of the volume of the pyramid. The data were recorded on a magnetic tape in a laboratory which was built a few hundred meters away from the Chephren pyramid.

During the measurement, more than 1 million muons were detected inside the Belzoni chamber under limestone with average thickness of about 100 meters. The pyramid corners were located and the detector position was determined with the precision of 1 meter already in the September of 1968. The analysis of the complete data set took 2 months.

In addition, a Monte Carlo simulation of the measurement was also performed. It took into account the pyramid shape and the detector effects. A hypothetical chamber was also implemented in the simulation and 700,000 muon tracks were generated. The *right panel* of Fig. 34 shows the ratio of the observed data to the expected data in 0.15° by 0.15° angular bins without any correction ($a$), with correction only on detector acceptance ($b$), with correction on the outer shape of the pyramid ($c$), and with the simulation of a possible chamber, called King's chamber which is filled with a material with the density of two times than the average density of the pyramid (see the darker region in $d$). From these results they could conclude that there is no hidden chamber inside the explored volume of the Chephren pyramid.

Pioneering measurements were also performed in an underground cavern near Trieste in Italy in the middle of 1990s by E. Caffau *et al* [17]. They applied a tracking system built from four glass spark chambers with the sensitive area of 1 $m^2$. The detector was installed inside the Grotta Gigante cave. The measurements were performed at three different positions at the depth of about 115 m. The high voltage power supplies and the trigger electronics were placed in a Nuclear Instruments Module (NIM) crate, and the complete data acquisition system was housed in a portable Computer Automated Measurement and Control (CAMAC) crate. The gas bottles were deployed at the entrance of the cave. The installation of the measurement inside the cave took about 1 day.

Digital models were made about the terrain above the measurement site and about the vault of the cavern. These models were used to calculate the expected muon flux. The modelled and the measured fluxes were in good agreement. Underground cavities were not found above the detector.

The experiments presented above, demonstrated that muon radiography is a promising technique for underground cavity research and for subsurface density mapping. However, the application oriented development of particle detectors is necessary to utilise the potential of this method.

### 4.1.2 Imaging of volcanic activity by tracking of nearly horizontal muons

The Mt. Asama was the first volcano which was imaged with muography in 2006 [18, 60]. After the eruption ($1^{st}$ of September in 2004), the Mt. Asama could not be accessed, and the conventional geophysical methods, such as electromagnetic and seismic techniques could not be performed. H. Tanaka *et al.* deployed Emulsion Cloud Chambers (ECC) with the detection area of 0.4 $m^2$ inside a 1 meter deep vault at the distance of 1 km from the summit crater of Mt. Asama, as shown in the *panel A* of Fig. 35. The angular resolution of the ECC detector pair was 10 mrad, thus the image resolution was 10 meter from the distance of 1 km. The data analysis was performed after the measurements: emulsion films were digitised and read out through a microscope and tracks were reconstructed by an image processor. More details about the readout of ECCs are provided in Sec. 4.5.

The density distribution of the summit crater was extracted by GEANT4 simulation [61]. A topographic map of Mt. Asama was included in the simulation. Muons were generated and were started from the detector with the energy above 1 GeV and with randomised zenith angle. The muons were tracked across the volcano and the flux was calculated behind the it. The average densities along the paths of the muons were modified and extracted when the simulated flux reproduced the measured one. *Panel B* of Fig. 35 shows the extracted density distribution of the summit crater. This is the first image about a crater of an active volcano done with muography. The higher density region plotted with red colour on *panel B* of Fig. 35 corresponds to the andesite lava mound formed after the eruption. The precision of the topographic measurement was about 2 %, which caused a systematic error of 3.2 % for the extracted density values. At the shallow crater region, Tanaka *et al.* could achieve better position resolution with muography than could have been achieved with conventional techniques. Furthermore, muography could image the lower part of the volcano which was not accessible to the conventional methods. The limit of conventional methods, such us high-resolution radar, is plotted by *dashed line* in *panel B* of Fig. 35.

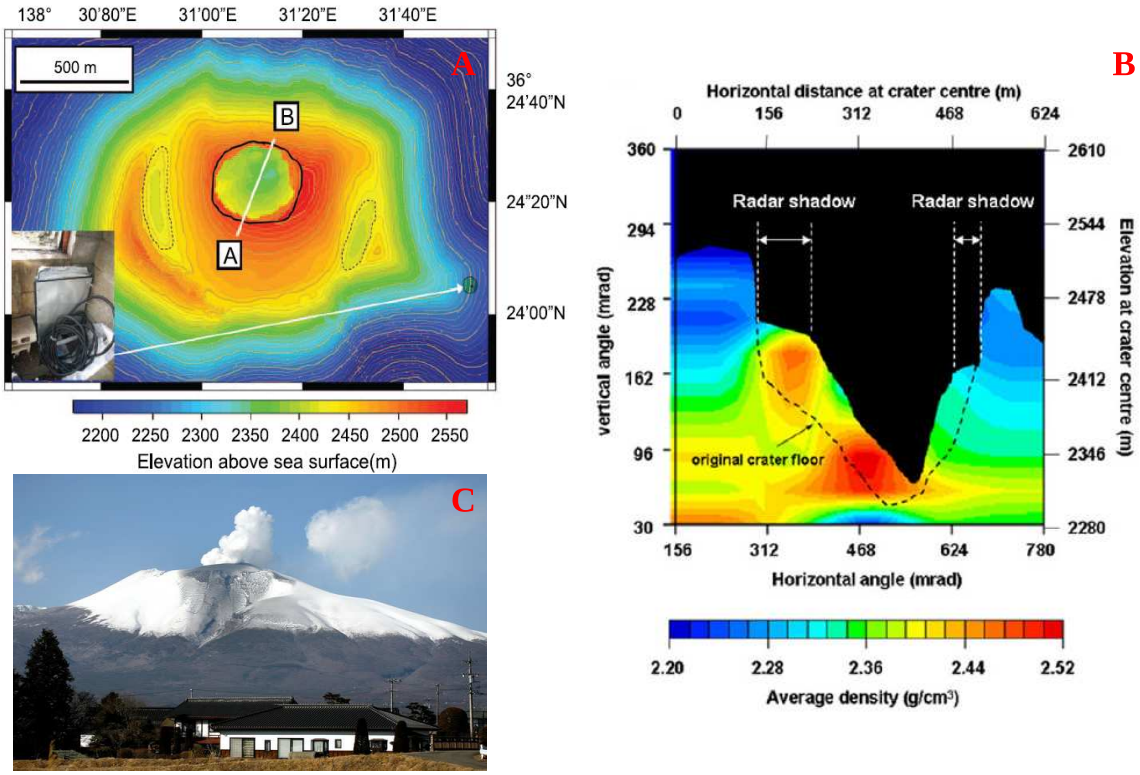


Figure 35: **A:** the map of the Asama volcano shows the location of the emulsion cloud chamber with an arrow, the white line shows the plane of the density distribution plotted in panel **B**. The *solid black line* shows the summit crater [18, 60]. **B:** the first muographic image about a volcano, the reconstructed average density distribution of the summit crater shows the solidified magma (*red region*) at the crater floor [18, 60]. **C:** a photo about the eruption of the Asama volcano on the 2$^{\text{nd}}$ of February in 2009 [62].

*Panel C* of Fig. 35 shows the eruption of Asama in 2009. In spite of the encouraging results, the ECC detectors are not applicable to perform real-time measurements of the density distribution of volcanoes, because the data processing is not possible during data taking. The real-time measurement of the lava movement inside the volcano is essential to predict the future eruptions.

The next pioneering experiment was performed during an eruption period of the Satsuma-Iwojima volcano from the 14$^{\text{th}}$ of June until the 10$^{\text{th}}$ of July in 2013. Tanaka *et al.* developed a scintillator-based tracking system, and applied it to the real-time measurement of the eruptions [63]. The tracking system consisted of six scintillator detectors with the

size of 2 $m^2$ and with the position resolution of 10 cm. The tracking system was deployed at the distance of 1.4 km from the summit crater. The distance between the first and last tracking layers was 3 m. That distance and the position resolution provided an angular resolution of 33 mrad for the tracking system. With this angular resolution, the density distribution of the summit crater could be determined with the resolution of $46 \times 46$ $m^2$. Five lead absorbers with the thickness of 10 cm (density-length of 111 $g/cm^2$) per layer were installed between the scintillators to absorb those particles which could not penetrate the volcano but had enough energy to penetrate the scintillators, such as the soft component of cosmic rays and the low-energy muons. I will call these particles the "physical background noise" for the remaining part of the thesis. The flux of physical background noise was less than 10 $m^{-2}$ $sr^{-1}$ $day^{-1}$ and the time resolution of the visualisation was drastically improved. The thickness of the volcano was 800 m with empty crater and its average density was 2 $g/cm^3$. The measured muon rate was 1.75 $day^{-1}$ in each angular bin from the directions between 247 mrad and 281 mrad. With filled crater, the effective thickness increased to 1,200 m, thus the rate reduced to 0.37 muons per day. Tanaka *et al.* could resolve the difference between an empty and a filled crater with $2\,\sigma$ (95 %) confidence level with 3 days of data taking.

The density distribution was extracted for each angular bin from the measured flux. The measured flux was in good agreement with the expected one calculated by Monte Carlo simulation. Figure 36 shows the first time sequential muon radiographic animation about the magma dynamics inside an erupting volcano with the $1\,\sigma$ (68 %) confidence level upper limit of the average density plotted along the muon path. During the eruptions, from the $14^{\text{th}}$ to the $16^{\text{th}}$ of June, and from the $29^{\text{th}}$ of June to the $1^{\text{st}}$ of July, the higher dense magma ascended in the crater, as shown in the *upper left* and in the *middle right* panels of Fig. 36. Furthermore, they observed that the flow of the lower density volcanic gases were faster than the magma body. This observation was consistent with the models of volcanology.

To conclude, muon radiography can be a promising method to understand better, or even to predict volcanic eruptions. The optimisation of muon trackers is necessary to reduce the time frame of muographic imaging to about 12 hours. The increase of the detector surface to the order of 10 $m^2$ is required to minimise the time of data taking. Furthermore, a reasonable position resolution ($< 1$ cm) is required for the detector layers to minimise the amount of absorbers needed to suppress the physical background noise.

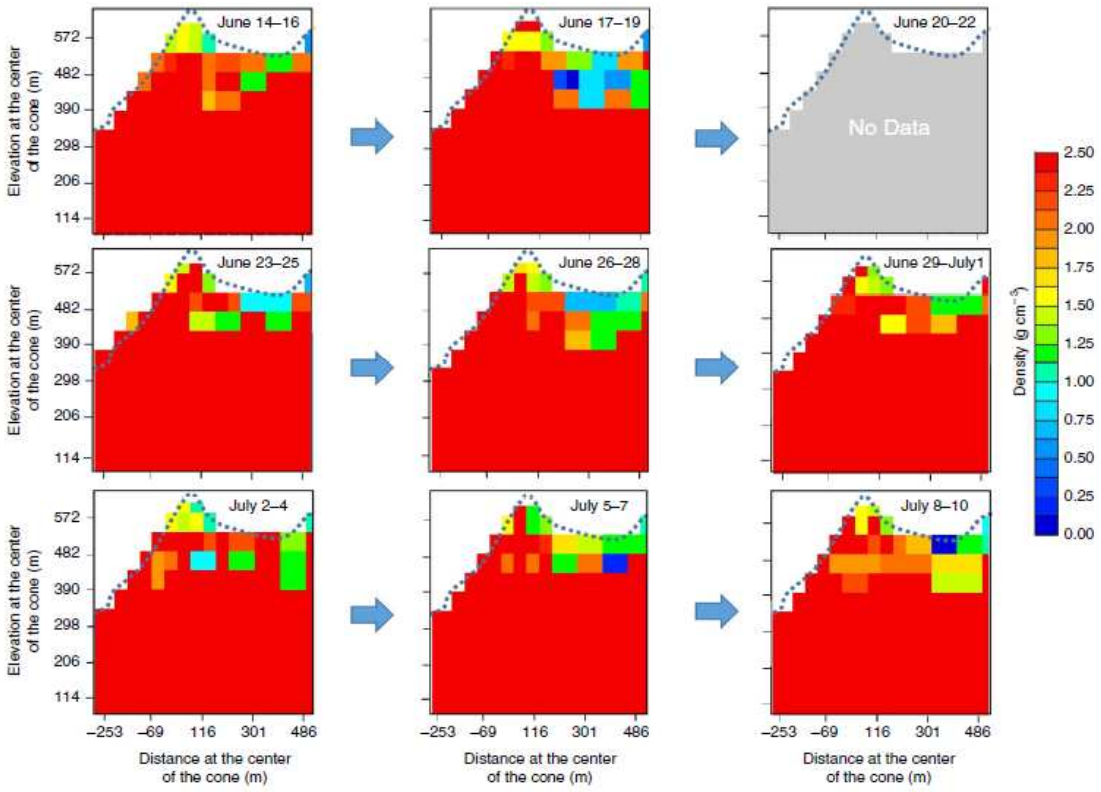


Figure 36: The muographic visualisation of the magma column dynamics in the erupting Satsuma-Iwojima volcano: the measured average density distribution shows that higher density magma column did not ascend fast, while the lower density gaseous region above it was more dynamic before and after the eruptions ($14^{\text{th}}$ and $29^{\text{th}}$ of June) [63].

### 4.1.3 Material discrimination by the measurement of muon scattering

Charged particles scatter with small angle on the nuclei of the transversed material by Coulomb interaction. The distribution of scattering angles is well approximated by a Gaussian distribution with $\theta$ RMS width which is described by the following equation [22]:

$$\theta = \frac{13.6\,\text{MeV}}{p\beta c} Z \sqrt{\frac{L}{X_0}} \left[1 + 0.038 \ln(L/X_0)\right] \quad , \tag{18}$$

where $p$, $\beta c$ are the momentum and velocity of the particle; $Z$, $L$, and $X_0$ are the atomic number, thickness, and radiation length of the transversed material, respectively. Therefore, one can determine the density and the atomic number of the object of interest by the measurement of the scattering angle of those particles which penetrated the object. This imaging concept was proposed by scientists at the Los Alamos National Laboratory [64].

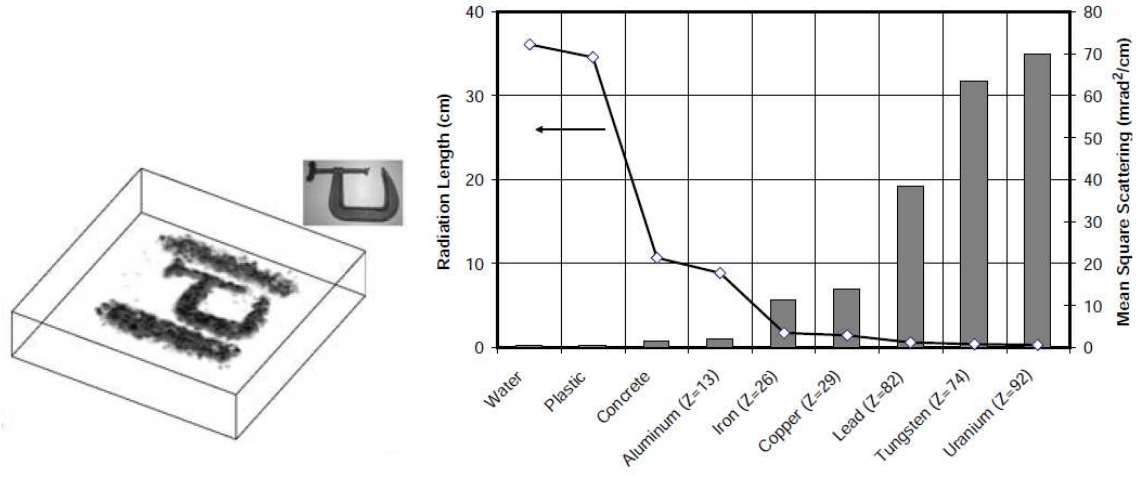


Figure 37: *Left:* An image of a steel C-clamp produced with 10,000 muons detected in about 30 minutes [65]. *Right:* The radiation length, and the mean square scattering per unit length for the muons with the energy of 3 GeV are plotted as a function of atomic number. The high-$Z$ materials can be discriminated from the mid-$Z$ and the low-$Z$ materials by the measurement of the multiple scattering of muons [65].

Based on this concept, different research groups and companies turned to the development of large volume muon trackers and the optimisation of muon tomography [65, 66, 67, 68]. The *left panel* of Fig. 37 shows one of the first experimental demonstrations of muon scattering tomography: an image about a C-clamp which was made by muon tomography [65]. The *right panel* of Fig. 37 shows the calculated radiation length (*linked empty diamonds*) and mean square scattering per unit length (*filled boxes*) for muons with the energy of 3 GeV as a function of the atomic number $Z$ of the material. These results demonstrate that high-$Z$ materials can be discriminated from the surrounding lower density materials with the measurement of multiple scattering of cosmic-ray muons [65].

Furthermore, the applicability of muon scattering tomography for the investigation of the Fukushima Daiichi nuclear power plant was demonstrated by Monte Carlo simulations [69]. The first measurements were performed by K. Morishima *et al.* in 2015 [70]. They observed that the core was melted down inside Reactor No. 2.

Muon scattering tomography is applicable to discriminate high-$Z$ materials from the surrounding low-$Z$ materials. However, the discrimination and identification of low-$Z$ materials are not yet achieved within a reasonable time. The discriminating of low-$Z$ materials require a different novel approach, discussed in Chapter 7.

## 4.2 Principles of muon radiography

After the description of possible applications of muon radiography, present section focuses on the principles of cosmic muon absorption imaging technique.

As presented in Sec. 1, the muonic component is the most abundant in energy at the surface of the Earth due to their relatively long lifetime ($\tau$ =2.2 $\mu s$) and fairly small interaction cross-section. The integrated flux of vertical muons with energy above 1 GeV is approximately 70 $\mathrm{m^{-2}\,s^{-1}\,sr^{-1}}$ at sea level [22]. The energy spectrum of muons originates from the spectrum of pion and kaon parents. The muon spectrum is the convolution of the spectra of parent particles, energy loss, and decay processes. The mean energy of muons is about 4 GeV at sea level. Three energy regions can be distinguished in the spectrum of muons due to the competition of energy dependent processes [71]:

- $E_\mu \leq 1\,\mathrm{GeV}$: The energy loss and decay of muons need to be take into account. The spectrum is almost flat.
- $1\,\mathrm{GeV} \leq E_\mu \leq \epsilon_{\pi,K}$, where $\epsilon_\pi = 115\,\mathrm{GeV}$ and $\epsilon_K = 850\,\mathrm{GeV}$ are the critical energies [2] of pions and of kaons in the vertical direction. Below the energy of 100 GeV, the muon energy loss in the atmosphere is not negligible, especially at near horizontal zenith angles. Above the energy of 100 GeV, the muon spectrum follows well the spectrum of parent mesons.
- $E_\mu \geq \epsilon_{\pi,K}$: The pion and kaon decay probabilities are suppressed due to the increased decay length, $L \sim \gamma\tau c$, where $\gamma$ is the Lorentz factor, $\tau$ is the lifetime of the particles, and $c$ is the speed of light. At this energy range, the flux is higher for inclined muons due to the increased thickness of the atmosphere.

In general, the differential muon flux, $f_\mu(E_\mu, \theta)$ is defined by the following equation [9]:

$$f_\mu(E_\mu, \theta) = \frac{\mathrm{d}N_\mu(E_\mu, \theta)}{\mathrm{d}\Omega\,\mathrm{d}A\,\mathrm{d}t\,\mathrm{d}E_\mu}\ \left[\mathrm{cm^{-2}sr^{-1}s^{-1}GeV^{-1}}\right]\ , \tag{19}$$

where $\mathrm{d}\Omega$ is the differential solid angle, $\mathrm{d}A$ is the surface element in the direction of observation ($\theta$) and $\mathrm{d}t$ is the measurement time.

The most energetic muons with energy above 1 TeV are able to penetrate across even kilometers of rock. The attenuation of muons depends on the amount of matter along the path of muons. Muon radiography relies on this fact. It is based on the measurement of

[2] At the critical energy, the decay probability equals to the hadronic interaction probability.

flux of those muons which penetrated across the body of interest to determine the amount of matter along the path of penetrated muons. The so-called "under open sky" condition where the muons interacted only with the atmosphere before they were detected. Three different approaches are used to determine the muon flux under open sky at a given altitude:

(i) **Measurement:** The trajectory of muons is measured by a tracking system and with the correction on detector geometry and detector effects, such as efficiency, the flux can be determined. More technical details about muon tracking are provided in Sec. 4.5. My work was concentrated on the development of tracking systems for muography. The precise determination of muon flux under open sky is very difficult using tracking detectors due to physical background noise. More details are provided about this issue in Sec. 4.4.

(ii) **Monte Carlo simulation:** The muon spectrum at a given altitude can be calculated by the simulation of muons across the atmosphere. For example, the COsmic Ray SImulations for KAscade (CORSIKA) injects primary nuclei from the top of the atmosphere, takes into account all of the relevant interactions for particles which are interacting each other and the atmosphere, as well as derives the spectrum at a given altitude [72].

(iii) **Empirical model:** This approach is based on parametrised curves which can be fitted to the existing measured muon flux data. There is large amount of data which parametrise the different parts of the muon spectrum, however the precise parametrisation of the whole spectrum has not been performed yet [73]. If the approximate thickness of the investigated object is known, one can choose and apply a suitable model for its imaging by cosmic muon tracking.

Let's consider here the approach (iii), empirical model based muon spectrum incorporating a number of existing measurements. One of the most successfully model is described by the following formula [73]:

$$f_\mu(E_\mu, \theta) = A\, E_\mu^{-\kappa} \Big[ \frac{1}{1 + (\frac{a_0\, E_\mu}{\epsilon_\pi})\, \cos(\theta)} + \frac{B}{1 + (\frac{a_1\, E_\mu}{\epsilon_K})\, \cos(\theta)} \Big] \ , \tag{20}$$

where the adjustable parameters are the factor $A$, spectrum index $\kappa$, the so-called balance factor $B$ which determines the branching ratios for the parent mesons and $a_0, a_1$ coefficients. There are different parameter sets of this model which are summarised in Ref. [73] by N. Lesparre *et al.*. For example, the so-called Gaisser-parametrisation is the following:

A = 0.14, B = 0.054, $\gamma$ = 2.7, $\epsilon_\pi$ = 115 GeV, $\epsilon_K$ = 850 GeV, and $a_0 = a_1 = 1.1$ [74]. The curvature of the Earth reduces the thickness of atmosphere layers, therefore spherical geometry is needed to take into account at large zenith angles ($\theta > 70^\circ$) [73]:

$$\cos(\theta^*) = \sqrt{1 - \frac{1 - \cos^2(\theta)}{1 + \frac{H_{atm}}{R_{Earth}}}} \ , \tag{21}$$

where $H_{atm}$ = 32 km is the upper production altitude of muons and $R_{Earth}$ = 6,370 km is the radius of the Earth. Equation (20) overestimates the differential muon flux below the energy of 100/cos($\theta$) GeV.

This model was extended to lower energies ($E_\mu < 100$ GeV) by E. V. Bugaev *et al.* [75] and an empirical parametrisation was proposed for all zenith angles and the energy range from 1 GeV to 2 TeV by D. Reyna [76]:

$$f_\mu(E_\mu, \theta) = A \cos^3(\theta) p_\mu^{-\left[a_0 + a_1 \log_{10}(p_\mu \cos(\theta)) + a_2 \log_{10}^2(p_\mu \cos(\theta)) + a_3 \log_{10}^3(p_\mu \cos(\theta))\right]} \ , \tag{22}$$

where $p_\mu = \sqrt{E_\mu^2 - E_0^2}$ is the muon momentum, $E_0$ = 0.105 GeV is the rest mass of muons and the parameters are the following: $A$ = 0.00253, $a_0$ = 0.2455, $a_1$ = 1.288, $a_2$ = -0.2555, and $a_3$ = 0.0209. Based on the model of D. Reyna, the differential flux of muons was calculated for different zenith angles and are plotted in Fig. 38. The choice of differential muon flux model becomes crucial when one extracts the density-lengths from the measured integrated muon flux. The comparison of different spectrum models is discussed in Sec. 4.3.

Let's consider the interaction of cosmic muons with the matter to determine the flux of penetrated muons and to derive the density-length along muon paths. Charged particles interact with the matter via ionisation, bremsstrahlung, electron-positron pair production, and nuclear interaction. Energy loss of cosmic muons is expressed by the following equation in the matter as a function of density-length, $L$ [73].

$$-\left(\frac{\mathrm{d}E_\mu}{\mathrm{d}L}\right)_{total} = a(E_\mu) + b(E_\mu) E_\mu \ , \tag{23}$$

where the $a(E)$ term represents the energy loss which is resulting by ionisation and described by the Bethe – Bloch formula, as it is presented in Sec. 2.1. The $b(E_\mu)$ factor represents the energy loss by bremsstrahlung, electron-positron pair production and photo-nuclear interactions. The *upper panel* of Fig. 39 shows the total energy loss of muons as a function of their energy in GeV. The data was provided by Ref. [22] and fitted by a fourth-order polynomial function by N. Lesparre *et al.* [73].

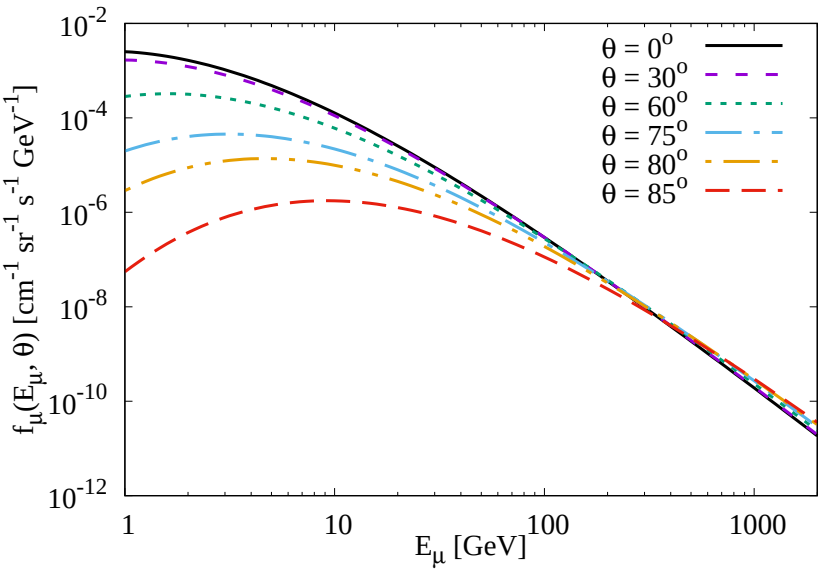


Figure 38: The differential muon flux, $f_\mu(E_\mu, \theta)$ was calculated at different zenith angles in the energy range of 1 GeV - 2 TeV based on the parametrisation of D. Reyna [76].

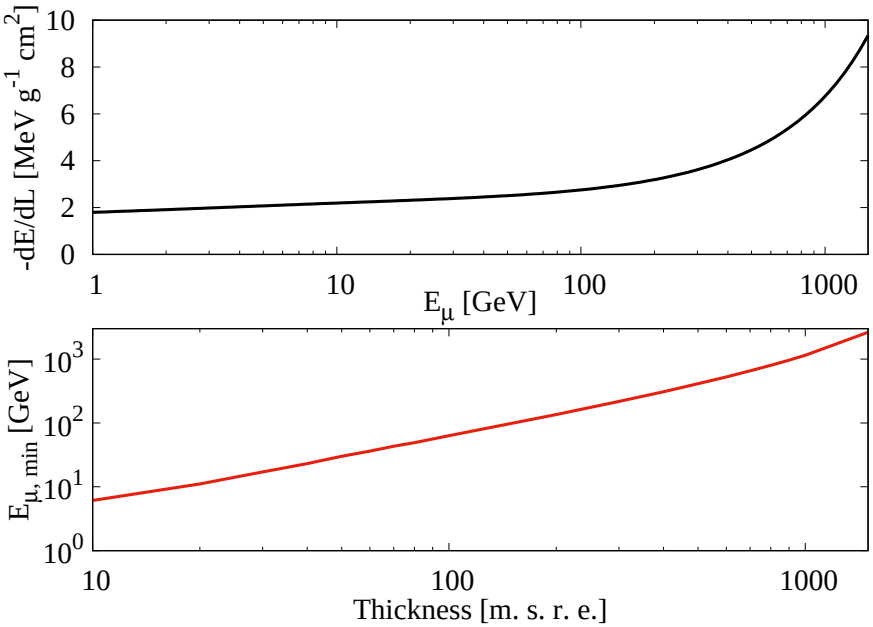


Figure 39: *Upper:* The energy loss of cosmic muon with the energy $E_\mu$ was parametrised by fourth-order polynomial function based on the data of Ref. [22] by N. Lesparre *et al.* [73] *Lower:* The minimum energy which is necessary for a muon to penetrate the standard rock is plotted as a function of rock thickness in meter-standard-rock-equivalent units.

The integrated flux of the muons which penetrated across the matter with the density-length $L$ is measured practically by tracking detectors in muon radiography. The integrated flux of muons is the integral of the differential flux of muons from the minimum energy which is necessary to penetrate across the material, $E_{\mu,min}$ to the end of muon spectrum, $E_{\mu,max}$. The minimum energy of muons can be expressed with their total energy loss on the density-length $L$ and their rest mass, $E_0$ [73]:

$$E_{\mu,min} - \int_0^L \frac{\mathrm{d}E_\mu}{\mathrm{d}L}\mathrm{d}L = E_0 \ . \tag{24}$$

The *lower panel* of Fig. 39 shows the minimum muon energy versus thickness in the unit of meter-standard-rock-equivalent[3] (m. s. r. e.). For example, the minimum energy values which are necessary to penetrate across standard rock of 10 m, 100 m, and 1,000 m are 6 GeV, 63 GeV, and 1,200 GeV respectively. The value of $E_{\mu,max}$ is model dependent, in case of the model of D. Reyna, it is 2 TeV. Finally, the integrated flux of muons which could penetrate the density-length $L$, $F_\mu(L,\theta)$ can be calculated by the following integral using Eq. (24) [73]:

$$F_\mu(L,\theta) = \int_{E_{\mu,min}(L)}^{E_{\mu,max}(L)} f_\mu(E_\mu,\theta)\mathrm{d}E_\mu \ [\mathrm{cm}^{-2}\mathrm{sr}^{-1}\mathrm{s}^{-1}] \ . \tag{25}$$

Figure 40 shows the integrated flux of muons as function of density-length in meter-standard-rock-equivalent (m.s.r.e.) units for certain zenith angles. At larger density-lengths, above 300 m.s.r.e. the flux of more inclined muons become more abundant. Based on the integrated flux versus density-length curves, one can derive the density-length across the body of interest by measuring the attenuated flux behind the body of interest. Thereafter, the average density can be determined with the knowledge of thickness of the body. In case of volcano muography, the thickness is provided by geodetic measurements. If the average density along of the investigated body is known, one can calculate the thickness of the body. The average densities can be also provided by electric-resistivity- or gravity measurements in case of cavity research by underground muography.

## 4.3 Systematic effects of muon radiography

As shown by the applications of cosmic muon tracking, presented in Sec. 4.1, both of the measured and the calculated fluxes influence the muographic image of the body of interest.

[3]The meter-standard-rock-equivalent is the thickness of standard rock, given in meter units. Standard rock has $A/Z = 2$ and $\rho = 2.65$ g/cm$^3$, where $A, Z$ are the mass and atomic numbers and $\rho$ is the density.

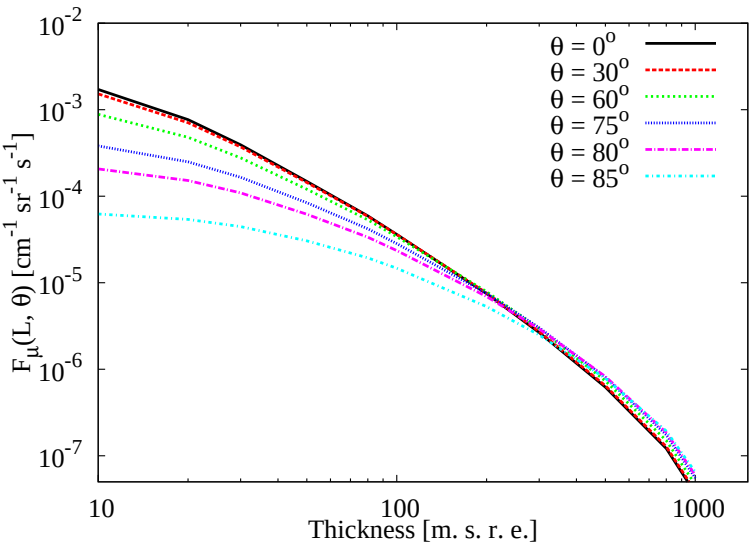


Figure 40: The integrated flux versus standard rock thickness was calculated at different zenith angles based on the model of D. Reyna [76] and plotted in Fig. 38.

In this section, the systematic effects are discussed.

The choice of a suitable model is a critical point to calculate the integrated muon flux. Large amount of experimental data exist for muon spectrum parametrisation. This causes significant discrepancies between the different spectrum parametrisations. Systematic comparison of different models in underground laboratories and at volcanoes are discussed in Ref. [73]. N. Lesparre *et al.* calculated that the relative difference between models can be 5-30 %, e. g. between the Gaisser [74] and Reyna [76] models in different energy regions. The model proposed by Bugaev [75] overestimates the integrated flux with three orders of magnitude compared to the other models, especially at lower energies. The approximate systematic error of density estimation, coming from the differential flux models, can be about 10 % for near horizontal muons and about 15 % for vertical muons.

The composition of the investigated object causes only a negligible systematic effect on the calculated muon flux via the density-length determination [77].

Location and time dependent systematic effects affect the measured flux of cosmic muons. Therefore, the measurement site causes also systematic effects in muon radiography. The detailed description of the systematic effects can be found in several papers, e. g. in Refs. [9, 71, 73, 77] or in Ref. [78]. Here only a brief summary is provided.

(i) **Solar modulation:** The variation of velocity of solar wind changes the low-energy part of the spectrum of primary cosmic rays [9, 73, 78]. The flux uncertainty caused by the solar modulation is decreasing with increasing momentum, e. g. it resulting 1 (10) % effect on the flux of particles with the energy of 10 (1) GeV.

(ii) **Variation of atmospheric conditions:** The changes in the atmospheric temperature, $T$ modifies the measured muon flux, $F$ at sea level [71, 73]. There are two competitive effects on $F$ as increasing the temperature. The atmosphere expands, the air density decreases, thus the decay probability of mesons increases which results increased muon flux. The opposite effect comes from that fact the expansion of atmosphere increases the path of muons across the atmosphere, therefore generates more muon decays which decreases the measured flux at sea level. The relative variation of the measured muon flux, $\Delta F/F$ caused by the relative change of temperature, $\Delta T/T$ is described by the following equation [73]:

$$\frac{\Delta F}{F} = \alpha_T \frac{\Delta T}{T} \ , \tag{26}$$

where $\alpha_T$ is the temperature coefficient which depends on the $K/\pi$ ratio and the critical energy of the mesons. Temperature effect causes a seasonal variation on the flux of the high-energy muons. Typically, a 5-10 % of flux variation was observed in underground laboratories [73]. The temperature effect need to take into account during long-term measurements. Note that a pressure effect also exists, however it causes negligible ($< 1$ %) variation on the flux of muons at sea level [78].

(iii) **Altitude dependence:** The measured muon flux depends on the distance between the detector level and production level of muons. It parametrised by the following formula [73]:

$$\frac{F(h)}{F(0)} = \mathrm{e}^{-h/a(p)} \ , \tag{27}$$

where $F(h)$, $F(0)$ are the muon flux at the altitude of $h$ and at sea level, respectively. The $a(p) = 750p + 4,900$ is a momentum dependent scale factor where $p$ is the momentum in GeV/c units. For example, this effect causes increase of about 9 (0.5) % for 1 GeV (100 GeV) muons at the altitude of 500 meter. Therefore, the altitude of detector level is relevant for muon radiography, especially for the estimation of flux of background particles.

(iv) **Geomagnetic latitude:** The geomagnetic field affect the penetration of primary cosmic rays across the atmosphere and define a threshold rigidity[4] for them. This threshold is negligible at the poles and it is about 15 GV near the equator. This effect influences the flux of muons only below 5 GeV [73].

To conclude, the location and time of muon flux measurement or the choice of the muon spectrum model can affect the radiographic image about the body of interest. Furthermore, the physical background noise can distort the image. The next section focuses on this issue.

## 4.4 The physical background noise of muography

Besides the penetrated muons, the physical background noise which consists of particles from hadronic- and electromagnetic component of cosmic rays is also detected under open sky. The integrated flux of vertical electrons and positrons is approximately 30, 6 and $0.2\,\mathrm{m^{-2}\,s^{-1}\,sr^{-1}}$ above 0.01, 0.1 and 1 GeV, respectively. For vertical protons it is about $0.9\,\mathrm{m^{-2}\,s^{-1}\,sr^{-1}}$ above 1 GeV [22]. At sea level, the total flux of these components is less than 1.5 % of the flux of muons, and becomes negligible with increasing energy. If one investigates an object with the thickness of about a kilometer, e. g. a mountain or a volcano, the measured muon flux decreases with two orders of magnitude after the object, and the physical background noise becomes non negligible. The presence of the physical background noise results increased rate of fake tracks in the detector system which generates higher muon flux, and lower density-length values than the real ones. The identification or suppression of these particles is crucial to improve the signal-to-noise ratio of muography. Figure 41 summarises the possible background noise sources of muography under open sky. Electrons, protons and low-energy muons can not penetrate through the investigated object, but these scatter, deflect or decay in the atmosphere, and arrive also from the direction of the investigated object. In addition, the hadronic interaction of protons and neutrons with atmospheric nuclei creates electrons and muons which are also detected from the direction of the body of interest. Low-energy particles scatter also inside the soil and enter the detector from its back side. These are the so-called upward-going particles which produce the similar trajectories inside the detector as muons from the direction of the investigated object, and can be rejected by the measurement of TOF [77, 79, 80, 81].

[4]Rigidity measures the effect of magnetic field on the motion of charged particles inside it. Rigidity is defined by $\vec{R} = \vec{p}/q$, where $\vec{R}$ is the rigidity, $\vec{p}$ and $q$ are the momentum and charge of the particle.

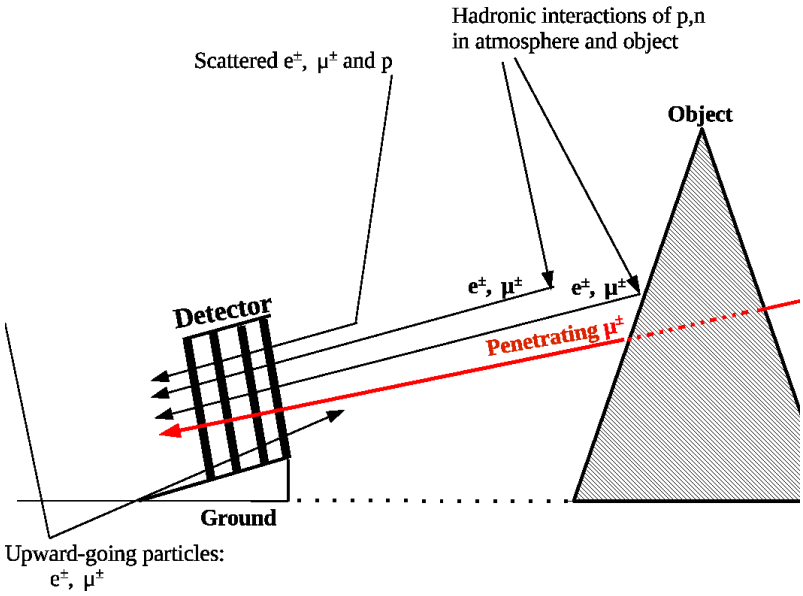


Figure 41: Scheme of a muon radiography measurement under open sky and the possible background sources.

To determine the sources of physical background noise with their spectra and to separate them from the spectrum of penetrated muons, a simulation-based study was performed by R. Nishiyama *et al.* [81]. Naive models of the earlier investigated Mt. Showa-Shinzano lava dome and the corresponding measurement site was created in a GEANT4 simulation framework. The Mt. Showa-Shinzano lava dome was modelled with a bump with 200 m height, 1 km diameter, and average density of 2 g/cm$^3$. Muons were generated and injected across the investigated lava dome. The energy spectrum of muons was parametrised by COSMOS simulation which was developed to reproduce the energy spectra of cosmic particles in the atmosphere [82]. In the simulation, detectors were deployed all around the lava dome, the spectra and the fluxes of particles were quantified from different regions of the lava dome which are shown in the *left panel* of 42. It was found that more than 84 % of background particles with the energy above 50 MeV are originated from hadronic particles and those muons and electrons which were created in hadronic interactions in the atmosphere and within the investigated object. 23 % and 44 % of total flux of background particles with the energy above 50 MeV is originating from upward-going particles from R2 and R3 regions, respectively. In this case, the energy spectrum of physical background noise did not exceed 1 GeV, as shown in the *right panel* of Fig. 42. Based on these results,

the earlier measurements which were performed at Mt. Showa-Shinzano lava dome had to be re-analysed, and so the extracted densities became consistent with the earlier geological measurements. These results confirmed that tracking detectors with energy threshold of 1 GeV can suppress sufficiently the background particles under open sky.

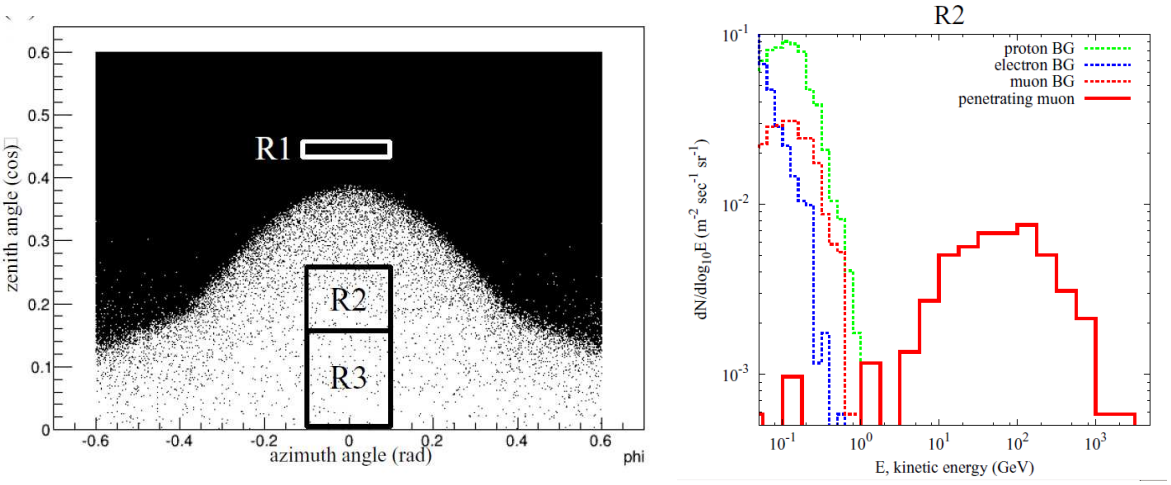


Figure 42: *Left:* The model of Mt. Showa-Shinzano lava dome was created in GEANT4 simulation framework. The investigated regions are signed R1, R2 and R3 [81]. *Right:* The energy spectra of background (BG) particles from R2 region was quantified. Energy threshold of 1 GeV was suggested for tracking detectors in future measurements under open sky based on this result [81].

To conclude, muography is very sensitive for low-energy background particles which originate from hadronic interactions and scattering processes. To perform reasonable measurements, one needs to minimise the physical background noise in the detector. As a rule of thumb, tracking detectors with energy threshold of 1 GeV can suppress sufficiently the physical background noise. However, specific studies of background sources at different measurement situations are necessary. These results provided a basis to my study focused on optimisation geometry and material-budget for the developed tracking system operated under open sky. This study is presented in Sec. 5.7.

## 4.5 Tracking detectors for environmental applications

The finite flux of cosmic muons limits the applicability of muon radiography. To allow a reasonable measurement, the detector surface, acceptance and efficiency is to be maximised. However, one has to optimise the detector size to the local environment at the

observation point as well. To perform reliable measurements out of the laboratory, the applied detector technology should be robust, durable, portable with low power consumption. An optimal cosmic muon tracker has reasonable angular and position resolution, high detection efficiency and low noise. It is also useful if its operation does not require a specialist and provides real-time data.

Actually, there are no standard technology for outdoor tracking detectors which are optimised for all of the above mentioned requirements. Presently, three different and competitive technologies can be applied for cosmic muon imaging:

(i) **Plastic scintillators with photo-multiplier tubes:** Charged particles crossing the detector, create photons with the typical yield of 1 photon per 100 eV of energy deposit via scintillation. Plastic scintillators are shielded from external light and internally reflective for the photons. Photons are detected most commonly with a photo-multiplier tubes (PMTs). The scintillators produce relatively fast signals ($\sim$ ns) and with the coincidence of multiple detector layers one can detect cosmic particles with high efficiency ($> 99\,\%$). Due to the relatively fast signal production, scintillators are applicable for time-of-flight measurement of particles across the tracking system and thus discriminate the upward- and downward-going particles. Though plastic scintillator trackers are very robust, their weight is not optimal for environmental applications and portability is a serious issue. The PMTs can work in wide temperature range, whereas their power consumption is relatively high. Scintillator trackers typically have 5-10 cm segmentation. To optimise their position resolution one has to increase the number of PMTs which drastically increases the power consumption and cost of the detector system. The *upper panels* of Fig. 43 show two examples for scintillator trackers which were developed by DIAPHANE group [83, 84] (*left*) and the Earthquake Research Institute (ERI) of the University of Tokyo [63] (*right*).

(ii) **Nuclear emulsion detectors:** These foils are manufactured from a plastic base and emulsion gel with a total thickness of 200-300 $\mu$m and consist of AgBr micro-crystals and gelatin. Emulsions films provide 3-dimensional particle detection [85]. After chemical development, the Ag crystals show the particle trajectories. The tracks are reconstructed by automated microscope scanning device. The typical readout speed of detector scanners are about 50 cm$^2$ per hour [86]. The *lower left panel* of Fig. 43 shows a microscope image of a nuclear emulsion film with a remarkable

cosmic muon track. These detectors provide very good ($\sim \mu$m) position resolution and very efficient in background rejection via the visualisation of the multiple scattering of low-energy particles [80, 87, 88]. Nuclear emulsion detectors can operate without any electricity, maintenance and their structure is modular, therefore one can perform measurements at sites which are difficult to access. This technology is very tolerant to mechanical shocks and water, however it can not work above room temperature ($> 25\,^{\circ}C$) because the higher temperature increases the speed of fading effects in which the number of grains decrease along the tracks. Nuclear emulsions have no dead time and continually accumulate the tracks of charged particles from their production, thus these detectors are capable to record data for about 6 months under the rate of cosmic rays at sea level. An important disadvantage is that one can not perform real-time measurement with these detectors because of their readout. Nuclear emulsion films are not applicable for monitoring purposes, e. g. for volcano eruption prediction, whereas they are very good candidates as complementary detectors and those measurements where real-time data are not crucial, such as pyramid muography [89].

(iii) **Gaseous detectors:** This technology can be a promising candidate for cosmic muon tracking. Gaseous detectors were presented in Sec. 2, here just presented shortly from the muon radiography point of view. These provide fair position- and angular resolutions, low-material budget for relatively low price. The variation of environmental parameters are affecting the gas gain and consequently by the tracking efficiency of gaseous detectors, thus correction on this effect is necessary to provide reliable tracking information during the data taking. One example is the Glass Resistive Plate Chamber which were applied for the radiographic imaging of the Puy de Dome volcano in France. The *lower right panel* of Fig. 43 shows a tracking system consists of GRPCs developed by the TOmographie MUonique des VOLcans (TOMUVOL) collaboration [90]. This detector concept is robust, modular, and easily transportable. Two main issues of GRPCs are the relatively high power consumption and the safety issues with applied toxic gas mixture. Micromegas-based tracking systems were also developed for cosmic muon tracking [91]. These are also applied to image the interior of the pyramids at Giza in Egypt [92].

In this section, the advantages and limits of muon radiography were presented. The applied particle detector technologies were reviewed from this application point of view. The following sections focus on the R&D and the application of gaseous detector systems for cosmic muon imaging.

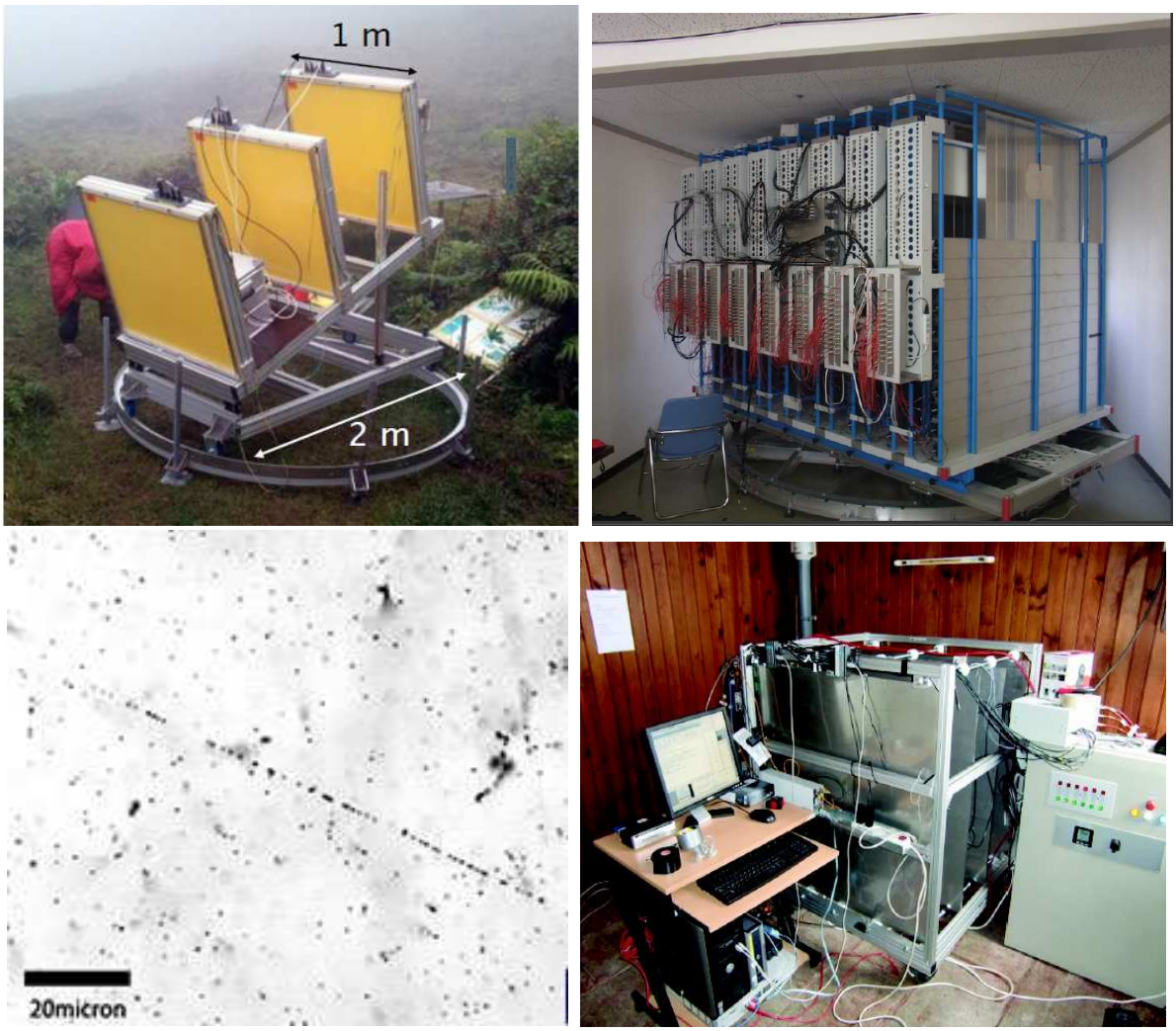


Figure 43: *Upper Left:* Photo of a scintillator-based tracking detector which was applied for muography of La Soufriére of Guadeloupe volcano by the DIAPHANE group [83]. *Upper right:* A photo about a scintillator tracker which was developed by the Earthquake Research Institute of the University of Tokyo and was applied to image the inerior of the Satsuma-Iwojima volcano [63]. *Lower left:* A microscopic image of a nuclear emulison film with a cosmic muon track [80]. *Lower right:* A photo about tracking detector constructed from Glass Resistive Plate Chambers and its data acquisition system which were developed by the TOMOVUL collaboration [90].

# 5 Development of gaseous detectors for muography

The tracking systems applied for muography in the recent years inherited the detector technologies from the HEP experiments. These were not optimised for outdoor measurements. One of my aims was to specifically develop and optimise tracking systems for muon radiography. The design of the tracking systems was motivated by two applications:

(i) search for rock density inhomogeneities and hidden caves,

(ii) image the interior of large size objects, such as volcanoes by tracking of the near-horizontal muons under open sky.

In this chapter, I focus on the R&D of tracking systems using the newly developed CCC and MWPC detectors for these applications of cosmic muon tracking.

## 5.1 General structure of the developed tracking systems

The design of the tracking systems takes into account some contradicting aspects, such as detection surface, resolution, tracking efficiency, mobility, power consumption, and cost considerations. In case of underground measurements, the accessibility of the interior of the investigated object limits the size and the weight of the detector for human handling.

Large-size objects, such as volcanoes are imaged from lateral direction under open sky. The rate of the near-horizontal muons is limited because of their angular distribution and the size of the body of interest. These physical properties imply the vertical arrangement of the detector layers in the muon tracker. In addition, lead absorbers are used between the tracking layers to suppress the physical background noise. The gaseous tracking systems can measure precisely the deflection of particles in the absorbers due to their reasonable position resolution. Therefore, the lead absorber layers are used as scatterers, instead of truly stopping the particles. To measure precisely the angular deflection of the low-energy background particles, the distances between tracking layers should be optimised.

In both of the applications, the tracking systems are operated in outdoor conditions. Concerning this fact, the main detector requirements are summarised as follows.

- Sustainable and safe operation: During the data taking, low maintenance is expected, whereas the outdoor installation requires safe and environmentally sound operation.
- Long term operation under varying outdoor conditions: The temperature, the pressure and the humidity variations should be tolerated in a wide range.

The photos of the developed tracking systems are shown in Fig. 44: a portable tracking system is based on CCC detectors for underground muography (*left*), and a modular, MWPC-based system for tracking near-horizontal muons under open sky (*right*).

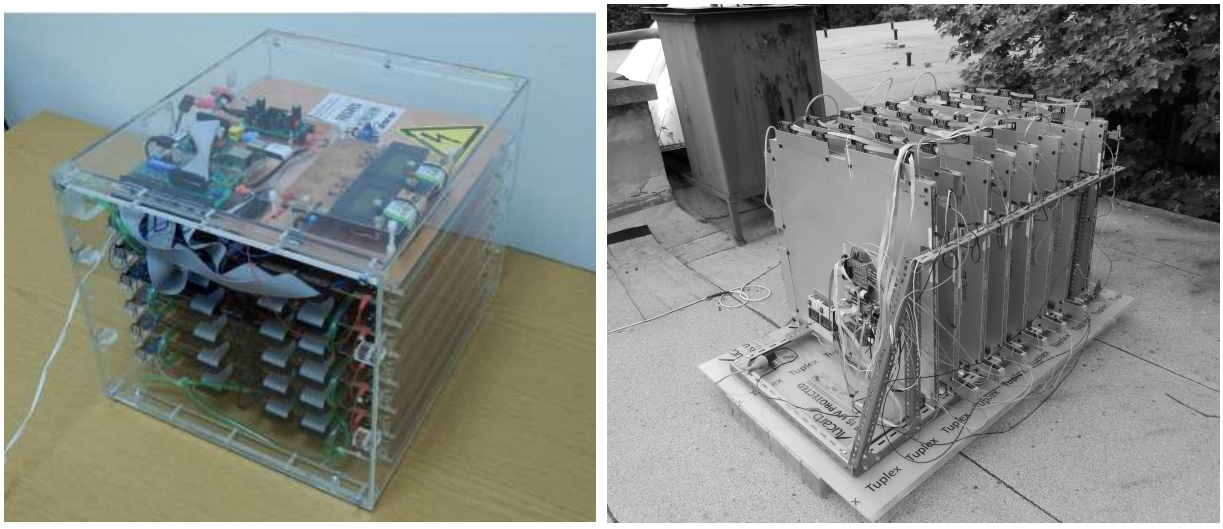

Figure 44: Photos about the developed tracking systems: a CCC-based tracker for underground muography (*left*) and a MWPC-based system (*right*) for imaging by tracking the near-horizontal muons.

For underground muongraphy, close cathode chamber-based tracking systems were developed [OL08, OL09, OL10, OL11]. The latter system has volume of $37 \times 32 \times 28$ cm$^3$, and its total weight is about 15 kg without the gas bottle and the batteries. It is relatively easy to handle manually. This tracker consists of six layers of CCC detectors with the detection surface of $25 \times 25$ cm$^2$ and with the equidistant spacing of 35 mm. Thus, the distance between the upper and the lower CCCs is 17.5 cm, which implies the angle of view of 56° for the tracking system in both pad and field wire directions. The chambers are housed within a solid box with 6 mm plexiglass walls. This box protects the tracker against the small mechanical shocks arising during transportation and installation, as well as isolates that from the surrounding humid atmosphere.

The MWPC-based tracker is the first prototype of a large-size ($\sim 10\,\mathrm{m}^2$) and modular tracking system, which will be applied to image the interior of large-size targets, such as volcanoes [OL01, OL12]. The final geometries, e. g. spacing between tracking layers, and mechanical support structures are under optimisation. Here the developed prototype consists of six or eight MWPCs with the surface of $80 \times 80$ cm$^2$. The tracking layers are placed vertically within a steel stand with equidistant spacing of 20 cm, as shown in the *right panel* of Fig. 44. The weight of a modular system is about 80 kg with the eight chambers and the stand. During the outdoor test measurements, the tracking system is covered by a solid plastic box with the volume of $100 \times 200 \times 100$ cm$^3$.

Both tracking systems require continuous gas flow during their operation. As presented in Sec. 2.3.1, the FC18 gas mixture is applied with the flow of about 0.5-2 L/h. This gas mixture is supplied from a standard bottle with the volume of 10 L and the maximal pressure of 150 bar. The premix passes through a pressure regulator (pressure of about 0.5 bar is suggested for these detectors), flows across an adjustable mechanical flow meter, and reaches the tracking system through a plastic tube. One gas bottle is sufficient for about 30-120 days continuous operation with the nominal gas flow. The detectors are connected in series with the gas tubes and the gas flows across the full tracking system. In case of the CCC-based system, the gas is exhausted from the last tracking layer inside the plexiglass box in which the humidity is reduced to 20-30 %. Due to the influence of the temperature variations on the gas, a one meter long tube was added to the gas outlet of the last tracking chamber in the MWPC-based tracking system.

The high- and the low voltage power supplies, the data acquisition system, and the front-end electronics were designed with the consideration of the power efficiency and the portability. The description of these detector elements is presented in Sec. 5.3.

## 5.2 Construction of the tracking layers

The development of the trackers were started by the construction of tracking layers. Here I summarise the construction procedures and the corresponding technical details. Figure 45 shows highlighted photos about the chambers and the construction steps.

I built the close cathode chambers for the portable tracking system applied for underground muography. The time of the construction of one pair of CCC detectors is about 5 days, limited by the time of the gluing procedures. A commercial two-component epoxi

glue is applied for all gluing processes. First of all, the wire-planes were produced by an automatised winding machine. After the winding, the wire-planes were fixed onto the baseplates. For each chamber, the wire spacing of 2 mm is provided by two laser engraved plastic bars glued onto the baseplates. Thereafter, the electric connections of the wires were soldered onto the baseplates. The chambers were closed with plexiglass walls and with the upper cathodes. Finally, the electronic connectors to transmit the output signals, and the high voltage connectors were soldered onto the chambers.

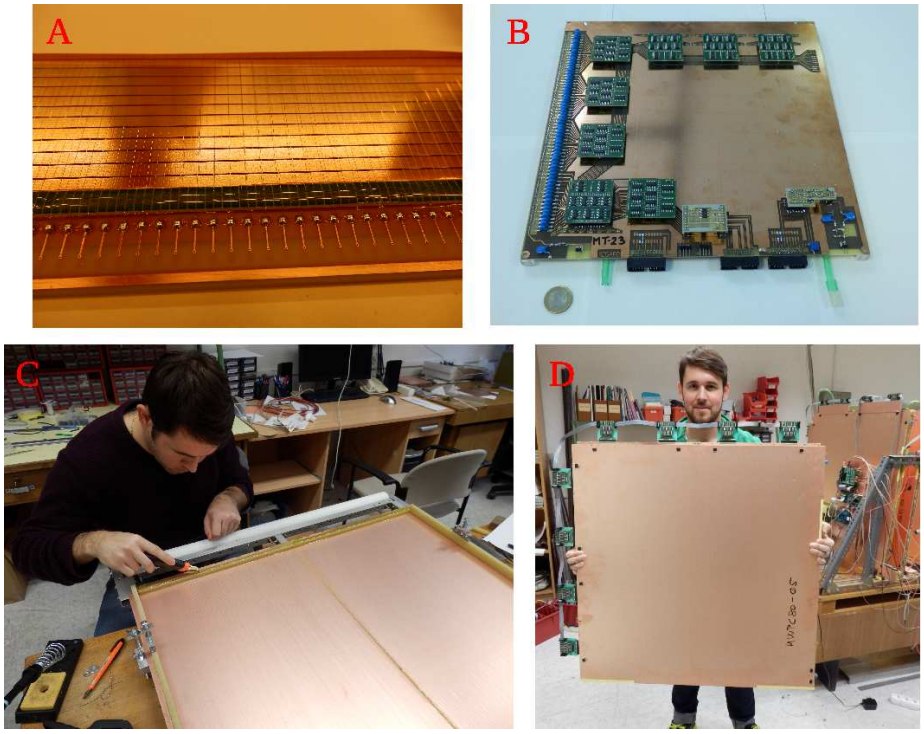


Figure 45: The highlighted photos about the construction of CCCs (A-B) and MWPCs (C-D). **A:** The wire-plane of the CCC detector is glued into lased engraved plastic bars placed on the lower cathode plate. **B:** The photo of a CCC chamber after the construction procedure. **C:** A photo about the wire fixing of the MWPC detector. **D:** A photo about the light-weight MWPC detector before the installation into the tracking system.

I constructed the large-size MWPC detectors together with the REGARD group [OL01]. The MWPC detectors were also built in pairs. The duration of the construction procedure was 5 days. The gluing procedures were also performed with two-component epoxi glue. As presented in Sec. 2.3.1, the build-up of MWPCs differs from the structure of CCCs, thus the construction procedures are also different.

In the first step, the printed circuit boards with the wire signal outputs were glued onto the lower copper plates. The copper plates were placed onto a hand-driven winding frame. The pick-up wires were winded and soldered to the printed circuit boards on the copper plate. Thereafter, the copper plates were rotated by 90° on the winding frame, the sense- and field shaping wires were winded onto the frame. In the next step, six-six support pillars were glued into the chambers. Finally, chambers were closed by the upper cathode, electronics, and high voltage connectors were soldered onto the chambers.

After the construction of the detector layers, the gas tests and the high voltage tests were performed on each tracking layer. First of all, the FC18 gas mixture was flowed through the chamber and the gas output was led into a bubbler. Presence of leaks on the chamber was indicated by lack of bubbles. In normal case, no leak was observed down to the gas flow value of about 0.1 L/h, which value was five times lower than the applied gas flow of 0.5 L/h during detector operation.

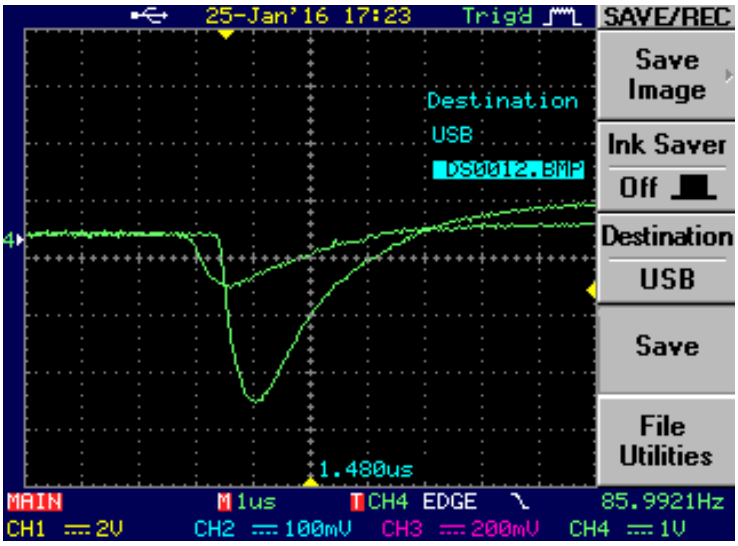


Figure 46: The oscilloscope image of a typical signal produced by a cosmic particle on the sense wires of the MWPC detector.

A high voltage test followed the gas leakage test. The high voltage was connected to the sense wires (in case of CCC on the field wires are on high voltage with the value of the half of sense wire voltage) and it was gradually increased above the nominal values: 1,100 V for CCCs and 1,800 V for MWPC detectors. The measured current values were below 10 nA per chamber for each of the CCC or MWPC detectors. The low current shows that, the power consumption of the tracking layer is negligible without FEEs.

The common signal of the sense wires was led out to an oscilloscope via an amplifying card. Besides the cosmic particles, a $^{90}$Sr $\beta$ source was also applied to investigate the shape and frequency of chamber signals. The typical frequencies were about 80-200 Hz for cosmic particles and 2.5-3 kHz using the $^{90}$Sr $\beta$ source. Figure 46 shows an oscilloscope image of a MWPC signal produced by a cosmic particle.

## 5.3 Description of the power and data acquisition systems

Both of the CCC-based and the MWPC-based tracking systems use the same Front-End Electronics and apply the same data acquisition system developed by the REGARD group. I constructed and optimised these separated modules for the tracking systems. Based on the blueprints, the printed circuit boards were created. Thereafter, the components (capacitors, resistors, connectors, switches, etc) were soldered onto the boards. Finally, the complete modules were tested in the tracking systems.

Figure 47 shows a photo of the power system and a Raspberry Pi computer (RPi) [93] controlled data acquisition system. These systems and the principles of their operation are described briefly in the following sections. These descriptions help to understand the operation of the detector system and my work focused on their optimisation.

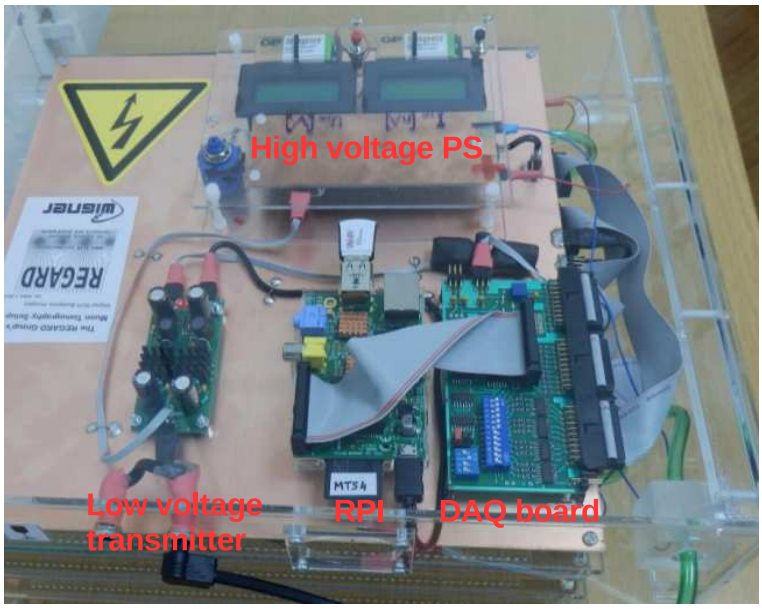


Figure 47: The power and DAQ systems on a CCC-based tracking system. Additional modules can be connected to the system for readout analogue signals from each chamber.

A dedicated low voltage transmitter module receives stabilised 12 V from a battery or a wall plug power supply. It transmits the 12 V to the high voltage power system. The transformed and filtered 5V output is transmitted to the RPi and the DAQ board.

The high voltage power supply is based on American High Voltage (AHV) modules [94]. Different AHV modules were applied for CCCs and MWPCs. For the CCCs, the AHV has two outputs, a positive one for the sense wires and a negative one for the field wires and the cathode. The high voltage can be set by a potentiometer from the outside of the plexiglass box. For the MWPCs, the AHV unit supports the high voltage in the positive range 0 V - 3000 V, and a single output line is used to supply the sense wires, while the other electrodes are on ground potential.

The power consumption of the high voltage power supply is 30 mA at 12 V (360 mW). The power consumption is 310 mA at 12V (3.72 W) for the data acquisition system which includes the RPi, the DAQ board, and the front-end electronics (48 piece in a tracking system which consists of 6 chambers total of 48×16 channels). Thus, the total power consumption of the tracking system is less than 5 W. This is lower by a factor of ten compared to the power consumption of the tracking systems applied for muography recently, as shown in Tab. 2 in Sec. 5.9. Both tracking systems can be operated for about one week by a couple of commercial 50 Ah car batteries.

Multi-channel Front-End Electronics were developed by the REGARD group for the amplification and the discrimination (digitisation) of the analogue signals produced on the field shaping wires, and on the pads (or on the pick-up wires). The FEEs are connected to the outputs of the detector segments of the tracking layers. The used FEEs, named DIN416, are based on standard Complementary-Metal Oxide Semiconductor (CMOS) technology with 16 channels. The signal amplification is provided by the CD4069 inverters and the MC14001B NOR commercial logic gates in non-conventional analogue mode with resistive feedback. Thereafter, the amplified signals are transmitted to shift registers, which digitise the measured analogue signals via the comparison of their amplitudes to the digitisation threshold, which has a common value for all channels of the FEEs. Therefore, the output of each channel is a binary information, it is "1" if the signal amplitude is above the digitisation threshold, or it is "0" if the signal amplitude is below the digitisation threshold. The FEEs are connected into series and the digital data are transmitted via a single data line from each chamber to the DAQ board.

Note that the analogue readout of the detector segments is also possible and it provides at least from three to six times better resolution for the tracking layers [26]. As the application of the analogue data readout increase drastically the power consumption and the cost of the detector system, the digital one is preferred for environmental applications. The first prototypes of the these FEEs, the so-called DIN316 cards are presented in Ref. [95].

A trigger card is placed on each tracking layer. It is connected to the output of the common signal of the sense wires. This card uses the similar but faster amplification part as the DIN416 card to provide sufficiently large signals with the amplitude of about 1.5-3 V. The trigger thresholds can be set by a potentiometer placed on the chamber. The trigger threshold of the chamber was set to provide the trigger efficiency above 99 % with input threshold of 32 fC. To measure precisely the amplitude of the sense wires' signal, a 10-bit ADC is also used on the trigger card. Here 1 ADC unit is equal with the charge of 1,800 electrons (0.3 fC).

The data acquisition system is based on a custom designed board operated by a Raspberry Pi computer. The photo of the DAQ board is shown in Fig. 48. This is responsible for the trigger, the communication between the RPi and the tracking layers, and the transmission of the data from the tracking layers to the RPi. It is supplied with 5V produced by the low voltage power supply, presented above.

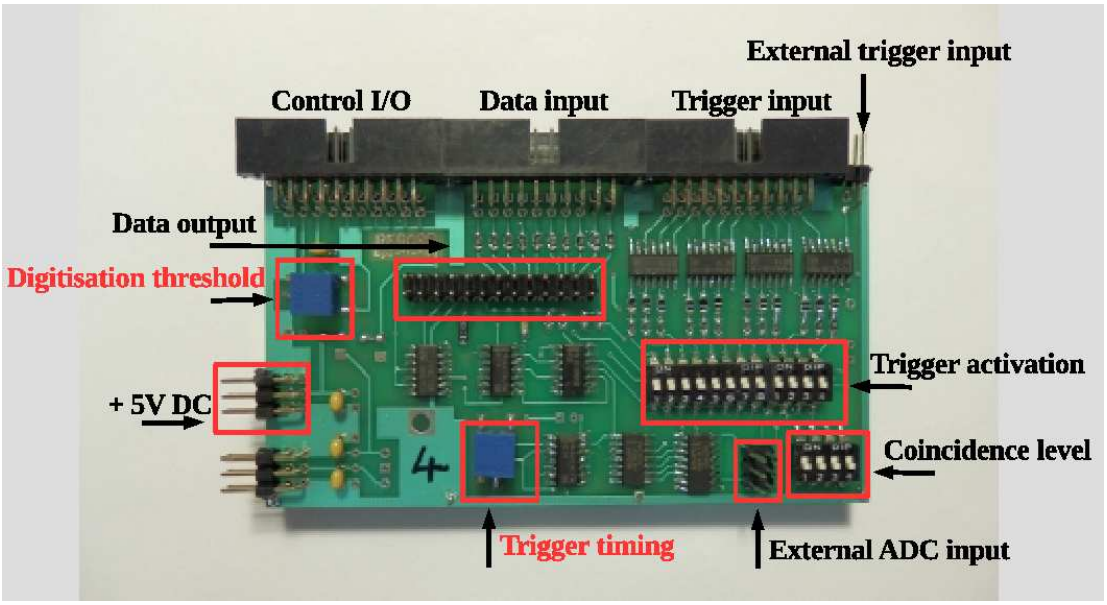


Figure 48: The DAQ board is responsible for data transmission from the tracking layers to the Rasberry Pi [96].

The DAQ board includes a coincidence unit with 12 trigger input lines. Ten lines from the tracking layers, one from an external trigger, e. g. a signal from a scintillator can be used as trigger; and an oscillator trigger on the DAQ board, which produces uncorrelated trigger signals to measure the noise. The trigger inputs can be selected manually by the trigger activation switch array. The coincidence level can be chosen by an another activation switch array. The timing of the accepted trigger signal is set by a potentiometer. The accepted trigger signal is provided by the coincidence of different trigger signals, where the coincidence level can be chosen by an another switch array. The individual trigger signals and the number of missing triggers are also recorded.

The common digitisation threshold of the signals measured on the field wires and pads (pick-up wires) with the amplitude of 0.1-0.5 V can be set by a potentiometer on the DAQ board.

The FEEs are placed in series for each chamber, while the chambers are read in parallel to minimise the dead time. In addition, the possibility to read in external ADC signals, such as the data from a Temperature-Humidity-Pressure (THP) sensor is also provided. These signals together with the digitised trigger signals are transmitted to the RPi via the data output. The data reading sequence is governed by the control input/output, including Look-At-Me (LAM), Busy, and Clock between the FEEs and the DAQ board.

The operation of the DAQ system is presented via a simplified example, shown in Fig 49. Here there is only one chamber and the data readout is triggered by the trigger signal of the chamber. When a charged particle crosses the chamber, it generates a signal on the sense wires ($a$). If the common signal of the sense wires is above the trigger threshold of the chamber, it flips the trigger bit, and received by the DAQ board ($b$). The individual chamber trigger signals are combined to produce the physics trigger. In most of the measurements an "at least two" input coincidence was used. If the readout line is not busy, the coincidence trigger becomes an Accepted Trigger (AT). The anagolue part of trigger electronics is faster than the ones on the DIN416, thus the AT shall be delayed to match with the peaks of the signals on the FEEs, thus maximising the signal-to-noise ratio ($c$). The leading edge of the AT generates a Look-At-Me signal toward the RPi, indicating that the readout can be started ($d - e$). This LAM is used as a busy signal during the readout of the data, and blocks the meanwhile coming coincidence triggers. The RPi sends an asynchronous clock and reads the data on the 10 input lines in parallel bit-by-bit. These data contain the digital info of the DIN416 electronics, the ADCs, and the THP sensors as

well. Due to the small amount of the data and the low trigger frequencies, no buffering was needed, thus the length of the data-readout signal (LAM) is the dead-time of the system. After the RPi reads all the predefined amount of bits, it sends a short Read-End (RE) singal, resets the LAM, and thus allows new triggers to be accepted ($f$).

To maximise the detection efficiency of the tracking systems, the above presented parameters (dead time, trigger timing, and digitisation threshold) were optimised experimentally, as presented below.

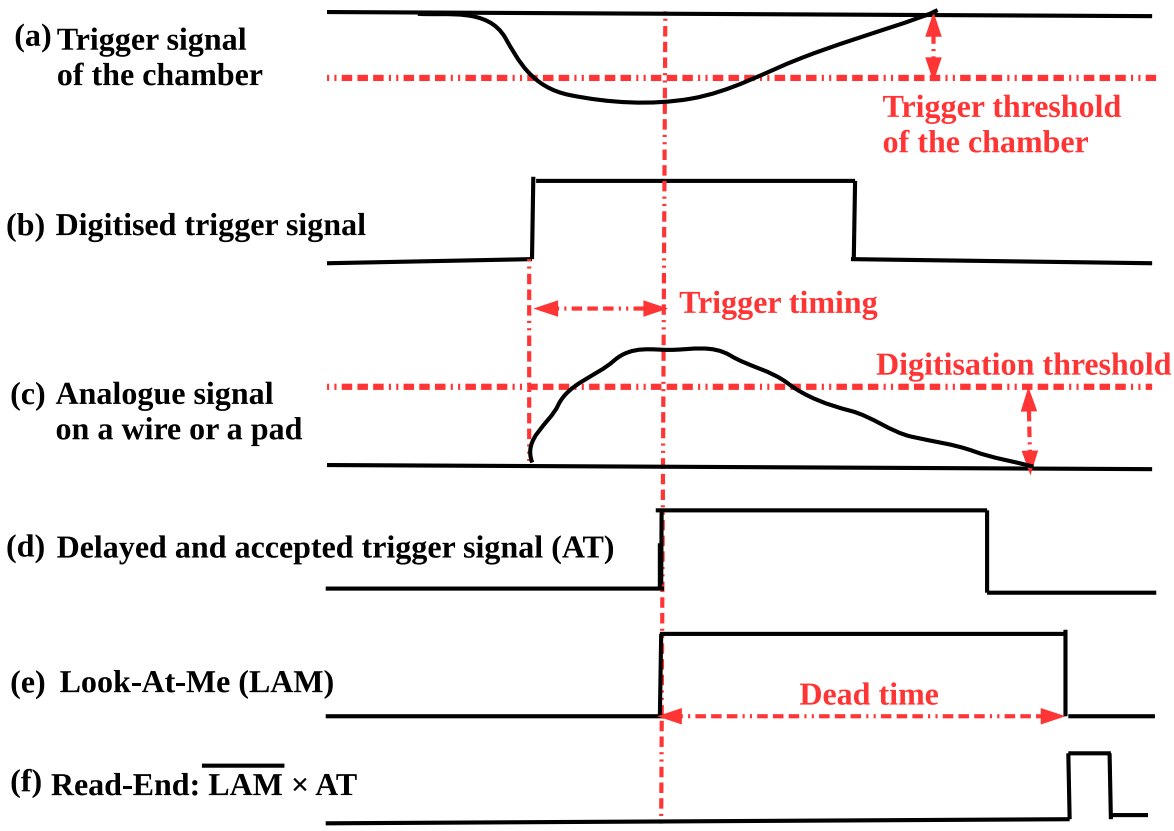


Figure 49: The operation of the DAQ is preseted via a simplified example. The trigger signal is produced by the signal of the sense wires of the tracking layer. When it is above the trigger threshold ($a$). The trigger signal is digitised ($b$), and delayed to the maximum of the analogue signals produced by the detector segments ($c-d$) to read out the digitised data from the tracking layer at the suitable time. When the delayed trigger turns to high level, it starts the LAM signal, which allows to the RPi to read out the data ($e$). When the data readout is finished, the LAM signal goes down, activates the triggering ($f$), and the DAQ waits for the next trigger signal which starts again the taking procedure.

The DAQ software runs on the Raspberry Pi [96]. It is responsible to control the measurements and to record the data. The read-out bit series are sorted and zero suppressed, as well as written as ASCII files on event-by-event basis (compressed if necessary). One event corresponds to one line in the file, and it contains the following data: event number, time relative to the last event in the units of microseconds, zero suppressed position info for all chambers, ADC signals, and trigger pattern. The size of one complete event is about 100-200 bits. After the data file is closed, it is compressed by zip program. The data is recorded on a SD card with the memory of 16 GB. It can contain 6 weeks data with the typical trigger rate of 40-50 Hz measured under open sky.

## 5.4 The data analysis framework

Reliable reconstruction of the trajectories of particles is the first step to optimise the operational parameters, to determine the performance, and to calculate the flux of the penetrating particles. As a part of my Ph.D. work, I developed an analysis framework for these tasks. The scheme of the analysis framework is shown in Fig. 50. It consists of two main parts: the "pre-analysis" and the "analysis". Both parts use the same data files, apply the same cuts, and perform the same algorithms to reconstruct the clusters on each chamber, as well as to find the tracks.

First of all, the "pre-analysis" is performed. This is responsible for the following tasks:

- Filtering of the noisy FEE channels: The pre-analysis counts the hits on each channel, and fills the *Hitmap*). If a channel fires five times more often than the average value of the hits on the chambers, then that channel is excluded from the further analysis. This exclusion suppresses the rate of fake tracks caused by the noisy FEE channels.
- Positioning of the tracking layers: Each tracking layer is installed with well defined geometry inside a plexiglass box, or in a stand. However, small ($\sim$ 1-6 mm) lateral displacements are possible. The displacement in one direction is determined by the average value of the distribution of the difference between the measured and fitted track coordinates. This is calculated in both directions for each chamber.

After the pre-analysis, the analysis reads the results of the pre-analysis, performs the corrections, and reconstructs the tracks. From the tracking information, the efficiencies, position and angular resolutions, as well as the flux of penetrating particles are determined.

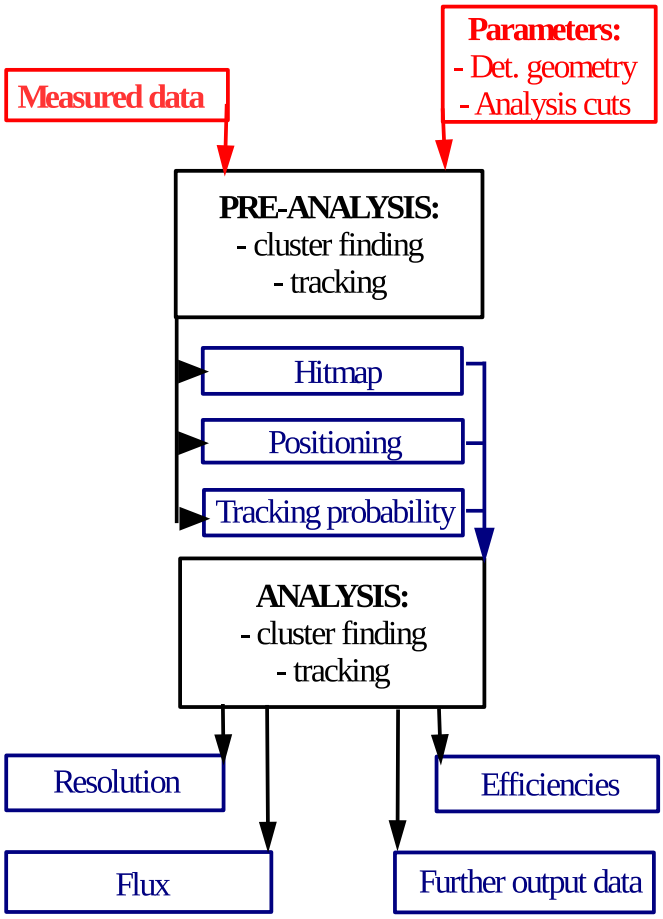


Figure 50: The scheme of the analysis framework.

Both analysis start with the application of the cluster finding algorithm in both the pad and the field wire directions on each chamber. It reconstructs the centroids of the clusters, the sizes of the clusters, and the total number of clusters per chamber. If the digitised field wire or pad signal is equal with 1, the channel is fired. The cluster is formed by consecutive fired channels.

After the cluster finding, the trajectories of the particles are reconstructed. These are straight tracks across the chambers. The cosmic particles produce typically one or two clusters per chamber, which result in one or two tracks per event (the number of events with the track multiplicity above 2 is less than 0.5 % of the total number of the reconstructed tracks). For the reconstruction of these low multiplicity events, a combinatorial

tracking algorithm was developed. It uses the cluster positions and the chamber distances to calculate the track parameters. The algorithm gathers clusters from each chamber into a track candidate, thus the number of track candidates is equal with the number of cluster combinations. The combinatorial algorithm works sufficiently well with the low track rate of cosmic particles. Note that the chambers has projective geometry, and the track coordinates are measured independently in the field wire and in the pad (or pick-up wire) directions. Consequently, the reconstructed tracks projections can be mixed if more then 1 track is found.

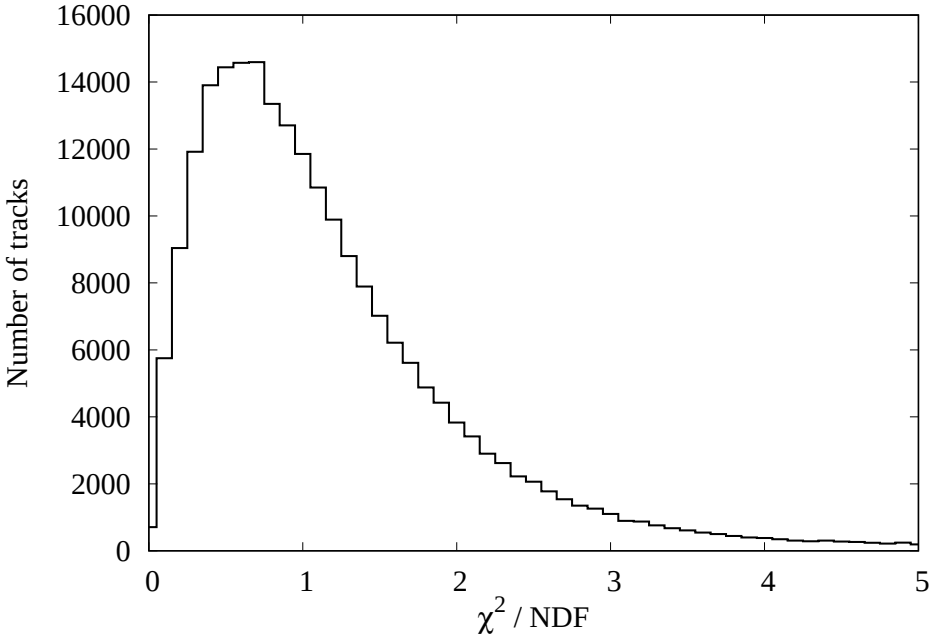


Figure 51: An example of $\chi^2$/NDF distribution for MWPC-based tracking system.

In the next step, the track candidates are fitted with lines. The "goodness", $\chi^2$/NDF of each track candidate is calculated by the following expression [OL01, OL08]:

$$\chi^2/\mathrm{NDF} = \frac{1}{\mathrm{NDF}} \sum_{i=0}^{N_{ch}-1} \frac{[(measured_i) - (fitted_i)]^2}{\sigma_i^2} \ , \tag{28}$$

where $\chi^2$ is the sum of the normalised deviations of the measured position from the fitted track position. The track fit has four parameters: two slopes and two intercepts. The number of degrees of freedom is NDF=$2 \times N_{ch} - 4$, where $N_{ch}$ is the number of chambers applied in the tracking system, and $\sigma_i \approx \sigma$ is the position resolution of the tracking layers.

An example of the distribution of $\chi^2/NDF$ values is shown in Fig. 51. The average value of the distribution is around 1, which indicates that the fit is reasonable. The tracks with $\chi^2/NDF < 2$ are accepted as "straight tracks". After the determination of the goodness of fits, the candidates are sorted and the best ones are chosen and used for further calculations.

Figure 52 shows an example of a typical event measured by the CCC-based tracking system. There are 64 field wires and 64 pads in this system. The fired detector segments are marked with "*" characters, and the ones which did not fire with "." characters. The cluster multiplicity per chamber is 1 or 2 for each layer. The clusters belong to the reconstructed track are signed with "X" letters. The positions of these clusters are also plotted here.

```
Event number:   5314

Field wires:
Number of clusters: 1    ..X.............. ................ ................ ................     Track position:  2
Number of clusters: 1    ....XX.......... ................ ................ ................     Track position:  4.5
Number of clusters: 1    .......XX....... ................ ................ ................     Track position:  7.5

Number of clusters: 1    ..........X..... ................ ................ ................     Track position:  10
Number of clusters: 2    .......**...XX.. ................ ................ ................     Track position:  12.5
Number of clusters: 1    ...............X X............... ................ ................     Track position:  15.5


Pads:
Number of clusters: 1    ................ ................ ................ ...........XX...     Track position:  59.5
Number of clusters: 1    ................ ................ ................ .......XX.......     Track position:  55.5
Number of clusters: 1    ................ ................ ................ ...XX............     Track position:  51.5

Number of clusters: 1    ................ ................ ................ .X..............     Track position:  49
Number of clusters: 2    ................ ................ ..***........XX. ................     Track position:  45.5
Number of clusters: 1    ................ ................ ..........XX.... ................     Track position:  42.5
```

Figure 52: The event display of a CCC-based tracking system consists of six detectors. Each CCC layer has 64 field wires and 64 pads. In both dimensions, the fired segments are denoted by "*" characters, and the reconstructed track coordinates are denoted by "X". The number of reconstructed clusters, and the coordinates of the track are also plotted.

After the reconstruction of the particle trajectories, the detector performance parameters, such as the tracking efficiency, the position and angular resolutions are calculated. The description of these methods are provided in Sec. 5.5. Furthermore, calculation of the muon flux is presented in Sec. 6.1.

## 5.5 Optimisation of the tracking systems for muography

In this section, the optimisation of the operational parameters and the performance of the tracking systems are presented.

### 5.5.1 The dead time, trigger and tracking efficiencies

As presented above, the trigger unit does not receive trigger signals during the data readout. This is the dead time of the tracking system (the length of the LAM signal). The distribution of time differences between consecutive events is shown in Fig. 53. The consecutive physical events produced by cosmic particles are independent from each other and these arrive with the same probability at any time. Consequently, the distribution of the time differences is expected to be exponential distribution. The *inner panel* of Fig. 53 shows the same distribution with the time bin size of 10 $\mu$s. Here the dead time is the smallest time value where the number of time differences are measurable. The dead time was found to be 400 $\mu$s.

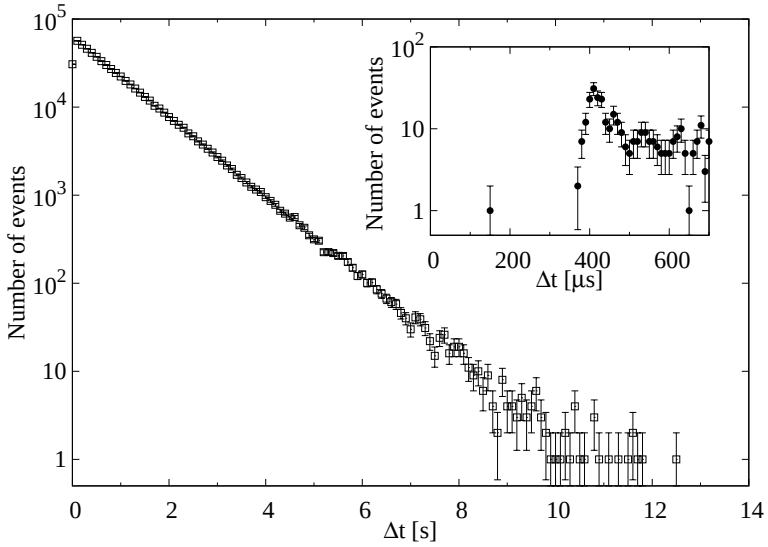


Figure 53: The distribution of time differences between events with the time bin sizes of 0.1 s and 10 $\mu$s (*inner panel*). The dead time was found to be 400 $\mu$s.

A key figure of merits of the tracking detectors are the trigger and tracking efficiencies. The trigger efficiency is the probability to trigger for a particle in a given chamber. The tracking efficiency is the probability to determine a specific point of trajectory of the detected particle.

The trigger efficiency is calculated by a dedicated algorithm. In the first step, it chooses a specific detector layer and reconstructs the particle's trajectory from the other chambers excluding the layer under study. If there is straight track, then the algorithm checks the digitised trigger signal of the investigated chamber. The trigger efficiency is the ratio of the number of cases in which the trigger bit is 1 to the total number of comparisons.

The trigger efficiencies were found to be above 95 % for each of the layers. The data taken was triggered by the twofold coincidence of any of the six tracking layers in case of each detector system. The resulting trigger efficiencies were found to be well above 99 % in case of both tracking systems.

Tracking efficiency is determined as the follows. The first step is the reconstruction of tracklets. It is the same procedure as applied to calculate the trigger efficiency. Thereafter, the algorithm extrapolates the tracklets to the investigated chamber, and investigates the digitised detector segment signals at the expected positions near the extrapolated coordinate (within 5 sigma of the position resolution, ± 2 detector segmentation units). The tracking efficiency is the ratio of the number of found clusters to the number of tracklet extrapolations. The tracking efficiencies were found to be above 95% for each of the chambers in normal operational conditions.

### 5.5.2 Tacking efficiency of the detector system

The tracking efficiencies of the complete detector systems consist of six chambers were also determined. The tracking efficiency of the detector system is the probability to reconstruct tracks with 5 or 6 clusters, $\varepsilon_{tracking}$:

$$\varepsilon_{tracking} = \epsilon_0\epsilon_1\epsilon_2\epsilon_3\epsilon_4\epsilon_5 + (1-\epsilon_0)\epsilon_1\epsilon_2\epsilon_3\epsilon_4\epsilon_5 + ... + \epsilon_0\epsilon_1\epsilon_2\epsilon_3\epsilon_4(1-\epsilon_5) \ , \qquad (29)$$

where $\epsilon_i$, $i = 0, ..., 5$ are the individual chamber tracking efficiencies. The first term of the right side is the efficiency of the reconstruction of tracks with 6 clusters. The second term is the probability of reconstruction of tracks without a cluster from the first chamber, etc.

The resulting tracking efficiencies were found to be well above 99 % for both CCC-based and MWPC-based detector systems.

To optimise the applied high voltages for the tracking systems consist of six chambers, the tracking efficiencies were determined as a function of the applied voltage on the sense wires. Plateaus are observed for both CCC-based (*left panel*) and MWPC-based (*right panel*) tracking systems, as shown shown in Fig. 54. The CCC-based tracking system

reached fully efficient configuration (> 99 %) at the high voltage value of 1,050 V. In case of the MWPC-based tracker, the tracking efficiency of 95 % (99 %) was reached at 1,650 V (1,700 V) for the first and second detectors ("1" and "2") with 25 $\mu$m thick sense wires. Here the efficiencies were measured up to 1,800 V, where a stable detector operation was still observed. The third and the fourth chambers ("3" and "4") use 22 $\mu$m thick sense-wires. Thus, these reached the optimal efficiency at lower voltage values.

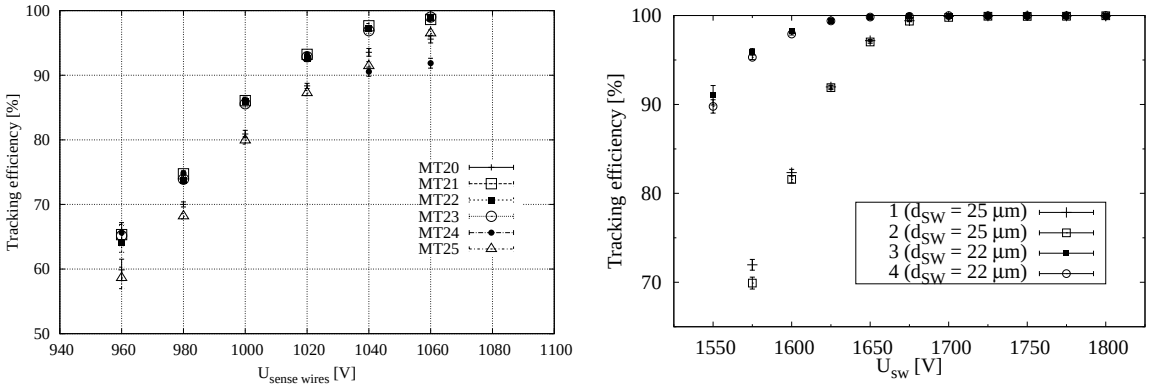


Figure 54: Tracking efficiency versus high voltage on sense wires for the chambers of CCC- (*left*) and MWPC-based (*right*) tracking systems. For both systems, plateaus are observed and the optima of high voltages on sense wires are 1,050 V and 1,700 V, respectively [OL01].

As presented in Sec. 5.3, the digitised and accepted trigger signal is faster than the analogue signals created on the wires and pads. Consequently, a certain time delay is necessary to compare the signal amplitudes at the maximum value to the digitisation threshold and to reach the maximal tracking efficiency. The next study focused on the optimisation of the trigger timing.

Figure 55 shows the tracking efficiency as a function of trigger time delay for both of the CCC-based (*left panel*) and the MWPC-based (*right panel*) tracking systems [OL01]. The maximum tracking efficiency values are found around the time values of 1.2 $\mu$s for the CCCs and 2 $\mu$s for the MWPCs. The determined time delays differ because of the different lengths of the sense wires. The capacity of the electrodes depends on length of the wires, as shown by Eq. (8), and in turn the capacity limits the speed of the signal. For this study, both systems were operated at lower sense wire voltages to measure the tracking efficiency below the plateau, where larger efficiency changes occurred. In case of the CCC-based tracking system, all chambers were on the sense wire voltage of 960 V. In

case of MWPC-based tracking system, the data were taken at the sense wire voltage of 1,700 V, except the middle two chambers on which lower sense wire voltages (1,600 V and 1,550 V) were applied. This procedure ensures reasonably high trigger efficiency (from four detectors) and a measurable efficiency (that is, well below 100%) for the inner layers.

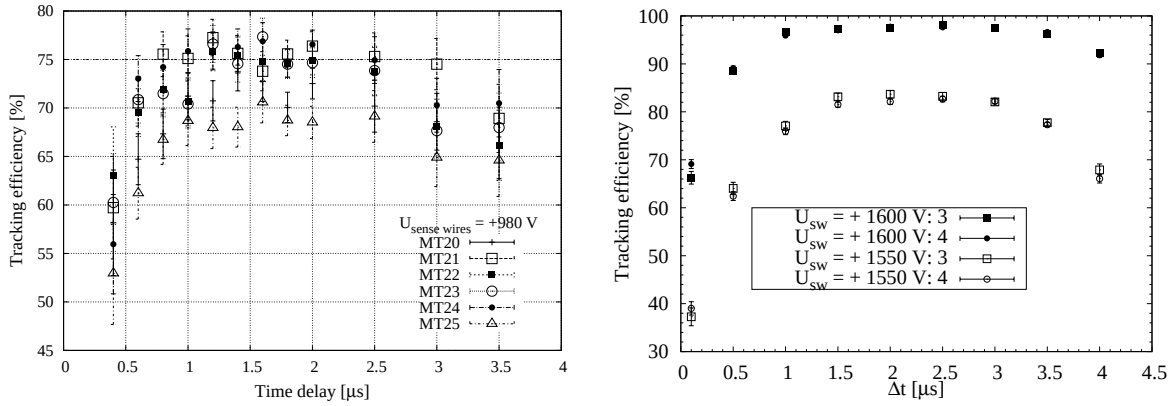


Figure 55: The tracking efficiency vs. timing delay are plotted for CCC- (*left panel*) and MWPC-based (*right panel*) tracking systems. The optimum time delay values are found to be 1.2 $\mu$s for the CCCs, and 2 $\mu$s for the MWPCs [OL01].

The tracking efficiencies as a function of FEE channels were determined for CCCs, shown in Fig. 56. These were found to be well above 95 % on average. The local efficiency losses were due to the degraded FEE channels [OL08].

The MWPCs are highly efficient ($> 95$ %) on each FEE channel [OL01]. If one measures the tracking efficiency map, one can see the local efficiency reductions at the place of support pillars. Figure 57 shows this effect on the tracking efficiency map. The data are taken in horizontal detector configuration. For this study, near-horizontal tracks were selected (within $\pm$ 200 mrad relative to the zenith). The pixel size in the efficiency map is 6 mm. As shown in the Figure 57, there is only small reduction (10-15 %) at the place of the support pillars. This unexpected high efficiency values near the pillars are caused by the fact that the pillars are smaller than the position resolution of the investigated chamber, presented below. Taking a 3 cm wide strip over the pillars (within dashed lines), the mean efficiency is plotted in Fig. 58 [OL01]. To the first order, one can conclude that the detector is sensitive for any muons which enter the gas volume around the pillars.

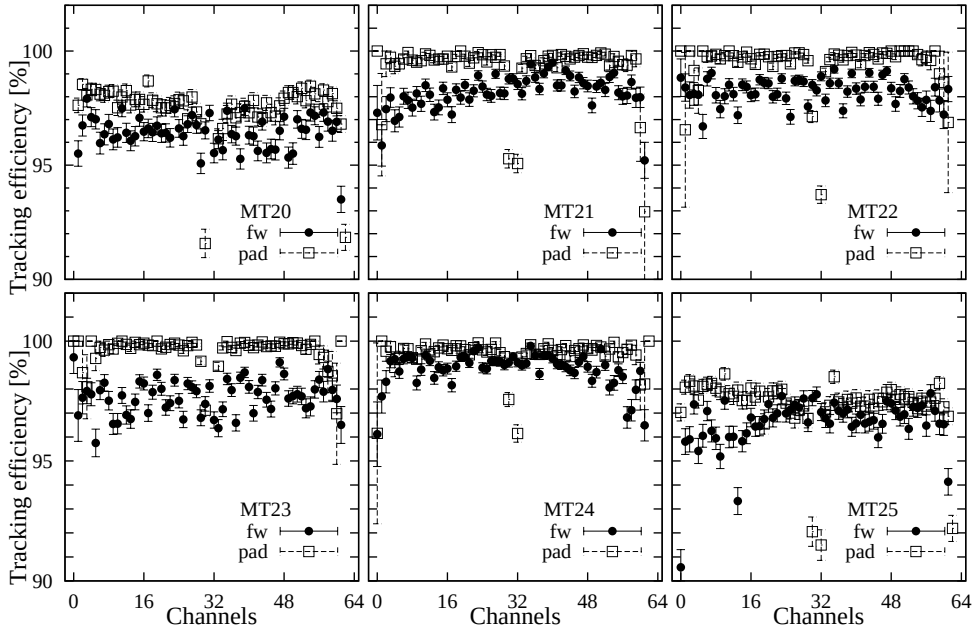


Figure 56: Tracking efficiency was calculated as a function of FEE channels for both the field wires (*fw*) and the pads (*pad*) with the same method, presented in Ref. [OL08].

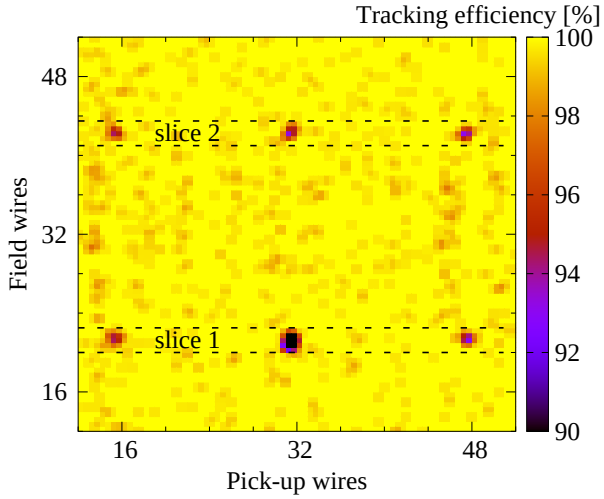


Figure 57: Efficiency map covering the region of the support pillars. The reduction which is caused by the support pillars is small and localised [OL01].

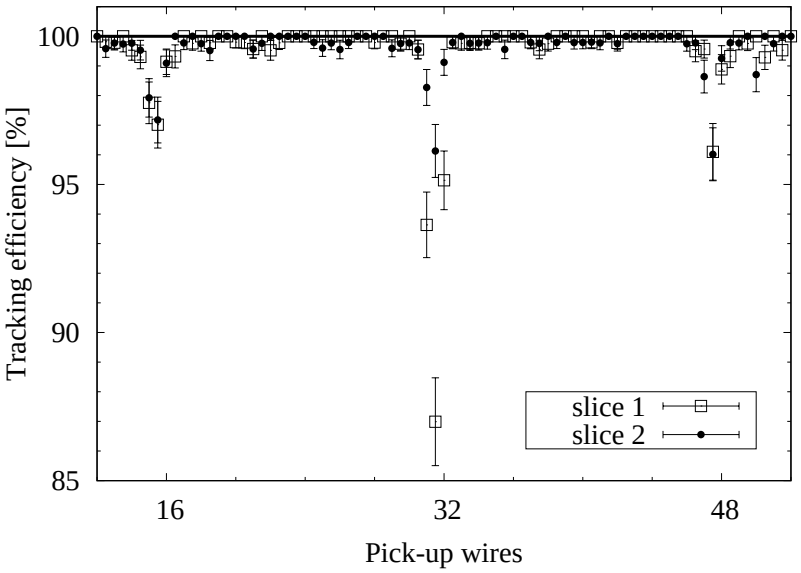


Figure 58: Efficiency drop around the support pillars (averaged over the 3 cm wide slice shown in Figure 57 indicated with the dashed lines) [OL01].

### 5.5.3 Position and angular resolution

The position resolution of the chambers were determined for both tracking systems. As described in Sec. 5.4, the position resolution was calculated from the difference between the reconstructed cluster centroids and fitted track intersection positions (residuals). Figure 59 shows the position resolution of the CCC-based tracking system consists of six chambers. In both the field wire (*solid lines*) and pad (*dashed lines*) directions the position resolution was found to be around 1.5 mm [OL08].

In case of the CCC-based tracking system, Fig. 60 shows the extracted position (*upper panel*) and angular resolutions (*lower panel*) as a function of zenith angle for both field wire (*empty rectangles*) and pad (*filled circles*) directions. As expected, the residuals are larger for inclined particles, which result in less precise positional resolution. The corresponding angular resolution is the position resolution divided by the track length across the detector and the number of tracking layers. The angular resolution was found to be below 16 mrad in both directions.

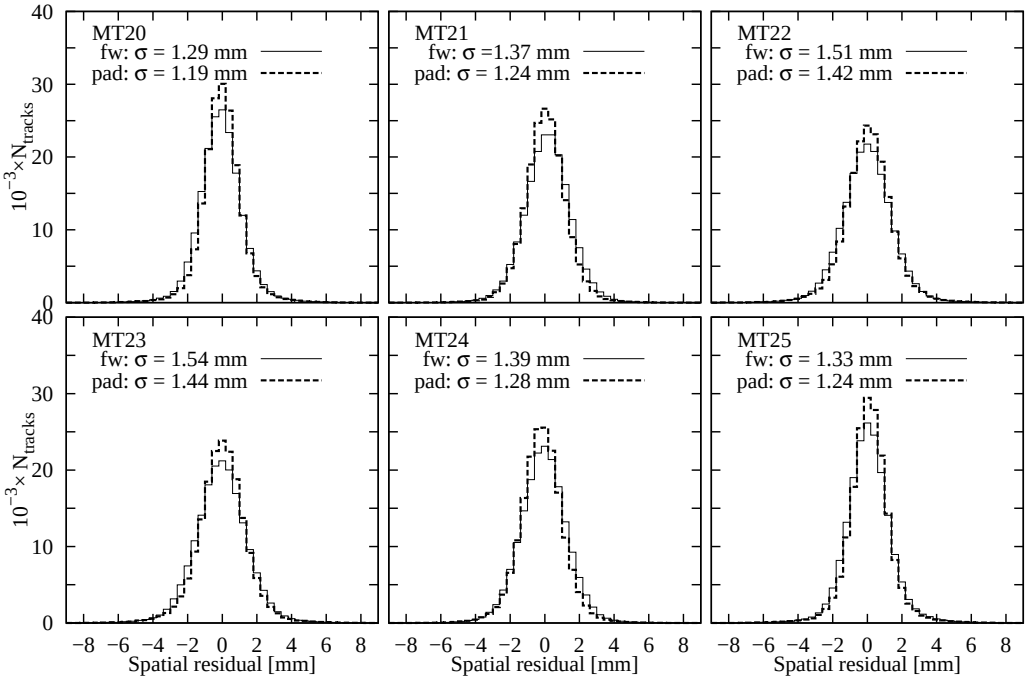


Figure 59: The resolution in both field wire (*solid lines*) and pad (*dashed lines*) directions are found to be around the value of 1.5 mm [OL08].

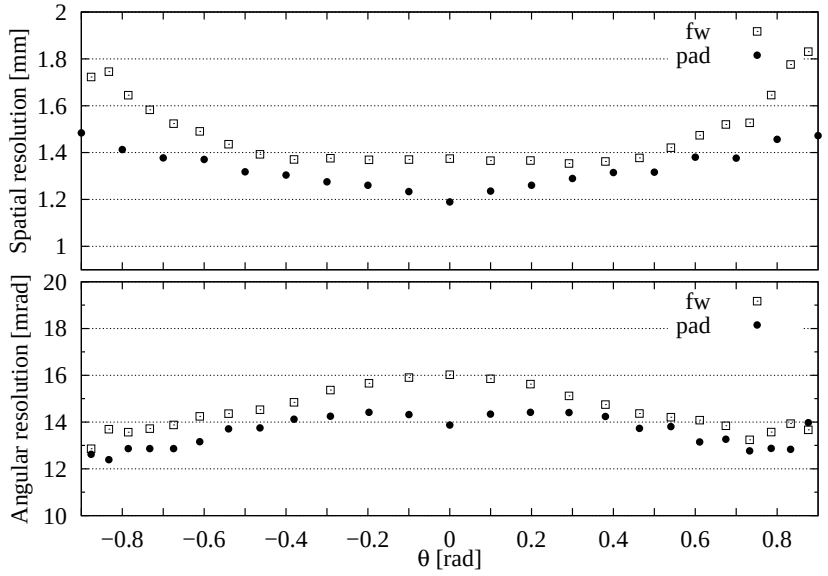


Figure 60: Position and angular resolution of CCC-based tracking detector as a function of zenith angle.

For MWPC-based the tracking system, the position resolutions of the chambers were also quantified by the same method [OL01]. Figure 61 shows an example of a residual distribution with the position resolution (RMS) of 3.73 mm in the field wire (*solid line*) and 3.92 mm in the pick-up wire (*dashed line*) direction. The residual distributions and the position resolutions were found to be the same for the other MWPCs. The values are roughly consistent with the expected position resolution of a detector with 12 mm position segmentation: 12 mm/$\sqrt{12}$ = 3.5 mm.

The angular resolution of the MWPC-based tracking system depends on the distances between the chambers. A further study was done to optimise the chamber distances, and the amount of absorber layers placed between the chambes. This is presented in Sec. 5.7.

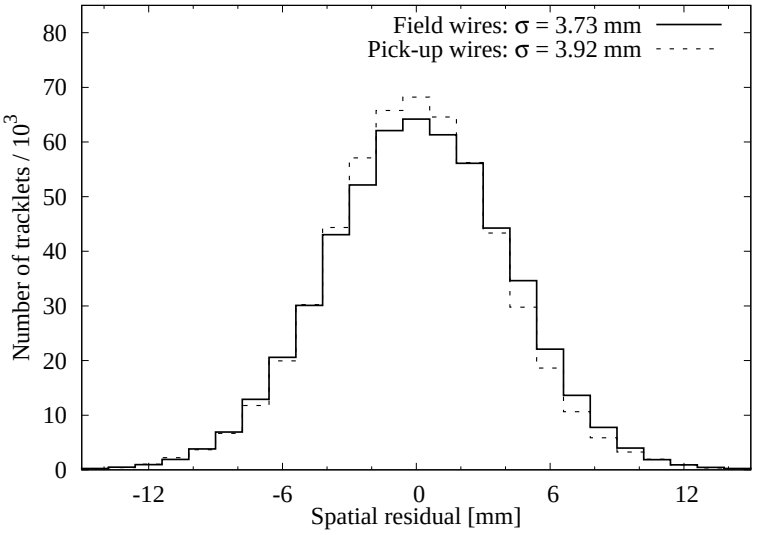


Figure 61: The position resolutions of the MWPC detectors in both field wire and pick-up wire directions were found be below 4 mm [OL01].

## 5.6 The instrumental background noise

As presented in Sec. 4.4, the physical background noise is detected as muons from the direction of the body of interest. In addition, the tracking system itself can produce noise. The fake tracks produced by the detector system itself are called the instrumental background noise. The fake tracks originate from the noisy FEE channels, or tracks from a randomly coincident, an independent particle due to the finite time resolution of the detector.

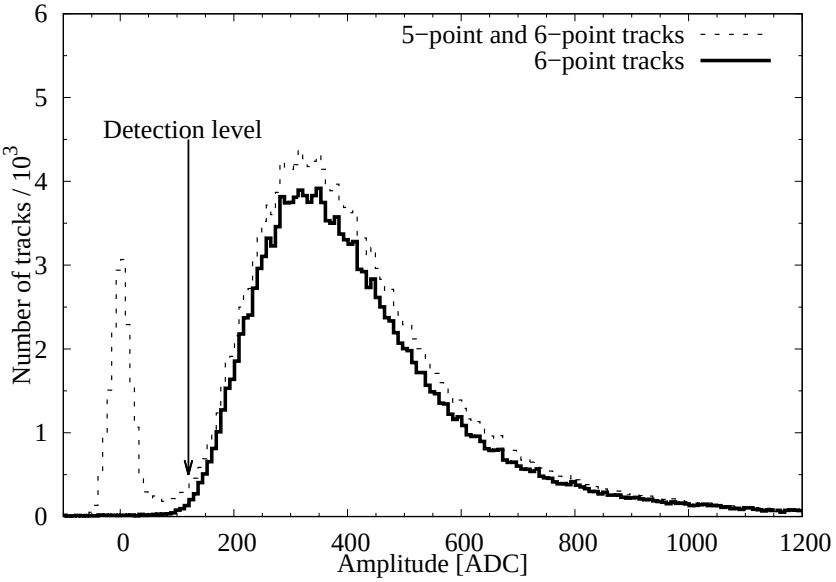


Figure 62: Distribution of analogue signals from an MWPC detector from all interconnected sense wires. *Solid line* shows those tracks which have a point detected in the investigated layer, and *dashed line* shows also those tracks which have no point in the investigated chamber [OL01].

The random electronic noise can produce fake tracks. These can be eliminated with a track selection cut applied on the amplitude of the analogue signal produced by the sense wires. Figure 62 shows an example of the analogue signal distribution for a chamber of the MWPC-based tracking system. The distribution of signal amplitudes for 6-point tracks (*solid*) follows the expected Landau-distribution, the distribution of the energy deposit of cosmic particles in the FC18 gas mixture. The distribution of 5-point tracks (*dashed*) contains those tracks which did not cross the investigated chamber. Consequently, the non-physical signals generate a Gaussian peak around the zero value. If an appropriate cut is chosen, the noise can be eliminated. In this case, the cut value was chosen to 125 ADC.

To minimise the noise clusters produce by the field wires and pads (or pick-up wires), the common digitisation threshold ($U_{th,DIN416}$) was optimised. Measurements were performed with different digitisation threshold voltages in the range 0.15 V - 0.45 V with/without application of high voltage on the tracking layers. Figure 63 shows the number of reconstructed clusters divided by the number of all events and the number of detector channels as a function of the digitisation threshold. If the digitisation threshold is below the optimal value, the noise clusters with low amplitudes are also detected. The number of clusters

increases drastically, which results in the loss of tracking efficiency. This effect was more obvious when the high voltage was not applied on the chambers (*filled markers*), and particle trajectories were not detected. Note that the size of error bars on the measured values are smaller than the size of points. The digitisation threshold value of 0.3 V was set for both tracking systems.

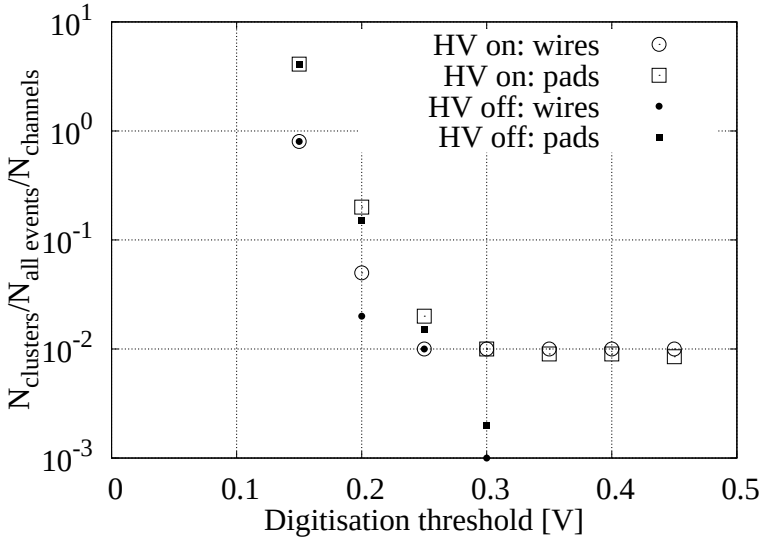


Figure 63: The digitisation threshold of 0.3 V was found to be optimal for the trackers.

The next step was the verification of that, the noise originates from the FEEs was exceedingly small. Without the application of high voltage on the chambers, triggers were not expected. The probability of the observation of fired channels was found in the order of $10^{-6}$. Consequently, the probability to detect fake tracks was also negligible.

The number of uncorrelated particle trajectories were measured using "random" (uncorrelated oscillator) triggers. In order to determine this background, a measurement was performed with the MWPC-based tracking system in fully efficient configuration ($U_{SW} = 1{,}700\,V$) and vertical chamber position. This measurement was triggered by an oscillator, running at a frequency of 110 Hz. The measured data contains the reconstructed tracks, and allows the estimation of the "background" flux $f_{BG}$. The flux of true particles, $f$ was also measured, and calculated with the procedure described in Sec. 6.1 and in Ref. [OL08]. The $f$ is proportional to the number of observed tracks per event [OL01]:

$$f \propto \frac{N}{t} = \frac{N}{N_{trig}} \frac{N_{trig}}{t} = \frac{N}{N_{trig}} R_{trig} \ , \tag{30}$$

where the number of tracks $N$ are measured over time of $t$, whereas the number of triggered events $N_{trig}$ during the same time is the trigger rate $R_{trig}$. The background tracks $N_{BG}$ add up to the "true" track set, and therefore

$$f_{BG} \propto \frac{N_{BG}}{N_{trig}} R_{trig} \ . \tag{31}$$

The background flux, $f_{BG}$ (*filled circles*) is shown in Fig. 64. A clear minimum of the background flux is observed at the horizon, where it reaches the value of $2 \times 10^{-4}$ $\mathrm{m^{-2}sr^{-1}s^{-1}}$. The background flux is four orders of magnitude lower ($2.2 \times 10^{-4}$) than true measured flux, marked with *empty squares*. Note that the measured flux includes the low-energy physical background as well. The similar shape of measured and background fluxes suggests that, most of these background tracks are originated from the random coincidence, which is caused by the physical particles.

The final conclusion is that, there is no instrumentation background beyond the flux of physical tracks originated from random triggered measurements ($f_{BG}$) due to finite time resolution of the detector system.

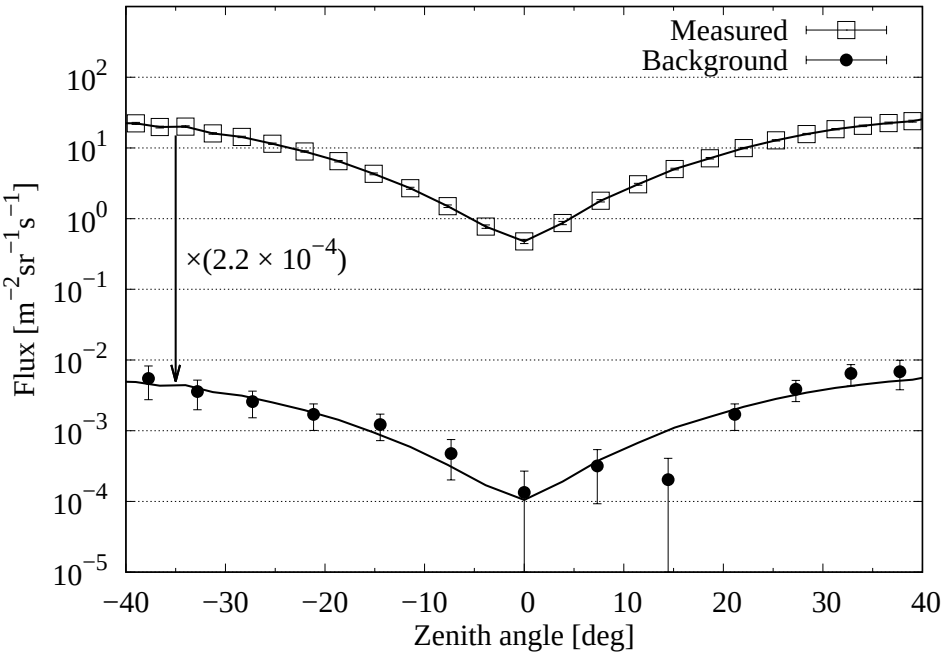


Figure 64: The background flux, $f_{BG}$ was found to be nearly four orders of magnitude below the $f$ flux of physical particles. Both fluxes have similar shape (indicated with the continuous lines) with clear minimums at the horizontal direction [OL01].

## 5.7 The suppression of physical background noise

As presented in Sec. 4.4, the end of the energy spectrum of the physical background noise is observed below the energy of 1 GeV [81]. This section focuses on the optimisation of the MWPC-based tracking system to suppress the physical background noise.

In the MWPC-based tracking system, the absorber layers are applied to deflect the trajectories of particles, as discussed in Sec. 5.1. The deflection in an absorber depends on the momentum (kinetic energy of relativistic particle) and the thickness of the absorber layer, as it is described by Eq. (18). With the precise measurement of the deflection of particles, the low-energy background particles can be suppressed. The angular resolution depends on the position resolution of detector layers, the number of tracking layers, and the total length of the tracking system. The aim of this study was to suggest the optimal spacing between detector layers and an absorber configuration for the MWPC-based tracking system to suppress the electrons and muons below the energy threshold of 1 GeV.

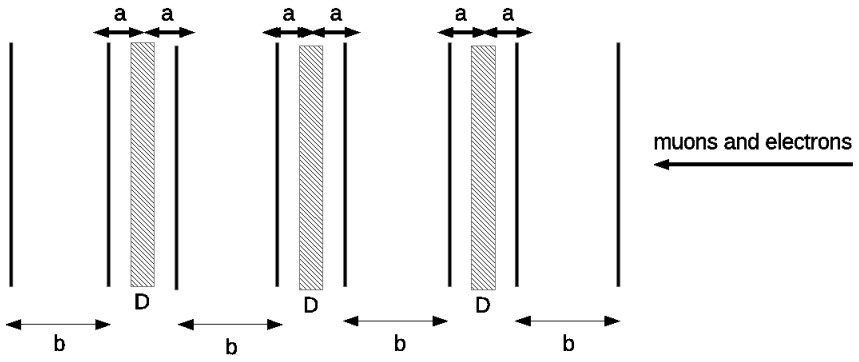


Figure 65: The scheme of the tracking system with 8 MWPCs (*black lines*) and 3 lead absorbers (*filled rectangles*) which was optimised by GEANT4 simulation.

For this study, I applied the GEANT4 simulation framework. A tracking system consists of eight MWPCs and three lead absorbers was constructed in the simulation, as shown in Fig. 65. Muons and electrons were generated in the energy range 0.2 GeV - 10 GeV, and injected horizontally across the tracking system. The standard GEANT4 electromagnetic processes were included in the simulation to take into account the interaction of particles with the detector [97, 98]. Both of primary and secondary particles were tracked with

their energy and spatial coordinates in the detectors. These parameters were written as ASCII files on event-by-event. The simulations were run with different chamber distances, $b = 30\,cm$, $b = 50\,cm$, and with different absorber thicknesses, $D = 2\,cm$, $D = 3\,cm$. The distances between the absorbers and the tracking layers were fixed to 5 cm.

The simulated data were analysed with the following procedures:

(i) Cluster formation: To take into account the position resolution of the MWPCs, the positions of the generated particles were shifted with a random number generated by Gaussian distribution with the sigma value of 4 mm. Each particle position was converted to half-integers, and those were defined as clsuter centroids.

(ii) Track reconstruction: The trajectories of simulated particles were reconstructed with different $\chi^2$/NDF cut values (2,3,4).

(iii) Calculation of the survival probabilities: It was the ration of the number of particles below the $\chi^2$/NDF threshold to the number of generated particles.

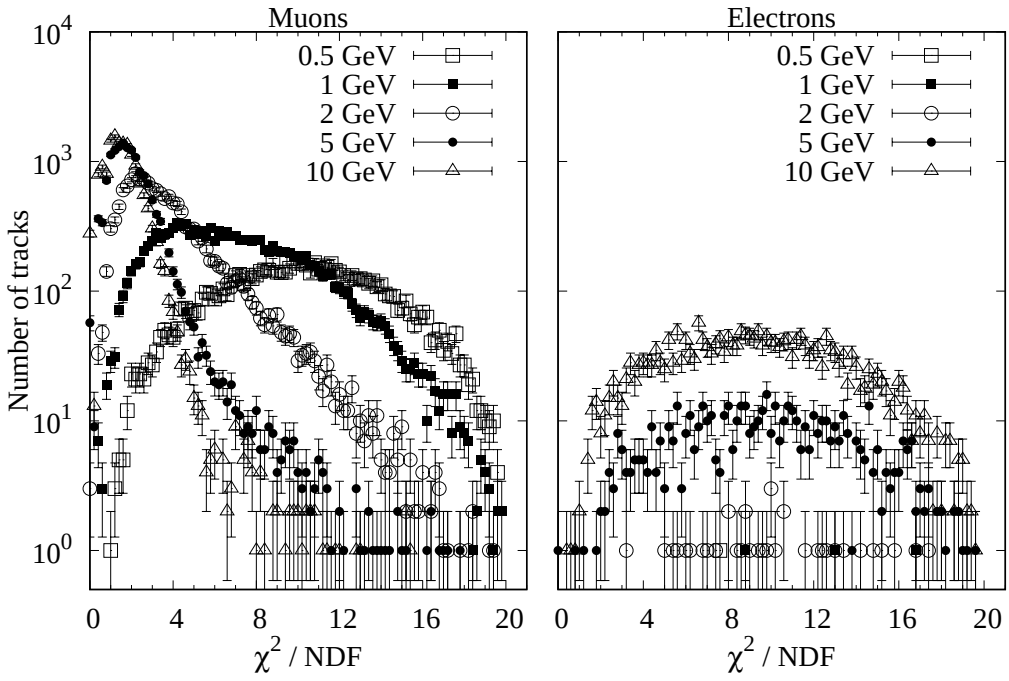


Figure 66: The distribution of $\chi^2$/NDF of simulated muons (*left*) and electrons (*right*) inside the MWPC-based tracking system. The low-energy particles scattered more through the absorbers, and the $\chi^2$/NDF distributions broadened to higher values.

Figure 66 shows an example for the distribution of $\chi^2$/NDF values of the tracks produced by the simulated muons (*left*) and electrons (*right*), detected by a tracker with b = 50 cm and D = 3 cm. As it was expected, the low-energy particles scattered more, and the $\chi^2$/NDF distributions broadened to higher values. The electrons lost most of their kinetic energy via bremsstrahlung, and stopped in the absorbers. The high-energy electrons suffered higher deflections than the muons. Consequently, the electrons produce broader $\chi^2$/NDF distributions.

The *upper panel* of Fig. 67 shows the survival probabilities of the particles as a function of their energy for different detector configurations. The *empty circles* shows a detector configuration with chamber spacing of 50 cm, total length of 2.4 m, and total absorber thickness of 9 cm. This configuration can efficiently suppress the muons and electrons below the energy of 1 GeV. Here the survival probability of electrons is observed to zero below the energy of 1 GeV, and it is found to be well below 2 % above the energy of 1 GeV. In case of the muons, the survival probability is found to be below 10 % at the energy threshold of 1 GeV. Note that these probabilities should be convoluted with the energy spectra of particles to calculate the fluxes.

This suppression level of the physical background noise is comparable with the suppression levels of other detector systems operated at volcanoes. For example, the *lower panel* of Fig. 67 shows the survival probabilities as a function of energy for different nuclear emulsion detectors. It is plotted for a system consists of 20 Emulsion Cloud Chambers with the *solid lines* and for a quartet detector consists of 4 tracking layers with *dashed lines*. Both trackers were applied for the investigation of Mt. Showa-Shinzano lava dome by R. Nishiyama *et al* [81].

To conclude, the presented simulation study suggests that, the application of a detector system consists of eight chambers with the total length of about 2.4 m and with 3 × 3 cm absorber layers to suppress the physical background noise down to 10 % level at the threshold energy of 1 GeV. These results demonstrated that, the tracking systems based on the new variant of MWPC detectors in this geometrical setup can suppress sufficiently the physical background noise. The next step will be the experimental optimisation and the comparison with the simulations.

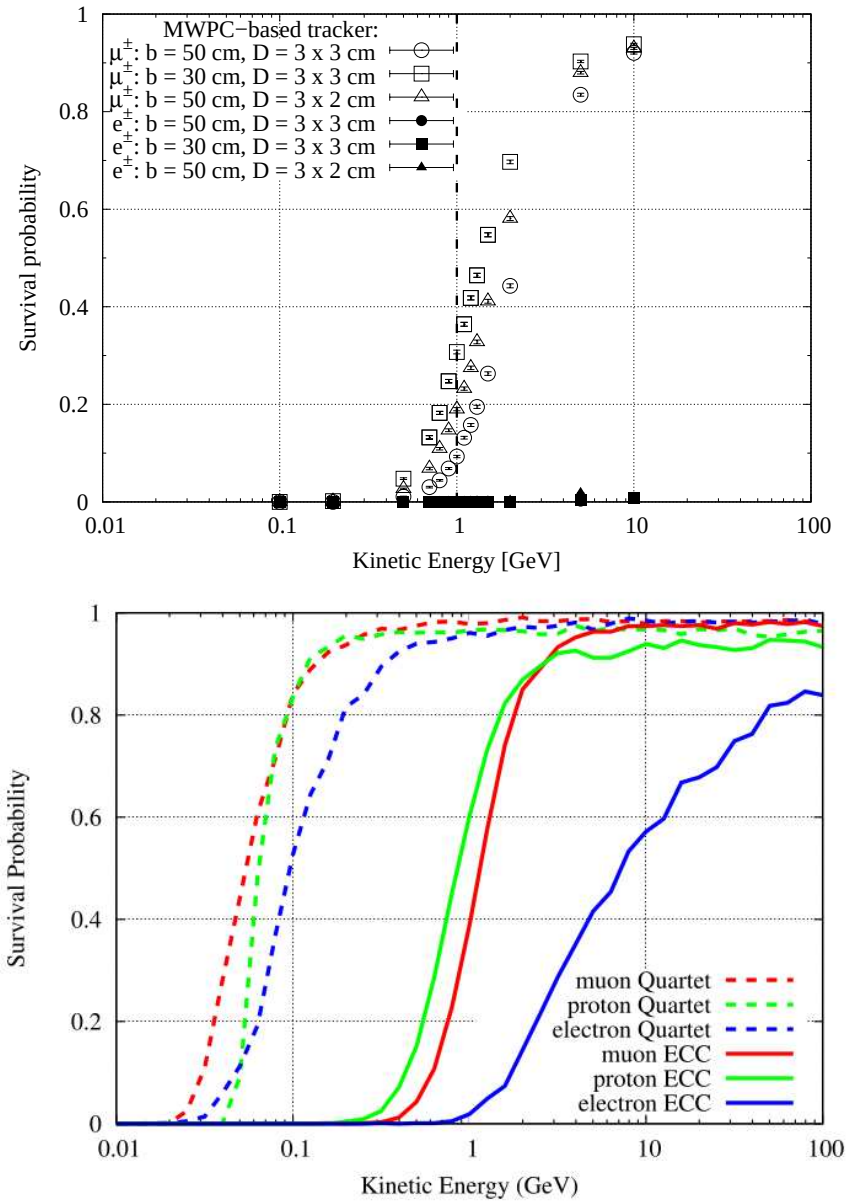


Figure 67: The *upper panel* shows the survival probabilities with $\chi^2$/NDF cut value of 3 for muons (*empty markers*) and electrons (*filled markers*) as the function of their kinetic energy for the MWPC-based system with different chamber spacing (b) and with different amount of absorbers (D). An optimised gaseous tracker with the total length of 2.4 m and 3 absorbers with the thickness of 3 cm can suppress more than the 90 % of the muons, and more than the 99.9 % of the electrons below the threshold energy of 1 GeV. This result is comparable with suppression level of other detector systems, such as with nuclear emulsion detectors developed for muography by R. Nishiyama, shown in the *lower panel* [81].

## 5.8 Experience with outdoor conditions

The tracking systems applied for muography should be optimised for the operation in outdoor conditions. In case of the CCC-based tracking system, the measurements are mostly performed at underground, where the change of weather did not influence the measurements and the environmental parameters (temperature, humidity, and pressure) were stable.

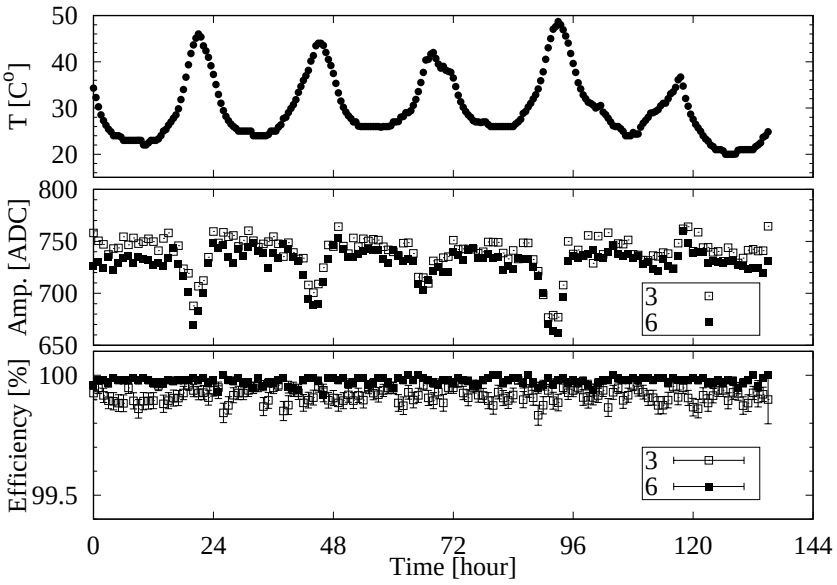


Figure 68: Time dependence of the relevant operational parameters during the six days of data taking in outdoor conditions. The temperature variations up to 30 °C were sustained (*upper panel*), with not more than 10 % mean amplitude changes due to partial compensation of the anode HV (*middle panel*). The tracking efficiency was consistently high, shown in the *lower panel*, during the whole period [OL01].

The MWPC-based tracking system was installed on the flat roof of a laboratory at the campus of Wigner RCP to test it under ambient outdoor conditions, as shown in the *right panel* of Fig. 44. The tracking system was covered only with a plastic box, thus it was influenced by the environmental conditions, e. g. received strong sunlight. The environmental parameters were also measured during data taking. The *top panel* of Fig. 68 shows the outer temperature. This shows about 30 °C daily temperature variations. The weather was clear during the data taking, except on the $5^{\text{th}}$ day, when it was rainy.

The 30 °C change of the temperature corresponds to nearly 10 % change of absolute temperature, and thus in the gas density. Therefore, the compensation of the sense wire

voltage is necessary to ensure stable measurements. This high voltage was compensated by a temperature dependent resistor, which was added to the high voltage power supply. Thereafter, the high voltage on the sense wires was reduced by 1 V at 1 °C temperature increase (from the nominal 1,700 V at 25 °C). The application of the compensation resulted that only a slight, 10 % mean amplitude variation was observed, as shown in the *middle panel* of Fig. 68. As it is described above, the key figure of merit for the detector is the tracking efficiency, shown in the *lower panel* of Fig. 68. The measured tracking efficiency was sufficiently high ($> 99.5\,\%$) and stable during the measurement period in the third (3) and sixth (6) tracking layers, and found consistently for all other chambers.

The detector was operated with a 2 L/h gas flow during the whole measurement period. An interesting issue was arisen due to the decrease of the temperature. The total tracking system gas volume was about 100 L. When the temperature decreased with about 6 °C in one hour, that was a $2\,\%$ relative change in absolute temperature, it reduced the total gas amount by about 2 L. In this case, the air was sucked from the outside atmosphere into the last chamber. In order to avoid this issue, a long buffer tube was connected after the last detector with a sufficiently large volume of about 2 L.

## 5.9 Summary and discussion about R&D of tracking detectors

In this chapter, I presented two gaseous detector systems, which were specifically developed for cosmic muon tracking: a CCC-based tracker for underground muography, and the first prototype of a MWPC-based system for imaging by the tracking of near-horizontal muons under open sky. I developed these tracking systems within the REGARD group and my contributions are summarised in the following points.

(i) Based on the design of the REGARD group, I constructed the CCC chambers and contributed to the construction of the MWPCs.

(ii) Based on the design of the REGARD group, I built, tested, and applied the power and data acquisition systems in both tracking systems.

(iii) I developed a data analysis software, which is applicable for performance studies, and analysis of measurements with the aim of imaging.

(iv) I quantified and optimised experimentally the performance of the developed tracking systems.

Based on Table. 2, one can compare the main technical parameters of the developed tracking systems with the other trackers applied for muon radiography in the recent years, presented in Sec 4.5. The developed tracking systems are promising candidates for comic muon imaging with their portability, modularity, low power consumption, good position and angular resolutions, reasonable data readout time, excellent detection efficiency, and negligible instrumental background noise of $2.2 \times 10^{-4}$. To suppress the low-energy physical background noise, the total detector length of 2.4 m and $3 \times 3$ cm of lead absorbers were proposed for the MWPC-based tracking system by Monte Carlo simulations.

| Technology | Size [$m^2$] | Weight [kg] | Power [W] | Position res. [mm] | Angular res. [mrad] | Refs. |
|---|---|---|---|---|---|---|
| Scintillator | 2 | 509 | $>30$ | 100 | 33 | [63] |
| Scintillator | 0.64 | 200 | 50 | 35 | 35 | [83, 84] |
| ECC | 0.4 | ? | 0 | 0.001 | 30 | [80, 87] |
| Emulsion | 2.45 | 250 | 0 | 0.001 | 15 | [88] |
| GRPC | 1 | ? | $>60$ | 4 | 4 | [90] |
| Micromegas | 0.25 | $<100$ | 35 | 0.2 | $<1$ | [91, 92] |
| **CCC** | **0.12** | **15** | **6** | **1.5** | **15** | **[OL08] - [OL11]** |
| **MWPC** | **0.58** | **80** | **6** | **4** | **15** | **[OL01, OL12]** |

Table 2: The comparison of the technical parameters of muon trackers which are used for muography from recent years: the detector technology, size of sensitive area, weight of sensitive detectors without absorbers, power consumption, position and angular resolution. Unknown data are signed with question marks.

The developed gaseous tracking systems with the technical details, the performances, and the applications were published in Refs. [OL01, OL08, OL09, OL10, OL11]. Furthermore, the MWPC-based tracking system was protected as a part of an intellectual property with the name of "Muographic Observation System" under the Ref. No. 2016-087436 (PTZTA153) in Japan [OL12].

# 6 Underground muography with gaseous detectors

Present chapter focuses on the applications of the CCC-based tracking systems at shallow depths underground. The aim was to demonstrate that the portable muon telescopes operate reliably during long measurement periods, measure precisely the flux of cosmic muons, and applicable to detect underground rock densifications or caverns.

In this chapter, I present the developed analysis method, the muon flux measurements in artificial tunnel systems, and their possible applications.

## 6.1 Calculation of muon flux

The muon flux was calculated by the offline data analysis. It uses HEP analysis methods which is presented in Sec. 5.4. The event-by-event analysis initiates by cluster reconstruction on each layer. Thereafter, the combinatorial tracking algorithm reconstructs the trajectories of the detected particles.

After the track selection, the direction dependent flux, $F(m_x, m_y)$ is calculated in $\mathrm{m}^{-2}\mathrm{sr}^{-1}\mathrm{s}^{-1}$ units with the following equation [OL08]:

$$F(m_x, m_y) = \frac{\mathrm{d}N_{tracks}}{\mathrm{d}A\,\mathrm{d}\Omega\,\mathrm{d}t\,\mathrm{d}\epsilon_{tracking}} \left[\mathrm{m}^{-2}\mathrm{sr}^{-1}\mathrm{s}^{-1}\right] \quad , \tag{32}$$

where $\mathrm{d}N_{track}$ is the number of reconstructed tracks, $\mathrm{d}A$ is the surface element in the observation direction, $\mathrm{d}\Omega = \mathrm{d}m_x\mathrm{d}m_y/(m_x + m_y + 1)^{3/2}$ is the differential solid angle, $\mathrm{d}t$ is time of data taking and $\mathrm{d}\epsilon_{tracking}$ is the direction dependent tracking efficiency calculated with Eq. (29) in each direction. Figure 69 shows the muon flux and the direction dependent detector parameters as a function of the track projections, $m_x$ and $m_y$, for a data set measured in the laboratory of Wigner RCP.

To calculate $\mathrm{d}N_{track}$, the following track selection cuts are applied:

- The cuts on the number of cluster per layer, $N_{clusters/layer}$, and the length of clusters, $L_{cluster}$ are applied to exclude the noisy events, which cause fake tracks: $N_{clusters/layer} < 6$ and $L_{cluster} < 7$. These cuts result in negligible ($<1\,\%$) decrease on the flux in normal detector operation.

- A cut is applied on the goodness of the fit to exclude the low-energy electrons which deflected in the material of the detector: $\chi^2/\mathrm{NDF} < 3$. This cut results less than 1 % decrease for the flux at underground[5].
- The number of tracks per event, $N_{tracks/event}$ equals to 1 : $N_{tracks/event} = 1$. This causes a small decrease ($\sim 1\,\%$) for the flux at underground measurements.

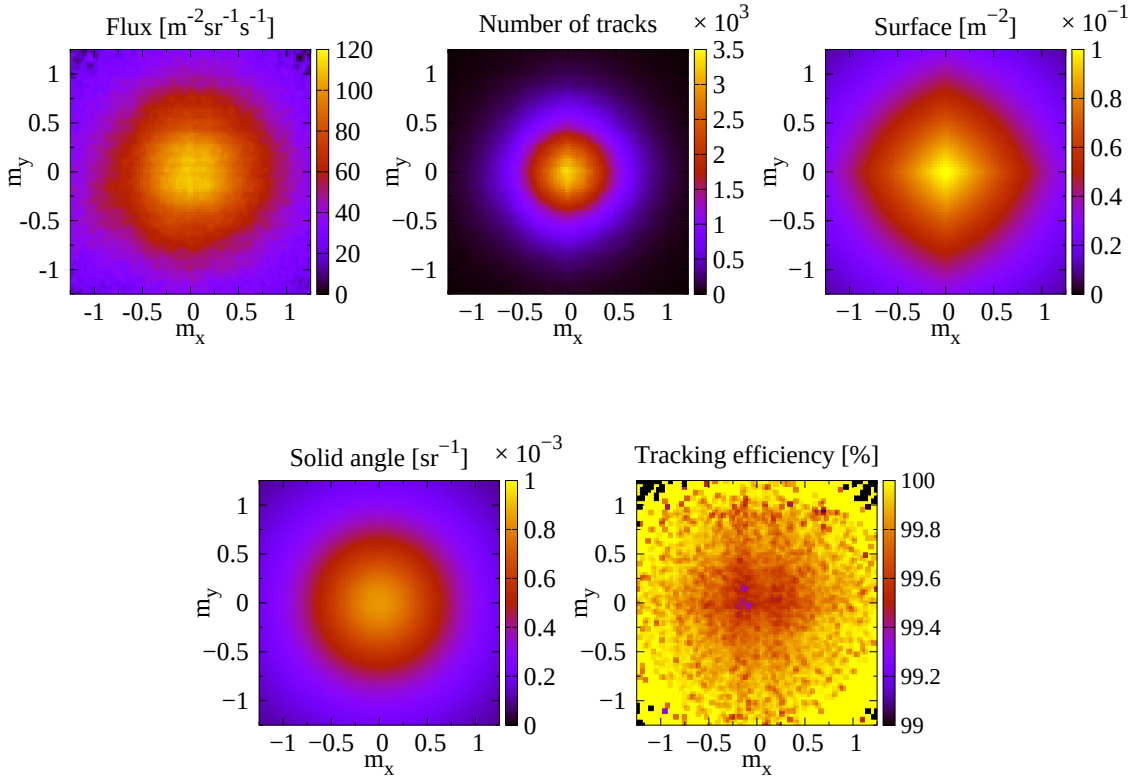


Figure 69: The flux (*upper left*) was calculated by Eq. (32) with the following direction dependent parameters: number of tracks (*upper middle*), effective detector surface (*upper right*), solid angle (*lower left*) and tracking efficiency (*lower right*).

The duration of data readout, the so-called dead time causes a systematical effect on the flux. This dead time is subtracted from the time of data taking on event-by-event basis. For the first prototype the dead time per event was 9.8 ms, which results a correction of 18 % under open sky, 7 % at the depth of 10 m, 2 % at the depth of 30 m. For the new

[5]Note that the soft component of cosmic rays is totally absorbed in the first 1-2 m of soil above the detector, the detected electrons are created mostly by the ionisation of the muons.

Raspberry Pi operated DAQ the dead time is 400 $\mu$s, thus the correction is about 0.6 % under open sky and even less underground.

Measurements were performed in different rotated and tilted detector positions to investigate that the calculated fluxes were in agreement at a given direction. Figure 70 shows the muon flux for different tilted measurements, where the flux values agree within statistical errors. The muon fluxes with rotated detector positions are also in agreement as it was presented in Refs. [OL08] and [99].

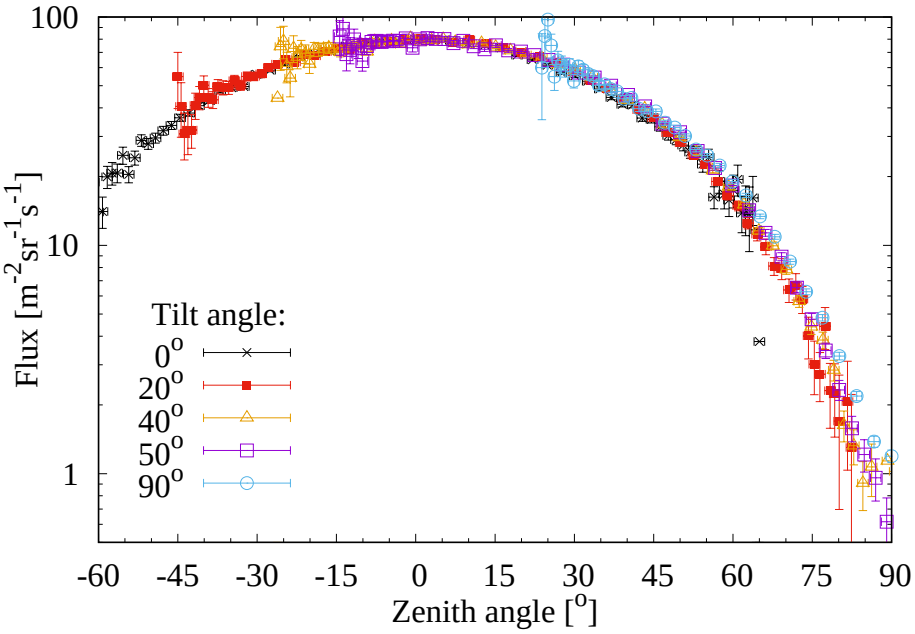


Figure 70: The muon flux as a function of zenith angle in vertical and different tilted detector positions. For each of the measurements, the flux values under the same zenith angle are in agreement within statistical errors.

## 6.2 Muon flux measurements in artificial tunnels

Present section focuses on the muon flux measurements performed in artificial tunnels. The aim of these measurements was to demonstrate that the developed portable muon telescope measures properly the flux of cosmic muons. Measurements were performed in the Jánossy pit at the campus of the Wigner RCP and in Felsenkeller, Dresden, Germany at different depth down to 50 meter-rock-equivalent depth. More details are provided about the measurement sites in Sec. 6.3 and in Sec. 6.4.

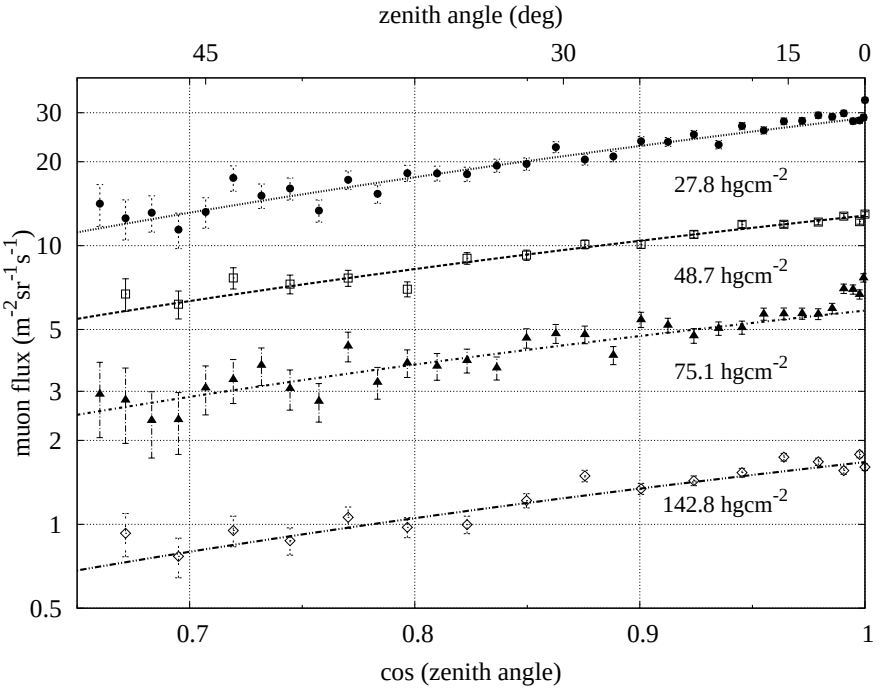


Figure 71: The muon flux were measured up to 55° at four different depth [OL15]. *Black curves* shown the fitted functions (see more in the text).

To compare the measured fluxes with earlier results, the middle slices from the fluxes were extracted and were fitted with the following function [OL15]:

$$F(\theta) = F(0)\cos^n(\theta) \ , \tag{33}$$

where $F(0)$ is the vertical flux and $n$ is the exponent of $\cos(\theta)$, $\theta$ is the zenith angle. Figure 71 shows the muon fluxes up to 55° with the corresponding statistical errors (3 - 8 %) as a function of zenith angle. The main parameters of the measurements (place and depth of the measurement, time of data taking, number of detected tracks) and the fit parameter values are shown in Tab. 3. Note that the depth of 1 hg/cm$^2$ is equal to 1 meter-water-equivalent depth and the density-length of the atmosphere is 10.3 hg/cm$^2$.

The fit parameters were compared to the results of the earlier measurements. Figure 72 shows the vertical flux as a function of depth from the top of the atmosphere. The vertical fluxes measured by the developed muon telescope (*red triangles*) are in good agreement with the empirical curve [100], and are consistent with the earlier measurements [101, 102, 103, 104, 105, 106, 107, 108, 109, 110, 111, 112].

| Place | Depth [m] | Density-length [hg/cm$^2$] | Time [day] | Muon tracks $\times 10^3$ | $F(0)$ [m$^{-2}$ sr$^{-1}$ s$^{-1}$] | $n$ |
|---|---|---|---|---|---|---|
| Jánossy pit | 10 | 27.8 ± 1.5 | 5 | 1,200 | 28.72 ± 0.74 | 2.19 ± 0.17 |
| Jánossy pit | 20 | 48.7 ± 3.2 | 7 | 550 | 12.45 ± 0.29 | 2.11 ± 0.16 |
| Jánossy pit | 30 | 75.1 ± 5.4 | 11.5 | 472 | 5.85 ± 0.22 | 2.00 ± 0.24 |
| Felsenkeller | 50 | 130.3 ± 10 | 20 | 217 | 1.77 ± 0.07 | 2.21 ± 0.27 |

Table 3: The summary of the measurements performed at shallow depth underground with the time of data taking, the number of detected muon tracks, and the results [OL15].

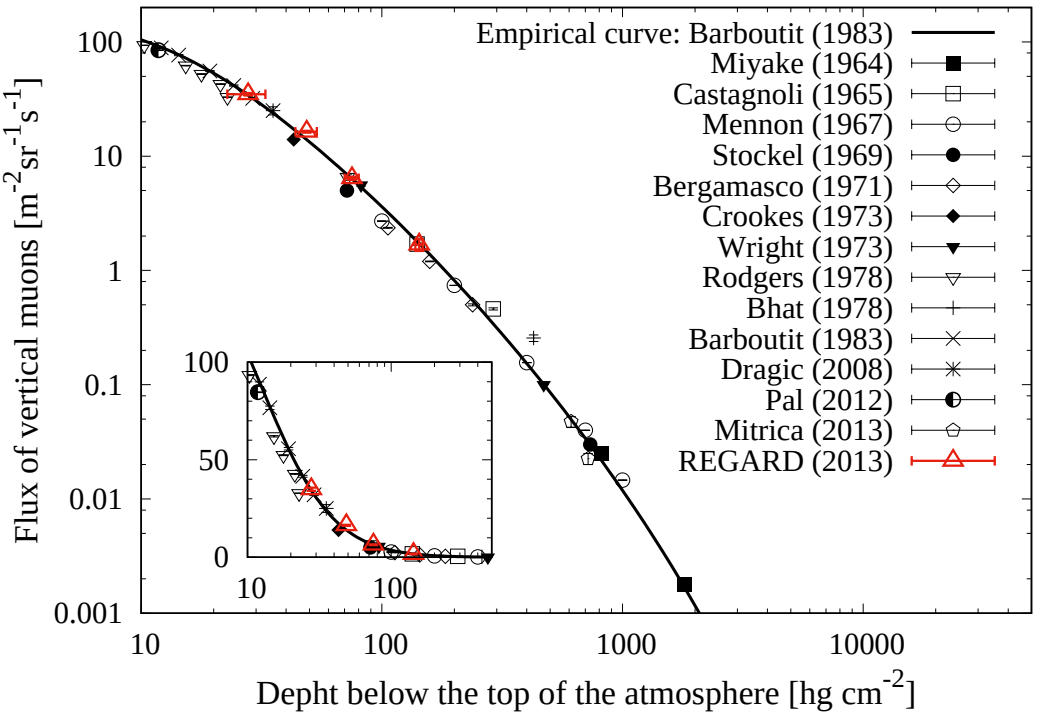


Figure 72: The flux of vertical muons is plotted as a function of depth from the top of the atmosphere in units of hg/cm$^2$. The vertical muon flux values measured by the muon telescope (*red triangles*) agree with the empirical curve (*continuous line*) and are consistent with the results of earlier measurements (*black dots*).

The $n$ exponents (*red triangles*) are plotted as a function of depth from the top of the atmosphere in Fig. 73. These are also in good agreement with the results of the earlier measurements presented in Refs. [101, 102, 104, 106, 109, 111, 113].

From the presented results one can conclude that the developed tracking system measure reliably the flux of cosmic muons at shallow depth underground.

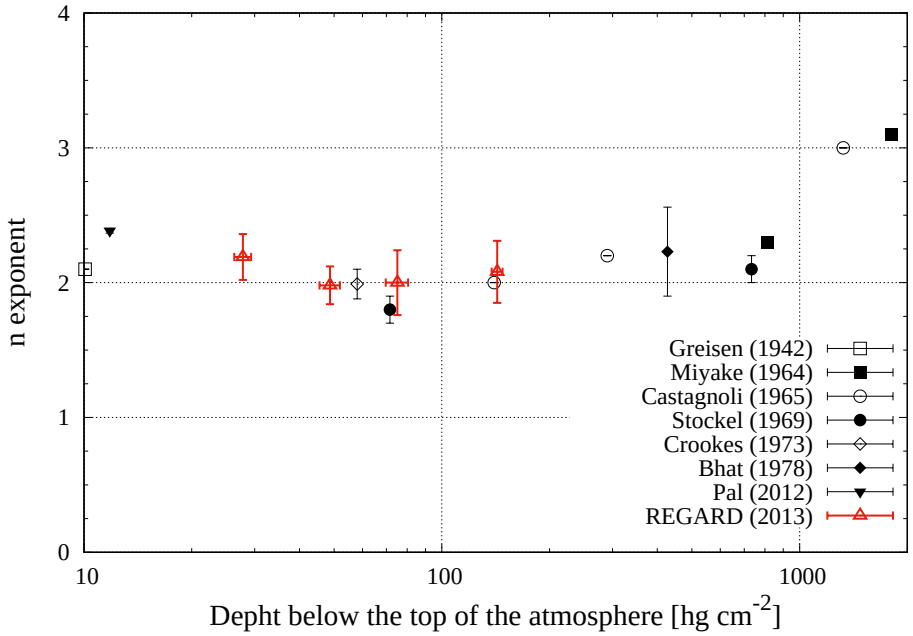


Figure 73: The exponent values of the measured muon fluxes as a function of depth from the top of the atmosphere in units of hg/cm$^2$. The measured exponent values (*red triangles*) are consistent with the results of earlier measurements (*black dots*).

## 6.3 Cosmic background measurements of proposed experiments

The first application of muon flux measurements was at a proposed place of a future underground laboratory at Felsenkeller Dresden Germany. Here nuclear astrophysical processes will be investigated by an accelerator-based experiment [114]. The aim of the muon flux measurements was to determine the cosmic background of the proposed experiments and to find the best location for the detectors where the cosmic background is minimal. Figure 74 shows the schematic of the tunnels in Felsenkeller [114]. The detector was deployed at the end of Tunnel IX at the proposed place of the Pelletron.

Multiple-directional measurements were performed at a fixed detector position at the depth of about 50 m between the 12$^{\text{th}}$ February and the 27$^{\text{th}}$ March in 2013 [OL13, OL14]. In vertical position, the detector was oriented to 350° relative to the Magnetic North. The muon flux were also measured in 45° (relative to the vertical direction) tilted detector position to the directions of 350°, 80°, 170°, 260°, and 305°. These measurements covered almost the full $2\pi$ solid angle of the upper hemisphere. More details about the parameters of the measurements can be found in Ref. [OL13].

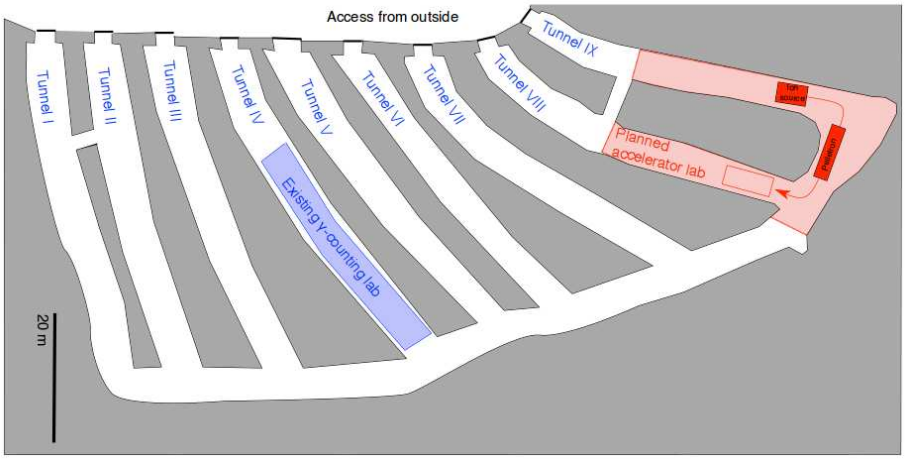


Figure 74: The schematic view of the proposed site for the accelerator-based experiments inside Felsenkeller, Dresden, Germany [114]. The muon flux measurements were performed at the end of Tunnel IX at the proposed place of the Pelletron.

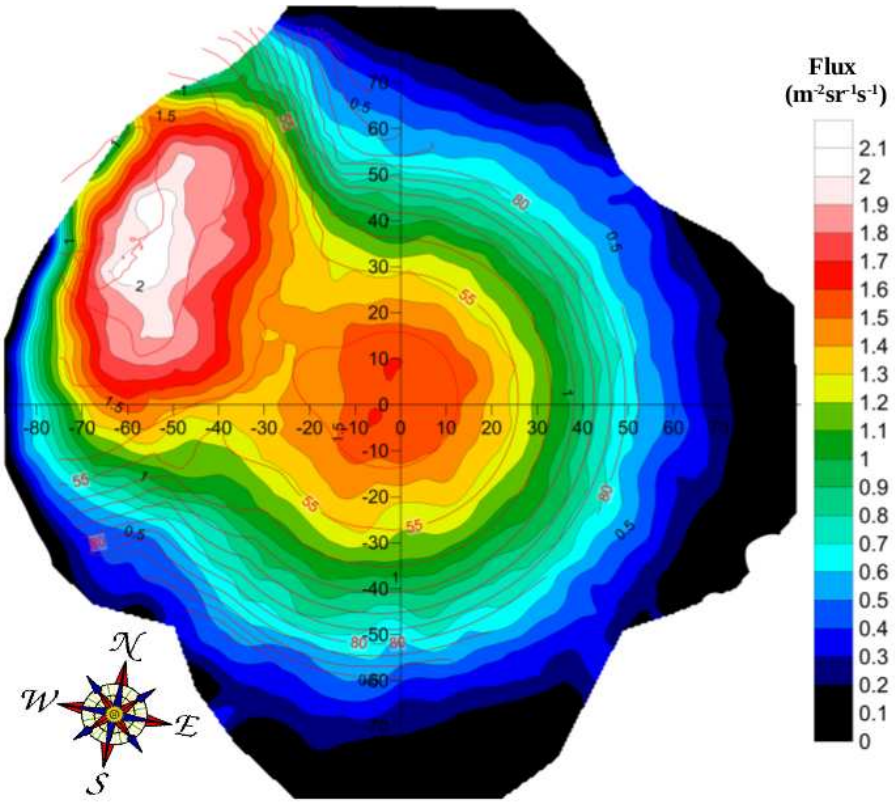


Figure 75: The flux of cosmic muons (*colour-scale contours*) was merged from six different measurements at the place of the proposed accelerator-based experiment. The detector was oriented to 350° to the Magnetic North [OL13, OL14].

The muon telescope operated reliably during the 39 days of data taking and 477,000 tracks were collected all together [OL13]. The flux of muons was calculated with the precision of $70 \times 70$ mrad$^2$ which resulted the statistical error from 3 % to 10 %. The soil thickness above the measurement location was also determined by geodetic measurements performed by the MTA-ELTE Geological, Geophysical and Space Sciences Research Group.

Figure 75 shows together the flux of cosmic muons in units of $m^{-2}sr^{-1}s^{-1}$ (*color-scale contours*) and the calculated soil thicknesses (*red contour lines*) as a function of zenith and azimuth angles. As it was expected, the measured muon flux correlated well with the overburden rock thickness: the colour scaling and the red contours were mainly parallel to each other. The maximum muon flux was found to be below 2.5 $m^{-2}sr^{-1}s^{-1}$. The highest fluxes were measured in the direction of the zenith and the entrance of the tunnel to west. The obtained flux map provides a well defined baseline for the calculation of total background of the proposed accelerator-based experiments in the Felsenkeller site and suggest the end of the Tunnel VIII for the location of the future detectors.

## 6.4 Muography of artificial underground tunnels

Present section focuses on the applicability of the developed portable detector system for muon radiography. Here, the aim is to demonstrate that the muon telescope can detect underground caverns via measurement of the flux of cosmic muons.

The first test measurements were performed at the depth of 60 m inside the Ajándék cave in the Ariadne natural cavern system in the Pilis mountains. The measurements with the total time of data taking of 50 days were demonstrated that the developed detectors can operate out of the laboratory during long-measurement period without continuous maintenance. Both the angular distribution of cosmic muons, and the rock thickness were calculated. No evidence were found for unknown caverns above the measurement point. More details are provided about this measurement campaign in Refs. [OL08] and [99].

Further test measurements were performed inside the Kőbánya tunnel system under Budapest. The tunnels are located from the depth of 10 m down to 30 m and the overburden soil has the average density of $1.8 \pm 0.1$ g/cm$^3$. The aim of the test measurements was to demonstrate that the developed muon telescope is applicable to detect underground tunnel structures. The main parameters of the measurements are summarised in Tab. 4.

| Place | Detector position | Depth [m] | Time [day] | Tracks $\times 10^3$ |
|---|---|---|---|---|
| Ariadne cavern system | Ajándék cave | 60 | 50 | 170 |
| Kőbánya tunnel system | **(a)**: exactly under a blow-hole | 12 | 7 | 330 |
| Kőbánya tunnel system | **(b)**: tilted with 15° under a blow-hole | 12 | 7 | 225 |
| Kőbánya tunnel system | **(c)**: next to a wall | 12 | 6 | 220 |
| Kőbánya tunnel system | **(d)**: 2 meters far from a blow-hole | 17 | 6 | 130 |

Table 4: The summary table of the test measurements performed in the Ariadne cavern system and Kőbánya tunnel system with the main parameters.

For each measurement, the angular distribution of cosmic muons was calculated with the precision of 70 × 70 mrad$^2$ using the cluster and track reconstruction algorithms presented in Sec. 5.4. Figure 76 shows the calculated angular distributions (*gray scale contours*) under vertical blow-hole in vertical (*a*) and in 15° tilted to the Magnetic North (*b*) detector positions, next to the wall of a tunnel (*c*) and close the blow-hole which vertical axis was 2 m away from the detector at the direction of 240° to the Magnetic North (*d*) [OL10]. The statistical errors for each of the angular contours are the square root of the values which result the relative error from 2 % up to 6 %.

Geodetic measurements were also performed by the MTA-ELTE Geological, Geophysical and Space Sciences Research Group to determine the soil thickness above the location of the measurement [OL10]. The calculated soil thicknesses are plotted with *red contour lines* in each (*a-d*) panel. The measured angular distributions correlate well with the calculated soil thickness in each panel of Fig. 76. The bright spots originate from particles arrived to the detector across the empty blow-hole. Note that the angular distributions at the white spots contain the electron component as well.

In case of Kőbánya tunnel system, the blow-holes connected to the surface of the Earth were shown in the measured angular distributions. Further measurements were performed inside the Jánossy pit. Here the aim was to demonstrate that the developed muon telescope can be applied for the detection of underground tunnels.

The Jánossy pit was an excellent place for that study because of its structure. Figure 77 shows the schematic view of the tunnel system. The Jánossy pit has three parallel levels under each other at the depths of 10 m, 20 m, and 30 m. At the first level there is one tunnel, *Tunnel 1* with the volume of $11 \times 2.5 \times 2.6\,\mathrm{m}^3$. At the second level, there are two tunnels in the opposite directions, *Tunnel 2a* and *Tunnel 2b* with the volume of $9.5 \times 2.5 \times 2.6\,\mathrm{m}^3$.

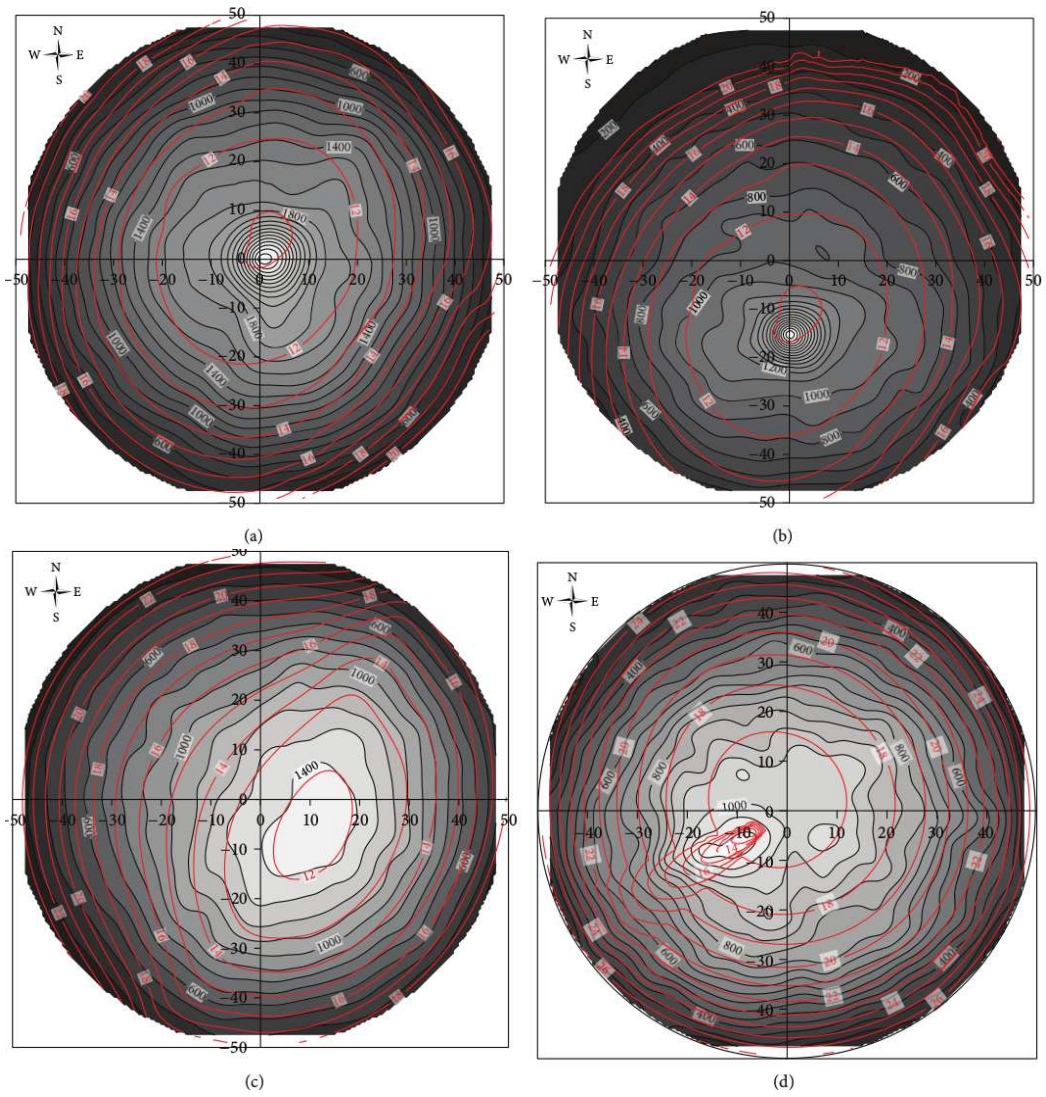


Figure 76: Measurements with the portable muon telescope performed at different places inside Kőbánya tunnel system: under a blow-hole (*a*), at the same place with 15° tilted detector to the Magnetic North (*b*), next to the wall of a tunnel (*c*) and blow-hole which vertical axis was 2 m away from the detector (*d*) [OL10]. *Gray scale contours* show the number of tracks divided by the detector acceptance and *red contour lines* show the depth in meter units which was determined by geodetic measurements.

Finally, at the third level there are three tunnels, the *Tunnel 3a* is located parallely under *Tunnel 1* and *Tunnel 2* with the volume of $23 \times 2.5 \times 2.6\,\mathrm{m}^3$, and two other tunnels with the orientation of $\pm$ 120° from *Tunnel 3a*. The soil density is $2.2 \pm 0.2\,\mathrm{g/cm}^3$. The thickness of the concrete ($\rho = 2.4\,\mathrm{g/cm}^3$) tunnel walls is about 1 m.

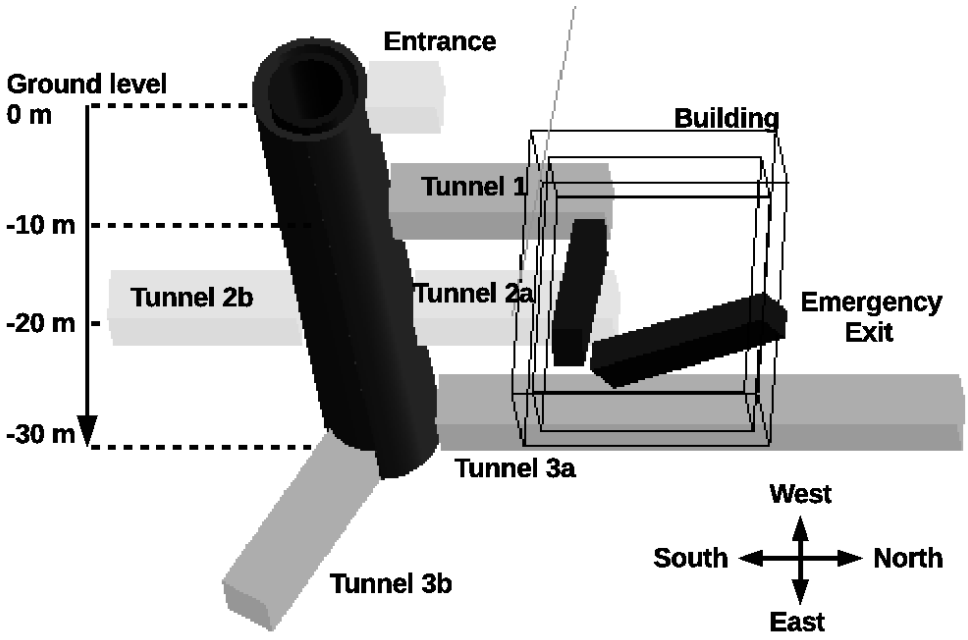


Figure 77: The schematic view of the Jánossy pit. It is a 30 m depth underground tunnel system with 3 levels at the depth of 10 m, 20 m and 30 m.

The geometry of the Jánossy pit was implemented into GEANT4 simulation with the above parameters. The expected muon flux was calculated by the following procedure. Muon beams were generated from the place of the detector inside the tunnel with uniform angular distribution and $N(E) \sim E^{-2.7}$ energy distribution. Above the Jánossy pit model, a screen was placed where the penetrated muons were recorded. From the minimum energy value, the density-lengths were calculated for each $35 \times 35$ mrad$^2$ size angular bin. From the density-lengths, the expected flux was calculated for each angular bin by an empirical formulae of vertical muon flux versus depth [100] and the combination of the angular distribution of cosmic muons with the exponent value of 2.

Figure 78 shows the expected (*left panels*) and measured (*right panels*) flux values, which are divided by $\cos^2(\theta_{x,y})$ normalisation, where $\theta_{x,y} = \arctan(m_x^2 + m_y^2)$. Specifically, the *upper panels* show the pit entrance dome of the tunnel system towards south and the nearby building edge at the northeast corner from the *Tunnel 1* at the depth of 10 m. In the *middle panels*, two parallel tunnels, *Tunnel 1* and *Tunnel 2a* are observed in the north-south orientation from the *Tunnel 3a* at the depth of 30 m. In the lower panels, a tunnel at the depth of 20 m, *Tunnel 2b*, is observed in the northeast – southwest orientation

from *Tunnel 3b*. The statistical errors are increasing with zenith angle from 3 % to 8 % for each measurement.

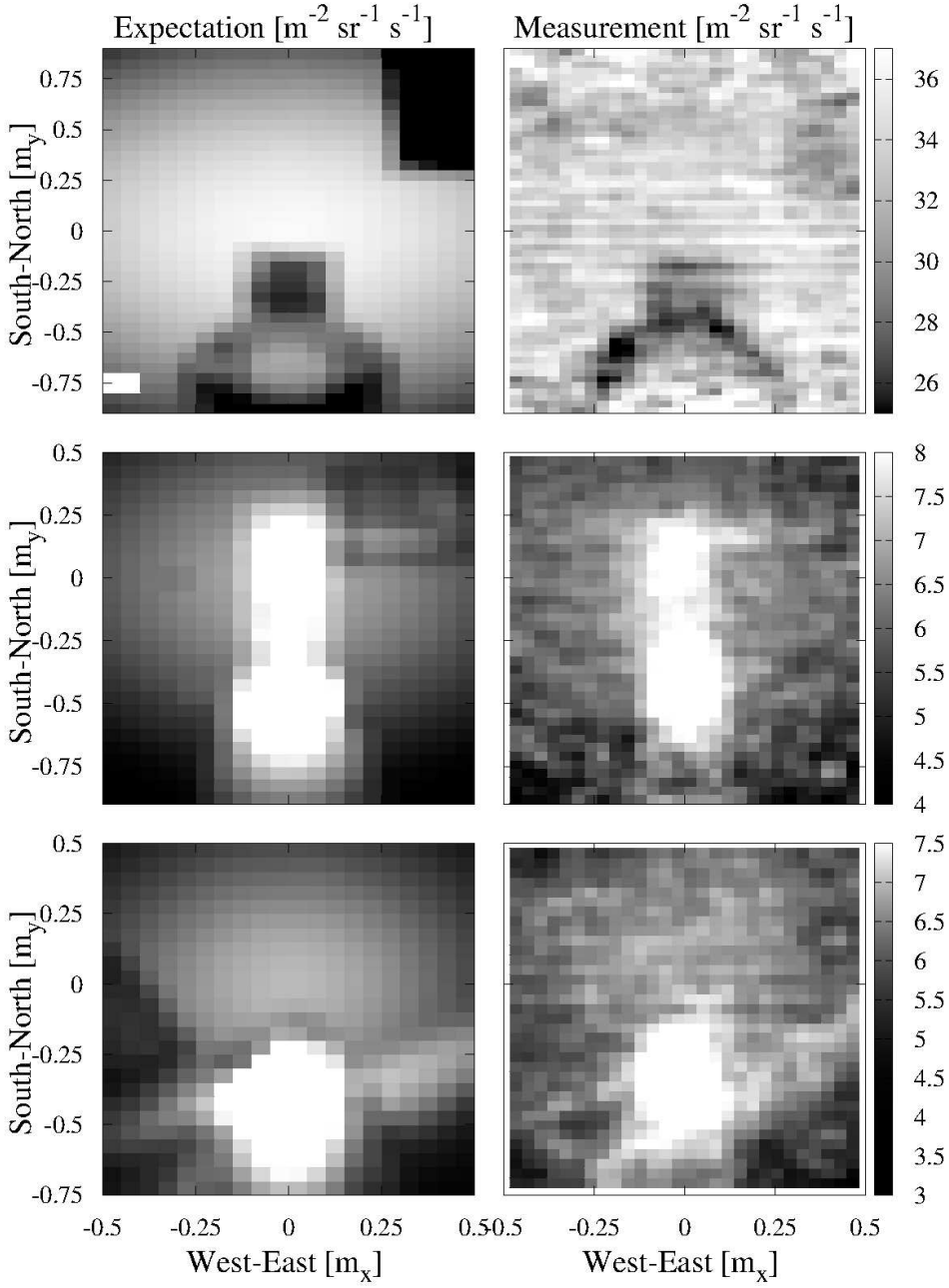


Figure 78: Muon flux measurements (*right panels*) were compared with the GEANT4 simulation (*left panels*): the tunnels and the building structures were well reproduced by the measurements [OL15, OL11]. *Grayscale* shows the flux values divided by $\cos^2(\theta_{x,y})$.

These results demonstrate that the developed tracking system is applicable to detect underground tunnels by the measurement of the flux of cosmic muons at the depth of 10-30 m with the data taking time of 1-2 weeks.

The above presented results demonstrated that the developed muon telescope sensitive to the effects of underground tunnel structures. Due to its small size and portability the detector itself can be applicable at inaccessible places under the urban area where it can provide useful information for urban planning or recultivation.

The next step was the demonstration of that the developed detector is applicable for detect hidden underground caverns. To explore the mountain above the Királylaki tunnel system, a measurement campaing was performed between the January of 2015 and August of 2016. Several measurements were performed at different locations inside the tunnel system with the data taking time of 1-4 weeks from the depth of 20 m to the depth of 100 m. The analysis of the measured data is still ongoing.

## 6.5 Calculation of the time of data taking

Present section focuses on the determination of the expected time of data taking to detect hidden caverns. Theoretical calculations were presented in Refs. [115, 116]. Here a Monte Carlo simulation-based study is also presented.

First of all, the time of data taking to measure the flux of vertical muons with different statistical uncertainties was calculated. Based on the vertical fluxes presented in Ref. [75], the measurement times were calculated for $70 \times 70$ mrad$^2$ angular bins at ten different depth. Figure 79 shows the calculated time of data taking which is necessary to measure the flux of vertical muons with the relative error of 3 % (*blue dots*), 5 % (*red dots*) and 10 % (*black dots*) as a function of depth in meter-standard-rock-equivalent units. Note that the lines are drawn to guide the eye. The time values on each curve are consistent with the time of the measurements performed in the Jánossy pit and Felsenkeller.

The flux of cosmic muon is maximal from the zenith direction. However, the detector is not always placed exactly under the investigated object and the measurement of the flux performed at different zenith angles is also necessary to detect underground caverns. Therefore, it is relevant to quantify the required time of data taking which is necessary to detect a given object, such as a cavern from a given depth with a vertically oriented detector.

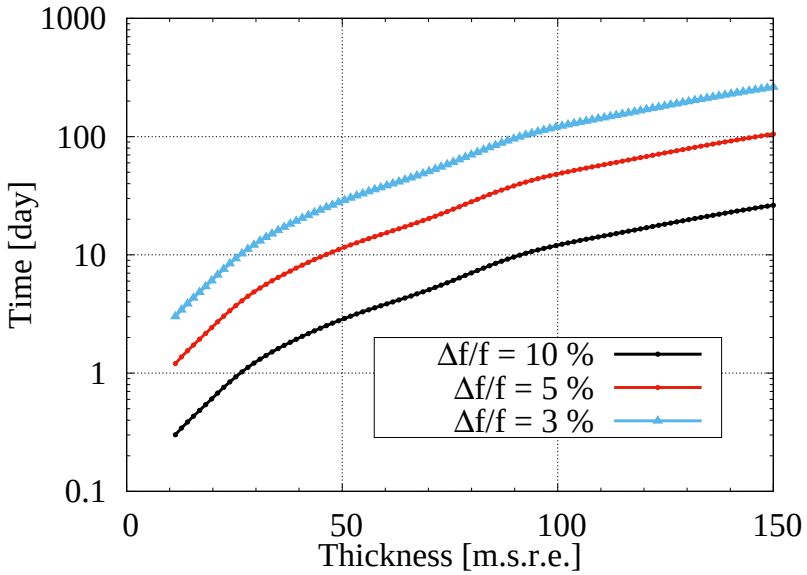


Figure 79: The expected time as a function of depth for measurement of vertical flux in 70 × 70 mrad$^2$ angular bins with the relative error of 3 % (*blue dots*), 5 % (*red dots*) and 10 % (*black dots*), respectively. Lines are drawn to guide the eye.

The muon flux $f(H)$ reduces as a function the depth $H$, therefore the change of $f(H)$ versus $H$ allows one to detect the underground rock inhomogeneities [115, 116]. Following the scheme in Fig. 80, for a $2R$ diameter cavern at the depth of $H$-$h$ the confidence level is proportional to the expected difference divided by the statistical uncertainty:

$$\frac{f(H-2R)-f(H)}{\sqrt{f(H-2R)}} \approx 2R\frac{\mathrm{d}}{\mathrm{d}H}\left[\sqrt{f(H)}\right] = 2\,R\,f^*(H)\ , \tag{34}$$

where $H \gg 2R$ is assumed. The ratio of the time of data taking at the zenith angle of $\theta$ ($t(\theta)$) to the same at the zenith angle of 0 ($t(0)$), to detect a cavern with the same confidence level is expressed by the following equation:

$$\frac{t(\theta)}{t(0)} = \frac{f^*(H)}{f^*(\frac{H}{\cos(\theta)})} \times \cos^{-2}(\theta) \times \cos^{-2}(\theta) \times A^{-1}(\theta)\ , \tag{35}$$

where, on the right side, the second factor is a reasonably good approximation of the angular distribution of cosmic muons, the third term is from the reduction of the angle of view if the cavern is located under the zenith angle of $\theta$. An additional detector geometry dependent factor, $A(\theta)$ determines detector acceptance relative to $\theta$ =0° [OL11].

The time of data taking as a function of zenith angle of cavern was quantified by

GEANT4 simulation. It simulates the penetration of atmospheric muons across a rock box with and without cavern, and includes all of the electromagnetic interactions [OL11]. The schematic view of the simulation is shown in Fig. 80.

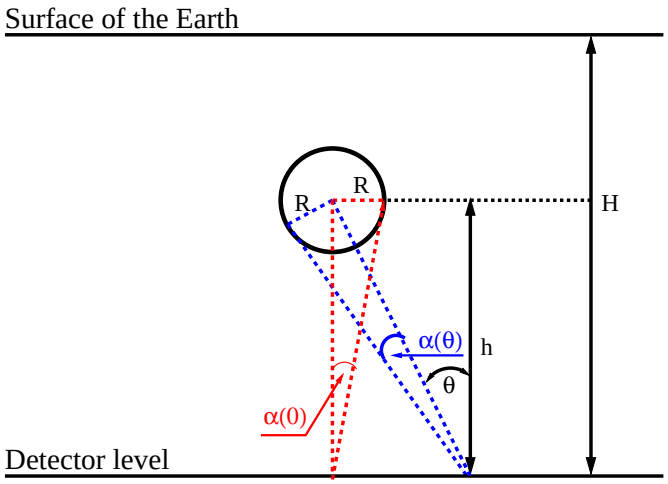


Figure 80: The 2-dimensional view of the geometry of the simulations [OL11].

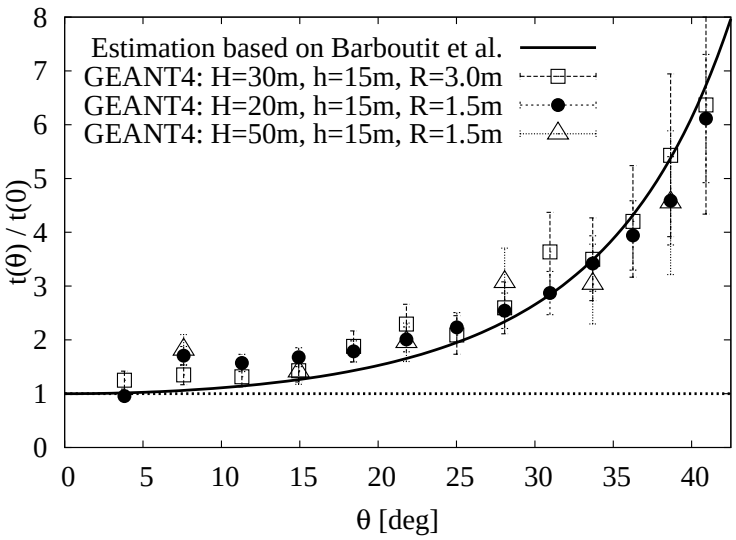


Figure 81: The relative time of the data taking required with a horizontal detector to detect a cavern with level of significance of $3\sigma$ (99.7 %) is plotted as a function of zenith angle ($\theta$) [OL11].

CRY cosmic ray generator provides the particle showers as the input for GEANT4 [117]. The muons were generated within a 100 × 100 $m^2$ area at sea level. Standard rock was implemented with different thickness, $H$ and with different cavern diameters, $R$ as well as without any cavern. For simplicity, a "flat" detector model was used with $A(\theta) = \cos(\theta)$. Note that this term can be set to $A(\theta) = 1$ if the detector is turned towards the object of interest. The time ratio of data taking to detect the cavern with $3\sigma$ (99.7 %) confidence level was calculated. Figure 81 shows the results of the GEANT4 simulation with different rock thicknesses, $H$ and cavern diameters, $R$ and the above detailed estimation which is used the muon flux versus density-length curve measured by Barboutit *et al.* [100]. Both the estimation and the simulation results show the same trend for different depths and cavern diameters. For example, the time of data taking to detect an underground cavern with $3\sigma$ confidence level is three times longer in the zenith angle of 30° than in case of the vertical direction [OL11].

## 6.6 Summary of underground measurements

In this section, I presented the underground measurements performed by the newly developed muon telescope. My contributions to the measurements and the data analysis are summarised as the follows.

(i) I measured the angular distribution and the flux of cosmic muons in Kőbánya tunnel system, Felsenkeller, and Jánossy pit at shallow depths (< 50 m.s.r.e.) with the newly developed muon telescope.

(ii) I verified that, the developed detector measures properly the flux of cosmic muons. I demonstrated that the portable tracking system is applicable to measure the cosmic background of future physics experiments.

(iii) I demonstrated that, artificial underground tunnels can be detected by the developed portable muon telescope. I calculated the relative time of data taking as a function of zenith angle to detect a cavern with $3\sigma$ (99.7 %) confidence level.

The presented methods and results were published in Refs. [OL08, OL09, OL10, OL11, OL13, OL14, OL15, OL16]. Furthermore, I presented these in talks at the 14$^{\text{th}}$ International Conference on Advanced Technology and Particle Physics and XXIV. European Cosmic Ray Symposium, as well as at MUOGRAPHERS2015 workshop as an invited speaker.

# 7 Imaging of low-$Z$ materials by muon tracking

The applicability of cosmic muon tracking for the inspection of high-$Z$ and large size objects was demonstrated in various applications. However, the imaging of low-$Z$ and small size materials could not be performed within a reasonable time by the measurement of the absorption and the scattering of cosmic muons. This chapter focuses on a novel approach developed to image low-$Z$ materials. This is based on a pioneering study performed in collaboration with the University of Novi Sad. We demonstrated that low-$Z$ materials can be imaged by the simultaneous detection of cosmic muons and photons created via bremsstrahlung inside the investigated sample [OL17].

Secondary photons are created by the following physical processes:

(i) **Bremstrahlung of electrons created by the ionisation of muons:** Muons create secondary knock-on electrons inside the investigated sample via ionisation described by Eq. (1) in Sec. 2.1. The distribution of the number and the energy spectrum of secondary electrons is described by the following equation [22]:

$$\frac{\mathrm{d}^2N}{\mathrm{d}E\mathrm{d}L} = 0.3071\frac{Z}{A}\frac{q_e}{\beta^2}\frac{F(E)}{E^2} \quad , \tag{36}$$

where $F(E)$ is the spin dependent factor [22] and the other parameters are defined in Eq. (1). The integral of Eq. (36) shows that the number of secondary electrons with energy greater than a threshold energy is inversely proportional to the energy threshold, and is proportional to the $Z$ atomic number of the investigated material. In 10 cm material with unit density (1 g/cm$^3$), a relativistic particle creates an electron with an energy greater than 1 MeV and 0.01 electron with an energy greater than 100 MeV . The energy of the photons created via bremsstrahlung is typically $Z\,10^{-3}\,E$. For example, the bremsstrahlung of an 100 MeV electron can create a photon with the energy of 100 keV.

(ii) **Bremsstrahlung of cosmic ray electrons:** The electrons produced in the atmosphere by the decay of cosmic muons or in electromagnetic cascades can be detected with an energy up to 1 GeV. These electrons create photons inside the investigated material via bremsstrahlung. Note that electrons and photons are used for imaging in this case.

(iii) **Bremsstrahlung of high-energy muons:** At the energies above 30 GeV, the radiation energy loss, e. g. bremsstrahlung, pair production also contribute to the energy loss of muons [22]. The contribution of radiation energy loss increases with the increase of the energy, and it is proportional to $Z^2$. Thus, the high energy cosmic muons can also create photons inside the investigated material.

Note that the individual contributions of the above presented sources in the number of detected photons is not yet quantified.

The spectrum of secondary photons were investigated in low-$Z$ materials with the Muon Induced Rare Event Dynamic Observatory (MIREDO) [118]. The MIREDO spectrometer consists of a High Purity GErmanium (HPGe) detector and a pair of scintillator detectors to detect the muons that arrive from near the vertical directions. K. Bikit *et al.* measured the energy spectrum of the tertiary photons created in a calcium oxide (CaO) powder sample. The production cross section of the these photons, $\sigma_{Ph}$ was calculated to be [118]:

$$\sigma_{Ph}(\Delta E) = \frac{R_{HPGe}(\Delta E)}{\epsilon_{HPGe}(\Delta E) N_{CaO} F_{CR}} \left[\mathrm{s}^{-1}\mathrm{keV}^{-1}\right] \ , \tag{37}$$

where $R_{HPGe}(\Delta E)$ denotes the energy dependent photon count rate in HPGe, $\epsilon_{HPGe}(\Delta E)$ is the energy dependent photon detection efficiency of HPGe, $N_{CaO}$ is the number of CaO molecules, and $F_{CR}$ is the flux of cosmic rays in the units of $\mathrm{m}^{-2}$ $\mathrm{s}^{1}$ measured by the scintillator plates. They found that the measured photon cross section decreases exponentially with the increase of the energy [118]:

$$\sigma_{Ph}(E) \ = \ 19 \exp(-E\,[\mathrm{keV}]\,/92) \ + \ 2.6 \ . \tag{38}$$

The measured spectrum is the most abundant in the range 20 keV - 400 keV with the maximum around the energy of 100 keV. At lower energies, the number of photon counts is less due to the self-absorption in the sample. These results demonstrated the presence of cosmic ray induced tertiary photons in low-$Z$ materials. In the following sections the imaging system, its performance and the first image about a low-$Z$ material are presented.

## 7.1 Description of the novel method and the imaging system

The novel imaging method is based on the simultaneously detection of cosmic particles and the tertiary (or secondary) photons created inside the body of interest. The imaging system developed for imaging of low-$Z$ materials consists of a photon detector and a muon tracker.

To detect the tertiary photons, two different photon detectors were applied: a HPGe detector for the investigation of small-size ($< 10$ cm) samples and a scintillator-based detector for the imaging of organic materials with relatively larger size ($< 0.5$ m) [OL17, OL18]. In case of the HPGe detector, the investigated samples were shielded from environmental gamma radiation by a lead absorber wall. The investigated materials, e. g. a copper sample (Cu cylinder), were placed between the HPGe and the lead absorber wall. The scheme of the imaging system using a HPGe-based photon detector for imaging of low-$Z$ samples is shown in Fig 82 [OL17]. In case of the scintillators, the body of interests, e. g. bones, were placed into the "scintillator box". Figure 83 shows a photo (*a panel*) and the schematic view (*b panel*) of the imaging system using a box of plastic scintillators with the imaging volume of 0.125 $m^3$ for photon detection.

For both photon detectors, tracking systems consist of close cathode chambers were designed. For both photon detectors, the tracking systems were designed to match to their geometry in an optimal way: the cosmic muons arrive across the tracking system to the photon detectors within a vertical cone with the opening angle of 30°.

The tracking detector was triggered by the twofold coincidence of the CCC chambers. The trigger signals of the trackers generated logic output signals which were stored with their time stamps in CAEN fast digitiser. In addition, the signals from the photon detectors with their amplitude and time relative to the start of the measurement were also stored in the fast digitisers. The distribution of the time difference (coincidence time) between the signal production time of the CCC chambers and the photon detector was found to be within 1 $\mu$s (with the FWHM of 0.5 $\mu$s) for the HPGe [OL17] and 200 ns for the scintillator-based photon detector [OL18]. With such a time resolution, the gamma background is small, thus the shielding of the scintillators were not necessary. Note that the quality of the image was not strongly influenced by the reduced energy resolution of the plastic scintillators.

In case of both imaging systems, muon tracks which interacted with the sample and created signal inside the photon detector are selected by a coincidence requirement in the tracking system and the photon detector. The resulting image of the investigated material is reconstructed by the selected tracks.

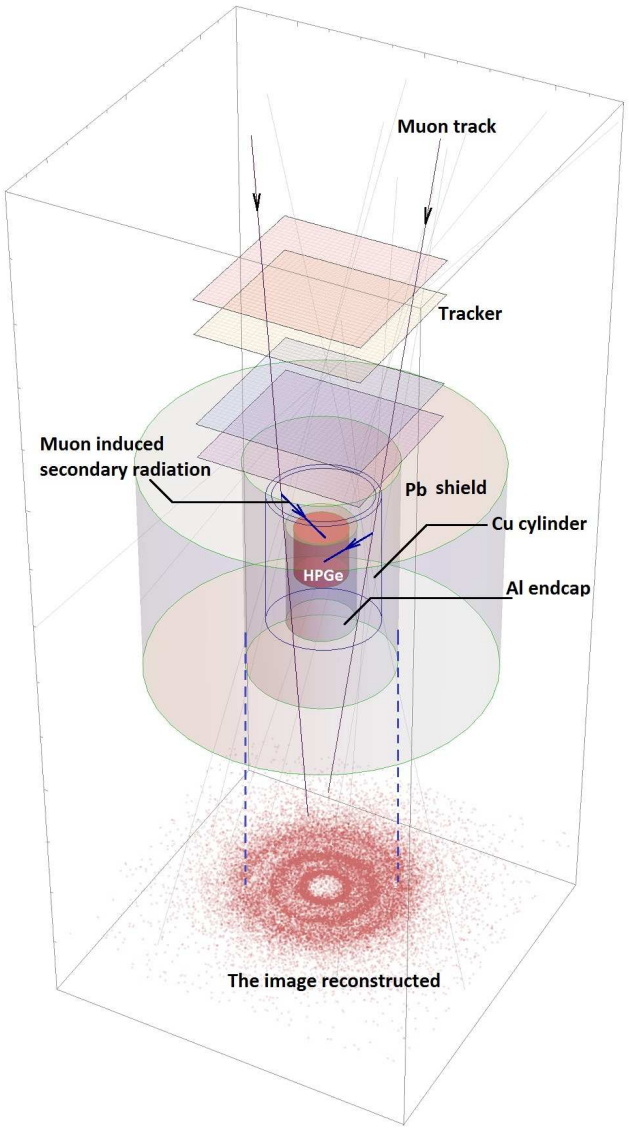


Figure 82: The new imaging technique is based on the simultaneous detection of cosmic muons, and secondary photons created inside the investigated sample. Here the schematic of the imaging system consists of a HPGe detector and a CCC-based tracker is presented [OL17, 119].

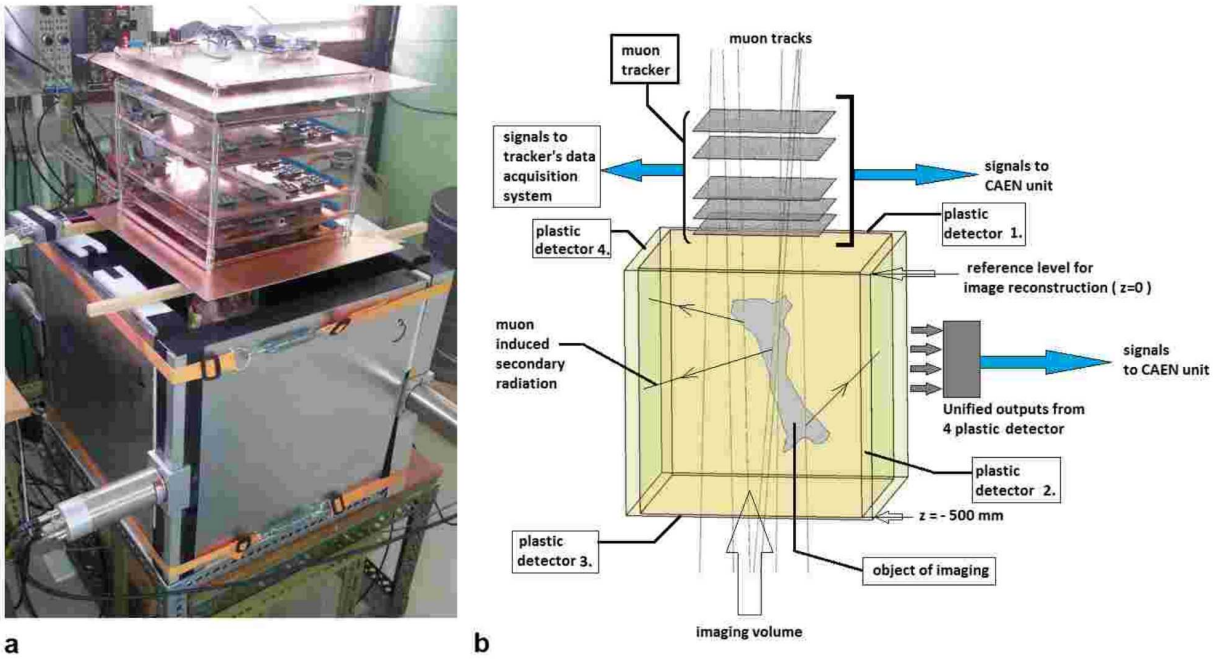


Figure 83: **a:** Photo about the portable muon imaging system with five layers of CCCs and plastic scintillator detector with the imaging volume of 0.125 $m^3$ [OL18]. **b:** The schematic view of the scintillator-based imaging system with the data taking procedure [OL18].

## 7.2 Performance of the imaging systems

Present section focuses on the performances of the developed imaging systems. Note that here only those performance parameters are presented which could be determined from the data of the tracking detector. Other performance parameters, e. g. the detection efficiencies of photon detectors, are not presented here.

I performed the offline analysis in the data of the tracking detector to determine the basic performance parameters, such as tracking efficiency and position resolution, and to contribute to the imaging procedure. Trajectories of cosmic particles were reconstructed by the combinatorial tracking algorithm which was presented in Sec. 5.4. Tracks with clusters on four different chambers were accepted for further analyses. The track coordinates were calculated in different horizontal planes inside and under the photon detectors. Furthermore, time stamp of each track was provided for further analysis together with the signals of the photon detectors.

To minimise the imaging time which is necessary to discriminate different low-$Z$ objects, one has to maximise the detection efficiency of the applied tracking system. Both the trigger and tracking efficiencies were calculated for the tracking systems with the algorithm which was presented in Sec. 5.5.1. The trigger efficiencies were found to be close to 100 % for each chamber. Figure 84 shows the tracking efficiencies which were found to be around 96 % for each of the chambers, except at the place of internal wire support plastic bar in "MT31" chamber. The resulting tracking efficiencies were found to be above 99 % for both imaging systems [OL17]. The observed efficiency values confirmed that the CCC chambers provided reliable tracking information during the measurements.

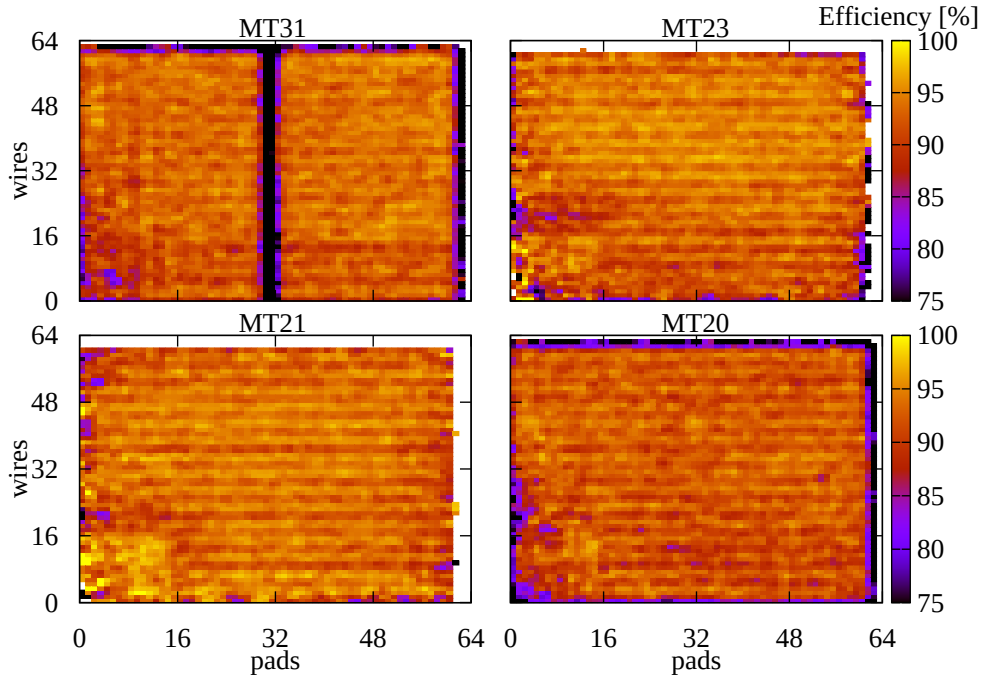


Figure 84: Tracking efficiencies was found to be around 96 % for each CCC layer, except at place of internal wire support plastic bar in "MT31" chamber. The combined tracking efficiency was found to be above 99 % for the developed imaging system [OL17].

The resolution of the images depend on the position resolutions of the tracking layers. The position resolutions were calculated by the same method as presented in Sec 5.5.3. Figure 85 shows the residual distributions and the corresponding RMS values for each of the tracking layers. Position resolution was found to be better than 2.5 mm for each tracking layer, consequently the position resolution of the resulting images were also better than 2.5 mm [OL17].

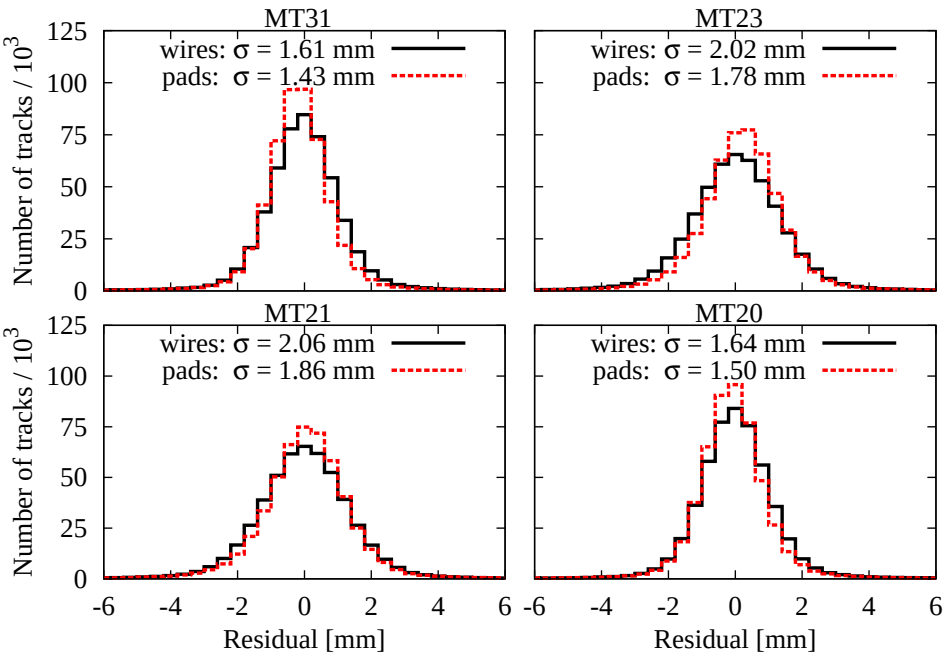


Figure 85: The distribution of the difference between fitted and measured tracks with four points (residuals) for each CCC layer in both wire (*black*) and pad (*red*) directions. The position resolutions were found to be better than 2.5 mm (RMS) for each tracking layer. The resolution of the images were also better than 2.5 mm. [OL17].

## 7.3 First images about low-$Z$ materials

To demonstrate the applicability the novel method, a copper sample with cylindrical shape was placed inside the HPGe detector. The imaging was performed with the data taking time of 24 hours. The *upper left panel* of Fig. 86 shows a photo about the experimental arrangement with the aluminium (Al) endcap of the HPGe detector, the cylindrical copper (Cu) sample which surrounds the HPGe crytal and the outer lead (Pb) shielding.

The images of the investigated sample were reconstructed by offline analysis of both the tracker's and the HPGe's data. The time stamps of the tracker's data were matched with the time stamps of the HPGe's data track-by-track. Those tracks were selected for imaging purpose which were in coincidence with tertiary photons within the time interval of 1 $\mu$s. A cut on the maximum photon energy was also applied. It was set to 6.4 MeV to exclude those photons which was induced by direct interactions of cosmic muons with the Ge crystal inside the HPGe detector. A 3-dimensional image was also obtained by

dividing the investigated sample with 20 horizontal planes and calculating the extrapolated coordinates of the reconstructed tracks in each plane.

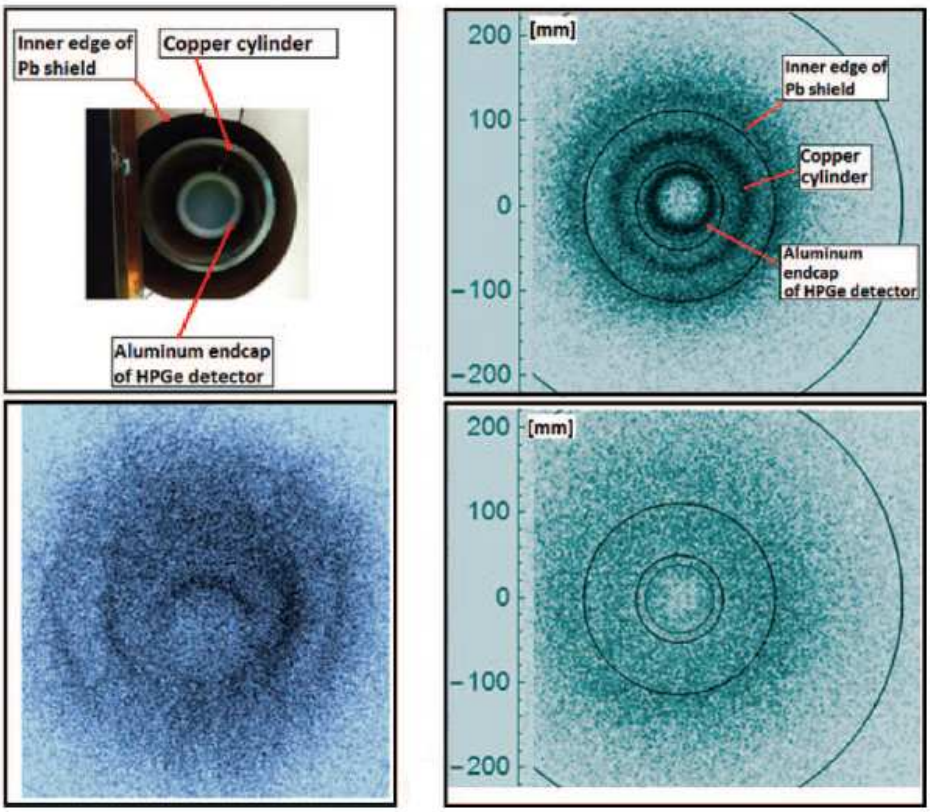


Figure 86: *Upper left:* A photo about the HPGe detector with its Al endcap, the cylindrical Cu sample and the Pb shielding [OL17]. *Upper right:* A 2-dimensional image in a horizontal plane inside HPGe about the experimental setup is achieved by those muons which were in coincidence with events in the HPGe detector [OL17]. *Lower left:* A 3-dimensional image was achived by the calculation of coordinates in 20 parallel horizontal planes inside the sample [OL17]. *Lower right:* 2-dimensional image in a horizontal plane which is placed under the HPGe detector, as we expected the Cu sample and HPGe detector structure were not visible [OL17].

Figure 86 shows the resulting images as well. The *upper right panel* shows the 2-dimensional image about this experimental arrangement in the plane of the Al endcap of the HPGe detector. The *lower left panel* of Fig. 86, 3-dimensional image of the same experimental arrangement. The 2-dimensional and 3-dimensional images visualised the lead shield, the copper sample (Cu cylinder) and the aluminium endcap of the HPGe

detector. Note that, the Ge crystal inside the HPGe was not visible because of the signal amplitude of the direct interaction of muons with the crystal is about 60 MeV which energy value is well above the maximum energy cut of the HPGe detector. The *lower right panel* of Fig. 86 shows the 2-dimensional image in a horizontal plane which placed under the HPGe detector [OL17]. As it was expected, none of investigated structures were observed in the image which was taken under the Ge crystal.

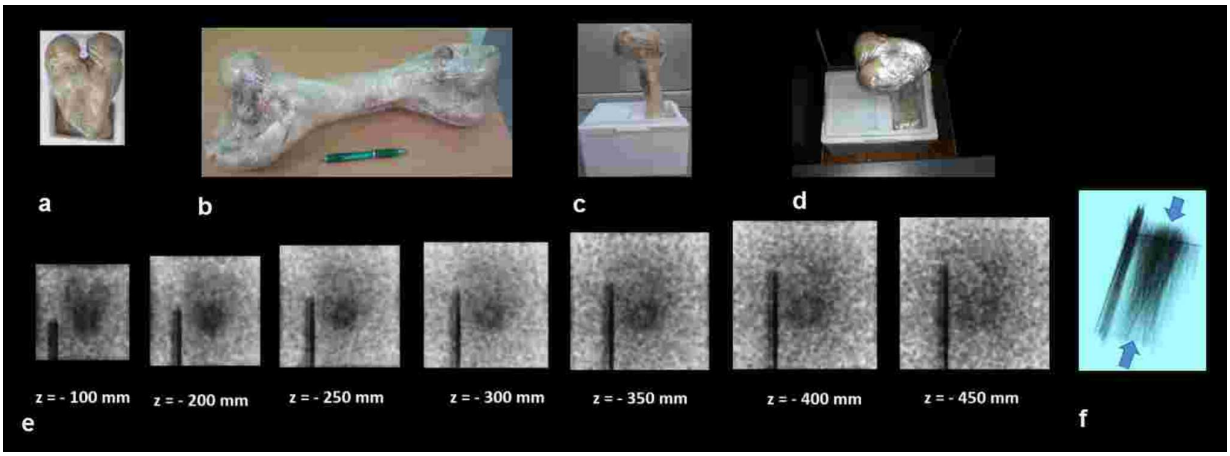


Figure 87: Photos (**a - d**), the corresponding 2-dimensional images (**e**) and the 3-dimensional cosmic muon image (**f**) about a cow femur bone. The time of data taking was about 24 hours [OL18].

The first images taken about low-$Z$ organic materials are shown in Fig. 87 [OL17]. These images were taken by the scintillator-based imaging system setup. Here the photos of a cow femur bone (a-d) and its 2-dimensional images at different depths (e), as well as the reconstructed 3-dimensional image (f) are presented. These results demonstrate that bones and tissues also can be imaged with the developed non-invasive method, and it can be promising in medical imaging.

These results demonstrate that the samples with low atomic number can be visualised by the muon induced secondaries because of the relatively high transparency of these materials. This is a huge advantage of this novel method to compare with both absorption and scattering imaging methods.

## 7.4 Summary of low-$Z$ material imaging

Pioneering study of a novel approach to cosmic muon imaging of low-$Z$ materials was presented in this chapter. The developed imaging systems consist of charged particle trackers and a photon detectors (HPGe and scintillators). The first cosmic muon images were taken about low-$Z$ materials: a copper sample was imaged around the HPGe detector, and a cow femur bone was reconstructed inside a scintillator-based photon detector.

The presented result demonstrated that the low-$Z$ materials can be imaged by those muons which are in coincidence with photons created by the bremsstrahlung of the secondary electrons. My contributions to the development of this novel approach are summarised in the following points.

(i) Installation and test of the tracking layers within the new imaging system.

(ii) Determination of the performance of the imaging system.

(iii) Contribution to imaging process by the reconstruction of muon trajectories and calculation of their coordinates inside the investigated sample.

The presented results were published in Refs. [OL17, OL18], as well as were highlighted in Refs. [119, 120, 121].

The developed novel approach is non-invasive, thus it can have high impact in the field of medical applications, life sciences, illicit trafficking, or archaeology where mostly organic objects are investigated. The ongoing studies focus on the application oriented development of the imaging system.

The aim of future measurements and detector upgrades is to determine the average atomic numbers and densities from the obtained images, as well as to minimise the time of imaging. The application of more efficient photon detectors, such as bizmuth germanate (BGO) or natrium iodide (NaI), which have higher signal production efficiency, can decrease the time of imaging. The resolution of the image can be improved by decreasing the angular resolution of the muon tracker.

# 8 Summary and future perspectives

In this Ph.D. thesis, I presented my work focused on research and development of particle detectors and their applications. I did my experimental work in the MTA Lendület Innovative Detector Development Group and the Budapest group of the ALICE Collaboration. My motivation was twofold.

(i) Detector physics investigation and upgrades of the subdetectors of the ALICE experiment are necessary to produce reliable data during the high-luminosity LHC periods.

(ii) Research and development of portable and low-power tracking systems with reasonable position and angular resolutions for imaging the interior of large-scale objects, e. g. mountains or volcanoes, as well as the development of a non-invasive method for imaging of low-$Z$ and small-size bodies.

I investigated the performance and ageing of the ALICE High Momentum Particle Identification Detector during the LHC Run 1 period (2010-2013) [OL06, OL07]. The gas gain, the number of photoelectron clusters and the quantum efficiency of photocathodes were determined by the analysis the p-p and p-Pb collision data and by Monte Carlo simulations. The results show that the HMPID detector was not suffering any ageing effects, and it can operate reliably until the end of the first high-luminosity LHC period (2023) [OL06]. Moreover, I contributed to the development of the Very High Momentum Particle Identification Detector [OL03, OL04, OL05] and the upgrade of the ALICE Time Projection Chamber [OL02].

Based on the new variant of Multi-Wire Proportional Chambers, I developed, built and optimised portable, low power ($\sim$ 5 W) tracking detector systems with reasonable position ($<$ 4 mm) and angular resolutions ($<$ 15 mrad) to detect underground rock inhomogeneities, e. g. caverns, and to image the density variation inside the active volcanoes [OL01, OL08, OL09, OL10, OL11, OL12].

I demonstrated that the close cathode chamber-based portable muon telescopes operate reliably outside of the laboratory. I measured the flux of cosmic muons in various

underground tunnel systems. I demonstrated that the developed tracking systems can be applied to detect of underground caverns and to measure the cosmic background in physics experiments [OL08, OL09, OL10, OL11, OL13, OL14, OL15, OL16].

I contributed to the development of a non-invasive method for imaging of low-$Z$ and small-size bodies via the tracking of cosmic particles. The novel method is based on the simultaneous detection of cosmic particles and photons produced by bremmstrahlung. The developed imaging system consists of a muon tracker and a photon detector. I designed and tested the muon tracker. I analysed the measured data and determined the tracking efficiency ($> 99$ %) and the resolution ($< 2.5$ mm) of the imaging system. Furthermore, I contributed to the imaging procedure by the reconstruction of the trajectory of cosmic particles and their positions inside the investigated materials. A copper sample and the aluminium endcap of the photon detector were discriminated, as well as a bone was imaged by the novel method within reasonable time (24 hour) [OL17, OL18].

Besides the scientific impact, the developed detector systems and methods may have high social benefits. Our intellectual property, the "Muographic Observation System" [OL12] is planned to be applied to image the interior of active volcanoes in 12 hour intervals and produce density maps for geologist who can analyse those and alert the responsible agencies.

The further optimisation and development of the non-invasive imaging method can enter new possibilities in the field of medical imaging: the frequency and duration of medical inspections will not be limited, and the lack of radiation exposure can simplify the inspection procedure.

# Acknowledgements

I would like to express my gratitude to my family and friends for their patience and continuous encouragement.

I would like to express my gratitude to Dezső Varga, my supervisor and Gergő Hamar for the fruitful discussions and the possibility to work with them.

I would like to express my gratitude to Gergely Gábor Barnaföldi, my supervisor for the opportunity to contribute to the ALICE experiment, the technical support at the underground measurements, reading and correcting the manuscripts.

The technical support during the detector construction and underground measurements provided by the REGARD group is gratefully acknowledged.

I would like to express my gratitude to Gergely Surányi (MTA-ELTE Geological, Geophysical and Space Sciences Research Group) for the technical support at all of the underground measurement sites, for the geodesic measurements, and the fruitful discussions.

I would like to thank to Istvan Bikit, Kristina Bikit, and Dusan Mrdja (University of Novi Sad) for the fruitful collaboration.

I would like to thank to Giacomo Volpe, Levente Molnár, Antonello Di Mauro, and Giacinto De Cataldo for the discussions about the technical details of the HMPID detector.

The possibility to perform measurements in Felsenkeller is gratefully acknowledged to Daniel Bemmerer and the Helmholtz Zentrum Dresden Rossendorf.

I would like to thank to prof. Hiroyuki K. M. Tanaka (University of Tokyo) for the fruitful collaboration.

I would like to express my gratitude to Dániel Barna and Márton Nagy for the review of my thesis during the defence procedure of the Wigner Research Centre for Physics.

I would like to thank to the Wigner Research Centre for Physics and the Eötvös Loránd University for the continuous support.

My research was supported by the Lendület Grant of the HAS under the grant No. LP2013-60 and the Hungarian OTKA Grant NK106119.

# A. Glossary

**ACORDE**: ALICE COsmic Ray DEtector
**ADC**: Analog-to-Digital Converter
**AHV**: American High Voltage
**ALICE**: A Large Ion Collider Experiment
**AMS**: Atomic Mass Spectrometer
**ASCII**: American Standard Code for Information Interchange
**ASIC**: Application-Specific Integrated Circuit
**AT**: Accepted Trigger
**ATLAS**: A Toroidal LHC ApparatuS
**CAMAC**: Computer AutoMatised And Controlled
**CCC**: Close Cathode Chamber
**CERN**: European Laboratory for Particle Physics
**CMOS**: Complementary-Metal Oxide Semiconductor
**CMS**: Compact Muon Solenoid
**CORSIKA**: COsmic Ray SImulations for KAscade
**CsI**: Caesium Iodide
**CT**: Computed Tomography
**DAQ**: Data AcQuisition
**DCS**: Detector Control System
**DDL**: Detector Data Link
**ECC**: Emulsion Cloud Chamber
**EECR**: Extrem-Energy Cosmic Ray
**EMCAL**: ElectroMagnetic CALorimeter
**ERI**: Earthquake Research Institute of the University of Tokyo
**ESD**: Event Summary Data
**FEE**: Front-End Electronics
**GEANT**: GEometry ANd Tracking

**GEM**: Gas Electron Multiplier
**GRPC**: Glass Resistive Plate Chamber
**GZK**: Greisen – Zatsepin – Kuzmin
**HEP**: High Energy Physics
**HMPID**: High Momentum Particle Identification Detector
**HPGe**: High Purity Germanium
**HV**: High Voltage
**ISS**: International Space Station
**ITS**: Inner Tracking System
**LAM**: Look-At-Me
**LANL**: Los Alamos National Laboratory
**LHC**: Large Hadron Collider
**LS**: Long Shutdown
**LV**: Low Voltage
**MIP**: Minimum-Ionising-Particle
**MIREDO**: Muon Induced Rare Event Dynamic Observatory
**MPGD**: Micro-Pattern Gaseous Detector
**MPV**: Most-Probable-Value
**MRI**: Magnetic Resonance Imaging
**NIM**: Nuclear Instruments Module
**PC**: Photocathode
**PCB**: Printed Circuit Board
**PE**: Photoelectron
**PET**: Positron Emission Tomography
**PHOS**: PHOton Spectrometer
**PID**: Particle Identification
**PISO**: Parallel In Serial Out
**PMT**: Photo-Multiplier Tube
**PS**: Proton Synchrotron
**PMD**: Pre-Shower Multiplicity Detector
**QE**: Quantum Efficiency
**QGP**: Quark Gluon Plasma
**R&D**: Research and Development

**RE**: Read-End
**RICH**: Ring Imaging Cherenkov
**RPC**: Resistive Plate Chamber
**RPi**: Raspberry Pi
**SM**: Standard Model
**SPS**: Super Proton Synchrotron
**SUSY**: Supersymmetry
**THP**: Temperature-Humidity-Pressure
**TOF**: Time-Of-Flight
**TOMUVOL**: TOmographie MUonique des VOLcans
**TPC**: Time Projection Chamber
**TRD**: Transition Radiation Detector
**UHECR**: Ultra-High Energy Cosmic Ray
**UV**: Ultra Violet
**VHMPID**: Very High Momentum Particle Identification Detector
**ZDC:** Zero Degree Calorimeter

# Bibliography

[OL01] D. Varga, G. Hamar, G. Nyitrai, L. Oláh:
Advances in High Energy Physics **2016** (2016) 1962317

[OL02] H. Appelshaeuser *et al.* (ALICE TPC Upgrade Collaboration):
Technical Design Report ALICE-TDR-016-ADD-1 CERN-LHCC-2015-002 (2015)

[OL03] T. C. Acconcia *et al.* (VHMPID Collaboration):
Eur. Phys. J. Plus **129**: 91 (2014) 30

[OL04] T. C. Acconcia *et al.* (VHMPID Collaboration):
Nucl. Instrum. Meth. A **732** (2013) 361-365

[OL05] T. C. Acconcia *et al.* (VHMPID Collaboration):
Nucl. Instrum. Meth. A **767** (2014) 50-60

[OL06] F. Barile *et al.* (HMPID Collaboration):
Performance of the HMPID detector during LHC Run1 and perspectives
ALICE Public Note https://aliceinfo.cern.ch/Notes/node/474 (2016)

[OL07] L. Oláh for the ALICE Collaboration:
The performance of the ALICE High Momentum Particle Identification Detector in pp, p-Pb and Pb-Pb collisions, poster at Quark Matter 2014 Conference, https://indico.cern.ch/event/219436/contributions/1523334/
(last view in the 27th of September in 2016)

[OL08] G. G. Barnaföldi, G. Hamar, H. G. Melegh, L. Oláh, G. Surányi, D. Varga:
Nucl. Instrum. Meth. A **689** (2012) 60-69

[OL09] L. Oláh, G. G. Barnaföldi, G. Hamar, H. G. Melegh, G. Surányi, D. Varga:
Geosci. Instrum. Method. Data Syst. **1** (2012) 229-234

[OL10] L. Oláh, G. G. Barnaföldi, G. Hamar, H. G. Melegh, G. Surányi, D. Varga: Advances in High Energy Physics **2013** (2013), 560192

[OL11] L. Oláh, G. G. Barnaföldi, G. Hamar, H. G. Melegh, G. Surányi, D. Varga: Journal of Physics: Conference Series **632** (2015) 012020

[OL12] G. Hamar, T. Kusagaya, L. Oláh, H. K. M. Tanaka, D. Varga: Muographic Observation System, 2016-087436 (PTZTA153) intellectual property

[OL13] L. Oláh, G. Surányi, D. Bemmerer, G. G. Barnaföldi, G. Hamar, H. G. Melegh, D. Varga: Journal of Physics: Conference Series **665** (2016) 012032

[OL14] L. Oláh, G. G. Barnaföldi, G. Hamar, H. G. Melegh, G. Surányi, D. Varga: Proceedings of Science (NIC XIII) **129** (2015) 6

[OL15] L. Oláh, G. G. Barnaföldi, G. Hamar, H. G. Melegh, G. Surányi, D. Varga: Astroparticle, Space Physics, Raditation Interaction, Detectors and Medical Physics Applications **8** (2014) 280-284

[OL16] L. Oláh, G. G. Barnaföldi, G. Hamar, P. Pázmándi, G. Surányi, D. Varga: Muography: Perspective Drawing in the 21st Century (2015) 77-85

[OL17] I. Bikit, D. Mrdja, K. Bikit, J. Slivka, N. Jovancevic, L. Oláh, G. Hamar, D. Varga: European Physics Letters **113** (2016) 58001

[OL18] D. Mrdja, I. Bikit, K. Bikit, J. Slivka, J. Hansman, L. Oláh, D. Varga: *First cosmic-ray images of bone and soft tissue* accepted research article in European Physics Letters (7th of December in 2016)

[1] W. N. Cottingham and D. A. Greenwood: *An Introduction to the Standard Model of Particle Physics* (1998) Cambridge

[2] Figure about the particles of Standard Model: https://en.wikipedia.org/wiki/Standard_Model#/media/File:Standard_Model_of_Elementary_Particles.svg (last view in the 27th of September in 2016)

[3] Super-Kamiokande Collaboration: Phys. Rev. Lett. **81** (1998) 1562-1567

[4] Schematic figure about a Pb-Pb collision in ALICE:
https://cds.cern.ch/record/2032743 (last view in the 27th of September in 2016)

[5] The ALICE Collaboration: JINST **3** (2008) S08002

[6] Figure about the energy spectrum of cosmic rays at the surface of the Earth:
http://www1.na.infn.it/wsubnucl/cosm/JemEuso/physics.html
(last view in the 27th of September in 2016)

[7] A. Augilar *et al.* (AMS Collaboration): PRL **110** (2013) 141102

[8] A photo of the AMS-02 on the ISS:
https://www.ams.nasa.gov/images/AMS-02_Project_Photos/AMS%20On-Orbit/110519%20PLB%20and%20Deploy/iss027e034934.jpg
(last view in the 27th of September in 2016)

[9] P. K. F. Grieder: *Cosmic Rays at Earth* (2001) Elsevier

[10] K. Greisen: Phys. Rev. Lett. **16** (1966) 748

[11] G. Z. Zatsepin and V. A Kuzmin: Journal of Exp. and Theor. Phys. Lett. **4** (1966) 78

[12] K. Moskvitch: Nature **514** (2014) 20-22

[13] The Pierre Auger Collaboration: Phys. Lett. B. **685** (2010) 239-246

[14] Figure about the energy range of X-rays and their applications:
https://en.wikipedia.org/wiki/X-ray (last view in the 27th of September in 2016)

[15] S. G. Patching: Journal of Diagnostic Imaging in Therapy. 2 **1** (2015) 30-102

[16] L. W. Alvarez *et al.*: Science **167** 832-839

[17] E. Caffau, F. Coren, G. Giannini: Nucl. Instrum. Meth. A **385** (1997) 480-488

[18] H. K. M. Tanaka *et al.:* Earth and Planetary Science Letters **263** (2007) 104-113

[19] S. Okubo and H. K. M. Tanaka: Meas. Sci. Technol. **23** (2012) 042001

[20] K. Nagamine *et al.:* Nucl. Instrum. Meth. A **356** (1995) 585-595

[21] H. Bethe and J. Ashkin: Experimental Nuclear Physics (1953) 253

[22] K. A. Olive *et al.* (Particle Data Group): Chin. Phys. C **38** (2014) 090001

[23] F. Sauli: *Principles of operation of multiwire proportional and drift chambers* CERN (1977)

[24] G. Charpak *et al.*: Nucl. Instrum. Meth. A **62** (1968) 262

[25] D. Varga *et al.*: Nucl. Instrum. Meth. A **648** (2011) 163-167

[26] D. Varga *et al.*: Nucl. Instrum. Meth. A **698** (2013) 11-18

[27] D. Varga *et al.*: Eur. J. Phys. **36** (2015) 065006

[28] R. Santonico and R. Cardarelli: Nucl. Instrum. Meth. A **187** (1981) 377-380

[29] G. Aielli *et al.*: Nucl. Instrum. Meth. A **714** (2013) 115-120

[30] F. Sauli: Nucl. Instrum. Meth. A **386** (1997) 531

[31] F. Sauli: Nucl. Instrum. Meth. A **805** (2016) 2-24

[32] The official webpage of RD51 Collaboration: http://rd51-public.web.cern.ch (last view in 5th of April in 2016)

[33] Figures about a Gas Electron Multiplier: http://www.oeaw.ac.at/smi/research/advanced-instrumentation/detector-development/ (last view in 5th of April in 2016)

[34] D. R. Nygren: eConf C **740805** (1974) 58

[35] H. Appelshaeuser *et al.* (ALICE TPC Upgrade Collaboration): Technical Design Report ALICE-TDR-016 CERN-LHCC-2013-020 (2013)

[36] The ALICE Collaboration: ALICE Public Note *ALICE-PUBLIC-2015-004* (2015)

[37] The ALICE Collaboration: ALICE HMPID Technical Design Report CERN/LHCC 98/19 (1998)

[38] G. Volpe: Nucl. Instrum. Meth. A **766** (2014) 259-262

[39] The ALICE Collaboration: Int. J. Mod. Phys. A **29** (2014) 1430044

[40] E. Nappi *et al.* (RD26 Collaboration):
LDRB-Status-Report-RD26 CERN-LHCC-96-020 (1996) 1-25

[41] C. Pastore *et al.*: Nucl. Instrum. Meth. A **639** (2011) 231

[42] J. C. Santiard and K. Marent: Nucl. Instrum. Meth. A **518** (2004) 498

[43] G. De Cataldo *et al.*: Nucl. Instrum. Meth. A **639** (2011) 211

[44] H. Hoedlmoser: *Development of Large Area CsI Photocathodes for the ALICE/HMPID RICH Detector* Ph.D. thesis CERN-THESIS-2006-004 Technical University of Vienna (2006)

[45] A. Breskin: Nucl. Instrum. Meth. A **371**, (1996) 116

[46] A. Di Mauro *et al.*: Nucl. Instrum. Meth. A **433** (1999) 190

[47] A. Braem *et al.*: Nucl. Instrum. Meth. A **515** (2003) 307

[48] The official webpage of ALICE Analysis Framework:
aliweb.cern.ch/Offline (last view in the 27th of September in 2016)

[49] The official webpage of Root TTree class:
https://root.cern.ch/root/html518/TTree.html
(last view in the 27th of September in 2016)

[50] The official webpage of ALICE Monitoring System:
alimonitor.cern.ch (last view in the 27th of September in 2016)

[51] D. Di Bari: Nucl. Instrum. Meth. A **502** (2003) 300

[52] The official webpage of PYTHIA simulation:
https://pythia6.hepforge.org/ (last view in the 27th of September in 2016)

[53] The official webpage of HIJING simulation:
http://ntc0.lbl.gov/ xnwang/hijing/ (last view in the 27th of September in 2016)

[54] The official webpage of ALICE HMPID code:
http://svn.cern.ch/guest/AliRoot/trunk/HMPID/AliHMPIDv3.cxx
(last view in the 27th of September in 2016)

[55] The official webpage of ALICE HMPID Hit class:
http://svn.cern.ch/guest/AliRoot/branches/v4-07-Release/HMPID/AliHMPIDHit.h
(last view in the 27th of September in 2016)

[56] A. Di Mauro *et al.*: IEEE Transactions on Nuclear Science **52** (2005) 4

[57] G. De Cataldo: Nucl. Instrum. Meth. A **766** (2014) 19-21

[58] H. Hoedlmoser *et al.*: Nucl. Instrum. Meth. A **574**, (2008) 28

[59] E.P. George, Commonwealth Engineer **1** (1955) 455-457

[60] H. K. M. Tanaka *et al.:* American Journal of Science **308** (2008) 843-850

[61] S. Agostinelli *et al.*: Nucl. Instrum. Meth. A **506** (2003) 250-303

[62] A photo about the eruption of Asama volcano:
http://www.zimbio.com/pictures/4oNQpWx0ElS/Mt+Asama+Erupts/
Mt+Asama+Volcano+in+Japan (last view in the 27th of September in 2016)

[63] H. K. M. Tanaka *et al.:* Nat. Commun. **5** 3381 (2014) 9p

[64] K. N. Borozdin *et al.:* Nature **422** (2003) 277

[65] L. J. Schultz *et al.*: Nucl. Instrum. Meth. A **519** (2004) 687-694

[66] S. Pesente *et al.*: Nucl. Instrum. Meth. A **604** (2009) 738-746

[67] K. Gnanvo *et al.*: Nucl. Instrum. Meth. A **652** (2011) 16-20

[68] The official webpage of Decision Sciences:
https://www.decisionsciences.com/mmpds/technology/
(last view in the 27th of September in 2016)

[69] K. N. Borozdin *et al.*: PRL **109** (2012) 152501

[70] K. Morishima *et al.*: *Measurement of Inner Structure of Fukushima Daiichi Nuclear Power Plant by Cosmic Ray Muon Radiography with Nuclear Emulsion* http://w4.gakkai-web.net/jps_search/2015aue/data/html/programsj.html (last view in the 5th of April in 2016)

[71] S. Cecchini and M. Spurio: Geosci. Instrum. Method. Data Syst. **1** (2012) 185-196

[72] D. Heck *et al.*: Forschungszentrum Karlsruhe Report FZKA 6019 (1998)

[73] N. Lesparre *et al.*: Geophys. J. Int. **183** (2010) 1348-1361

[74] T. Gaisser: *Cosmic Rays and Particle Physics* Cambridge University Press (1990)

[75] E. V. Bugaev *et al.*: Phys. Rev. D **58** (1998) 054001

[76] D. Reyna: arXiv:hep-ph/0604145v2 (2006) 7p

[77] R. Nishiyama: *Accurate muographic imaging of volcanoes by background noise reduction with nuclear emulsions* Ph.D. thesis University of Tokyo (2015)

[78] T. Hebbeker and C. Timmermans: Astroparticle Physics **18** (2002) 107-127

[79] K. Jourde *et al.:* Geophys. Res. Lett. **40** 24 (2013) 6334-6339

[80] R. Nishiyama, S. Miyamoto, and N. Naganawa: Geosci. Instrum. Method. Data Syst. **3** (2014) 29-39

[81] R. Nishiyama *et al.:* Geophys. J. Int. **206** (2016) 1039-1050

[82] S. Roh *et al.:* Astropart. Phys. **44** (2013) 1-8

[83] N. Lesparre *et al.:* Geophys. J. Int. **190** (2012) 1008-1019

[84] D. Carbone *et al.:* Geophys. J. Int. **196** (2013) 633-643

[85] T. Nakamura *et al.:* Nucl. Instrum. Meth. A **556** (2006) 80-86

[86] K. Morishima: Physics Procedia **80** (2015) 19-24

[87] H. K. M. Tanaka *et al.:* Nucl. Instrum. Meth. A **575** (2007) 489-497

[88] L. Consiglio and V. Tioukov: Astroparticle, Space Physics, Raditation Interaction, Detectors and Medical Physics Applications **8** (2014) 708-713

[89] The official webpage of ScanPyramids project:
http://www.scanpyramids.org/ (last view in the 27th of September in 2016)

[90] C. Carloganu *et al.:* Geosci. Instrum. Method. Data Syst. **2** (2013) 55-60

[91] S. Bouteille *et al.:* Nucl. Instrum. Meth. A **834** (2016) 187-191

[92] S. Procureur: *MPGD-based muon telescopes for archeology: the ScanPyramids project*
MPGD Applications Beyond Fundamental Science Workshop 15-16 September 2016
Aveiro Portugal

[93] The official webpage of Raspberry Pi:
http://www.raspberrypi.org/ (last view in the 27th of September in 2016)

[94] The official webpage of American High Voltage:
http://www.ahv.com/ (last view in the 27th of September in 2016)

[95] G. Hamar: *Investigation of high momentum particles in heavy ion collisions*
Ph.D. thesis Eötvös Loránd University 2015 (in Hungarian)

[96] User manual for the softwares of the DAQ system developed by the REGARD:
http://regard.kfki.hu/cikkek/MtRD_Guides_20150306.pdf
(last view in the 27th of September in 2016)

[97] J. Apostolakis *et al.*: Journal of Physics: Conference Series **219** (2010) 032044

[98] V. N. Ivanchenko *et al.*: Journal of Physics: Conference Series **219** (2010) 032045

[99] L. Oláh: *Szerkezetvizsgálat kozmikus részecskék segítségével*
M.Sc. thesis Eötvös Loránd University 2012 (in Hungarian)

[100] A. I. Barboutit and B. C. Rastin: *J. Phys. G: Nucl. Phys.* **9** (1983) 1577-1595

[101] S. Miyake *et al.*: Nuovo Cimento **32** (1964) 1505-1523

[102] C. Castagnoli *et al.*: Nuovo Cimento **35** (1965) 969-976

[103] M. G. K. Menon and P. V. Ramana Murthy:
Progr. Elementary Particles and Cosmic Rays **9** (1967) 161

[104] C. T. Stockel: J. Phys. A: Gen. Phys. **2** (1969) 639

[105] L. Bergamasco, P. B. D'Ettorre, and P. Picchi: Nuovo Cimento **4B** (1971) 59-67

[106] J. N. Crookes and B. C. Rastin: Nuclear Physics B **58** (1973) 93-109

[107] A. G. Wright: Proceedings of the 13th ICRC 3 (1973) 1709

[108] I. W. Rodgers and J. C. Percy: Proceedings of the 15th ICRC **6** (1977) 99-103

[109] P. N. Bhat and P. V. Ramana Murthy: J. Phys. G: Nucl. Phys. **4** (1978) 453-470

[110] A. Dragić *et al.*: Nucl. Instrum. Meth. A **591** (2008) 470-475

[111] S. Pal *et al.*: Pramana - J. Phys. **79** (2012) 1267-1270

[112] B. Mitrica *et al.*: Advances in High Energy Physics **2013** (2013) 256230

[113] K. Greisen: Phys. Rev. **61** (1942) 212-221

[114] D. Bemmerer *et al.*: JPCS **665** (2016) 012030

[115] L. Malmquist *et al.*: Geophysics **44** (1979) 1549-1569

[116] A Celmins: U.S. Army Ballistic Research Lab Technical Report-3110 (1990) 44

[117] C. Hagmann *et al.*: Nuclear Science Symposium Conference Record (2007) 1143-1146

[118] K. Bikit *et al.:* Appl. Radiat. Isot. **87** (2014) 77-80

[119] europhysicsnews: *Expanding Frontiers of Cosmic-ray Muon Imaging* 2016 47/4

[120] J Swain: *Imaging with muons* CERN COURIER 2016/07

[121] F. Levi: *Cosmic-ray muons: Pictures from the sky* Nature Physics **12** (2016) 376

# Summary

The motivation of my Ph.D. work was the research and development of gaseous detector systems for the LHC ALICE experiment, which investigates one of the open questions of particle physics, the origin of the Universe; as well as for the applications of particle physics, primarily for cosmic muon imaging.

The better understanding of the early state of the Universe can be allowed by increasing the energy and the luminosity of heavy-ion collisions. The particle rate produced in these collisions motivates the detector-physical investigation and the upgrades of the present subsystems of ALICE.

The instruments and methods developed for particle physics allow the wider spread of applications. Muon radiography can be applied to image the interior of large-scale objects, e. g. mountains or active volcanoes, furthermore, the non-invasive imaging of low-density and small-size materials is possible by a novel method. These can be realised by the application oriented development of detector systems.

The main results of my Ph.D. work are summarised in the following points:

(i) I investigated the variation of the operational parameters (gas gain, number of photoelectron clusters) and the ageing (quantum efficiency) of the photocathodes of the ALICE HMPID Cherenkov detector with the analysis of the data of LHC p-p and p-Pb collisions and Monte Carlo simulation. The results show that the HMPID will provide reliable data until the end of the first high-luminosty LHC period (2023). Besides, I contributed to the development of the VHMPID and the upgrade of the ALICE TPC.

(ii) I developed and built portable, low-power tracking systems with optimised position and angular resolutions for search underground rock inhomogeneities, e. g. caverns, and for radiograpic imaging of volcanoes. I optimised the operational parameters and the structure of the detector systems with measurements and Monte Carlo simulation.

(iii) I demonstrated that the developed portable detector systems are applicable for detect underground caverns, and the measurement of the angular-distribution of physics experiments' background, which is caused by cosmic particles.

(iv) I contributed to the development of a novel, non-invasive method for imaging of low-$Z$ and small-size materials with the application of tracking detectors and the analysis of the measured data. This method is based on the simultaneous detection of the muons, and the photons which are generated by the bremsstrahlung of the secondary electrons. The apparatus consists of a muon tracker and a photon detector. I calculated the tracking efficiency of the muon detector, the resolution of the imaging and the position of the particles inside the investigated sample. The applicability of the method was demonstrated by the imaging of copper, aluminium, and a bone.

# Összefoglalás

Doktori munkám motivációja gáztöltésű detektorrendszerek kutatás-fejlesztése volt a részecskefizika egyik nyitott kérdését, az Univerzum keletkezését vizsgáló LHC ALICE kísérlet́hez; valamint részecskefizikai alkalmazásokhoz, elsősorban kozmikus müonokkal történő képalkotáshoz.

Az Univerzium korai állapotának pontosabb megismerése a nehézion ütköztetések energiájának és luminozitásának növelésével érhető el az LHC gyorsítóban. Az itt keletkező nagy sugárterhelés motiválja jelenlegi ALICE alrendszereinek detektorfizikai vizsgálatát és továbbfejlesztését.

A részecskefizikában kifejlesztett berendezések és módszerek fejlődése lehetővé teszi az alkalmazások szélesebb körű elterjedését. Müonradiográfiával képet alkothatunk nagy méretű objektumok, pl. hegyek vagy aktív tűzhányók belsejéről, továbbá egy új eljárással lehetőség van a kis sűrűségű és kisméretű anyagok nem-invazív képalkotására. Ezek a detektorrendszerek alkalmazás-orientált fejlesztésével valósulhatnak meg.

Doktori munkám főbb eredményeit a következő pontokban foglalom össze:

(i) Megvizsgáltam az ALICE HMPID Cherenkov-detektor működési paraméterinek (gázerősítés, fotoelektron klaszterek száma) változását és a fotokatódjainak öregedését (kvantum hatásfok) az LHC p-p és p-Pb ütköztetések adatainak elemzésével és Monte Carlo szimulációval. Az eredmények alapán a HMPID megbízható adatokat biztosít az első nagy luminozitású LHC periódus végéig (2023). Emellett hozzájárultam az ALICE TPC és a tervzett VHMPID detektorok továbbfejlesztéséhez.

(ii) Kifejlesztetem és megépítettem hordozható, alacsony fogyasztású, optimalizált hely- és szögfelbontású detektorrendszereket föld alatti kőzet-inhomogenitások, pl. üregek kutatására, és vulkánok átvilágátására. Mérésekkel és Monte Carlo szimulációval optimalizáltam a detektorok működési paramétereit és felépítését.

(iii) Mérésekkel demonstráltam, hogy a kifejlesztett hordozható detektorrendszerek alkalmazhatók föld alatti üregek kimutatására és fizikai kísérletek kozmikus részecskék által keltett hátterének szög-eloszlás mérésére.

(iv) Nyomkövető detektorok alkalmazásával és a mérések elemzésével hozzájárultam egy új, nem-invazív, kis rendszámú és kisméretű anyagok képalkotására alkalmas eljárás kifejlesztéséhez. Ennek alapja a müonok és a másodlagos elektronok fékezési sugárzása által keltett fotonok együttes detektálása. A berendezés egy müon- és egy fotondetektorból épül fel. Kiszámoltam a müondetekor nyomkövetési hatásfokát, a képalkotás felbontását és a részecskék helyét a vizsgált mintában. Réz, alumínium anyagokról, ill. egy csontról alkotott képpekkel lett demonstrálva az eljárás kivitelezhetősége.

**[38]ADATLAP**
**a doktori értekezés nyilvánosságra hozatalához**

**I. A doktori értekezés adatai**

A szerző neve: Oláh László
MTMT-azonosító: olahlaszlo
A doktori értekezés címe és alcíme:
Research and Development of Particle Detectors for Muon Tomography and the CERN ALICE Experiment
DOI-azonosító[39]: 10.15476/ELTE.2016.144
A doktori iskola neve: Eötvös Loránd Tudományegyetem Fizika Doktori Iskola
A doktori iskolán belüli doktori program neve: Részecskefizika és csillagászat
A témavezetők neve és tudományos fokozata: Dr. Varga Dezső, Dr. Barnaföldi Gergely Gábor
A témavezetők munkahelye: MTA Wigner Fizikai Kutatóközpont

**II. Nyilatkozatok**

A doktori értekezés szerzőjeként[40]

a) hozzájárulok, hogy a doktori fokozat megszerzését követően a doktori értekezésem és a tézisek nyilvánosságra kerüljenek az ELTE Digitális Intézményi Tudástárban. Felhatalmazom a Természettudományi Kar Tudományszervezési és Egyetemközi Kapcsolatok Osztályának ügyintézőjét, hogy az értekezést és a téziseket feltöltse az ELTE Digitális Intézményi Tudástárba, és ennek során kitöltse a feltöltéshez szükséges nyilatkozatokat.

b) kérem, hogy a mellékelt kérelemben részletezett szabadalmi, illetőleg oltalmi bejelentés közzétételéig a doktori értekezést ne bocsássák nyilvánosságra az Egyetemi Könyvtárban és az ELTE Digitális Intézményi Tudástárban;[41]

c) kérem, hogy a nemzetbiztonsági okból minősített adatot tartalmazó doktori értekezést a minősítés *(dátum)*-ig tartó időtartama alatt ne bocsássák nyilvánosságra az Egyetemi Könyvtárban és az ELTE Digitális Intézményi Tudástárban;[42]

d) kérem, hogy a mű kiadására vonatkozó mellékelt kiadó szerződésre tekintettel a doktori értekezést a könyv megjelenéséig ne bocsássák nyilvánosságra az Egyetemi Könyvtárban, és az ELTE Digitális Intézményi Tudástárban csak a könyv bibliográfiai adatait tegyék közzé. Ha a könyv a fokozatszerzést követőn egy évig nem jelenik meg, hozzájárulok, hogy a doktori értekezésem és a tézisek nyilvánosságra kerüljenek az Egyetemi Könyvtárban és az ELTE Digitális Intézményi Tudástárban.[43]

**2.** A doktori értekezés szerzőjeként kijelentem, hogy

a) az ELTE Digitális Intézményi Tudástárba feltöltendő doktori értekezés és a tézisek saját eredeti , önálló szellemi munkám és legjobb tudomásom szerint nem sértem vele senki szerzői jogait;

b) a doktori értekezés és a tézisek nyomtatott változatai és az elektronikus adathordozón benyújtott tartalmak (szöveg és ábrák) mindenben megegyeznek.

**3.** A doktori értekezés szerzőjeként hozzájárulok a doktori értekezés és a tézisek szövegének plágiumkereső adatbázisba helyezéséhez és plágiumellenőrző vizsgálatok lefuttatásához.

Kelt: Budapest, 2016. 10. 06.

.....
**a doktori értekezés szerzőjének aláírása**

[38] Beiktatta az Egyetemi Doktori Szabályzat módosításáról szóló CXXXIX/2014. (VI. 30.) Szen. sz. határozat. Hatályos: 2014. VII.1. napjától.
[39] A kari hivatal ügyintézője tölti ki.
[40] A megfelelő szöveg aláhúzandó.
[41] A doktori értekezés benyújtásával egyidejűleg be kell adni a tudományági doktori tanácshoz a szabadalmi, illetőleg oltalmi bejelentést tanúsító okiratot és a nyilvánosságra hozatal elhalasztása iránti kérelmet.
[42] A doktori értekezés benyújtásával egyidejűleg be kell nyújtani a minősített adatra vonatkozó közokiratot.
[43] A doktori értekezés benyújtásával egyidejűleg be kell nyújtani a mű kiadásáról szóló kiadói szerződést.